AN INVESTIGATION OF OXIDE COMPOSITE ANODE MATERIALS FOR LITHIUM ION BATTERIES

by

Bo Liu

A dissertation submitted to the faculty of
The University of Utah
in partial fulfillment of the requirements for the degree of

Doctor of Philosophy

Department of Metallurgical Engineering

The University of Utah

August 2013

The University of Utah Graduate School

STATEMENT OF DISSERTATION APPROVAL

The dissertation of **Bo Liu**

has been approved by the following supervisory committee members:

Zhigang Zak Fang	, Chair	**05/02/2013** Date Approved
Ali Abouimrane	, Member	**05/02/2013** Date Approved
Michael L. Free	, Member	**05/02/2013** Date Approved
Ravi Chandran	, Member	**05/02/2013** Date Approved
Yang Ren	, Member	**05/02/2013** Date Approved

and by **Jan Miller** , Chair of the Department of **Metallurgical Engineering**

and by Donna M. White, Interim Dean of The Graduate School.

ABSTRACT

This thesis is aimed to develop high-capacity, inexpensive, long cycle life and environmentally benign anode for lithium-ion batteries. With those goals in mind, a novel oxide alloy composite materials MO-$Sn_xCo_yC_z$ (MO=GeO_2, SnO_2, SiO and SiO_2) have been proposed and investigated. Mechanical alloying method has been used to synthesize oxide alloy composite anode material. The MO-$Sn_xCo_yC_z$ composite has the potential to combine the advantageous properties of both Sn-Co-C (long cycle life) and MO (high capacity) and, thereby, improve the overall electrochemical performance.

The as-milled materials were studied by BET, laser particle analyzer, X-ray diffraction (XRD), scanning electron microscope (SEM), pair distribution function (PDF), extended X-ray absorption fine structure (EXAFS). Evaluating from electrochemical performance, tap density, and cost, GeO_2 and SiO are the most promising candidates alloyed with Sn-Co-C system. The GeO_2 composite anode shows a reversible capacity over 800 mAh/g with good capacity retention. Furthermore, the 1^{st} cycle coulombic efficiency has been improved up to 80%. Compared with GeO_2, SiO has an advantage on the price. A series of composite anode materials of xSiO • (1-x)$Sn_xCo_yC_z$ were studied by electrochemical method. The composition of 50 wt.%SiO-50 wt.%$Sn_{30}Co_{30}C_{40}$ shows the best electrochemical performance. Two different milling methods (ultra high-energy milling and SPEX milling) were employed to prepare the samples. Ultra high-energy milling sample exhibited superior electrochemical performance. Stabilized lithium

metallic powder technique is employed on this anode to improve the first cycle coulombic efficiency. Full-cell configuration ($Li_{1.2}Ni_{0.15}Co_{0.10}Mn_{0.55}O_2$ vs. 50 wt.%SiO-50 wt.% $Sn_{30}Co_{30}C_{40}$) has been cycled over 200 cycles successfully.

The SiO-$Sn_xFe_yC_z$ (x : y: z molar ratio) composite has been milled in different compositions. Metallic iron was employed instead of cobalt, which cuts the cost significantly but does not sacrifice the performance in the meantime. The 50 wt.%SiO-50 wt.%$Sn_{30}Fe_{30}C_{40}$ exhibited specific capacity of 900 mAh/g with acceptable cycle life. The electrodes were loaded with different current rates and showed excellent rate capability.

Based on an overall consideration of various factors, SiO composite anode material prepared by ultra high-energy milling can provide the best electrochemical performance in terms of capacity and cycle life, and also have acceptable tap density and cost.

TABLE OF CONTENTS

LIST OF FIGURES

LIST OF TABLES

LIST OF ABBREVIATIONS AND SYMBOLS USED

AA	a standard size of battery
a, b, c	lattice parameter
AFM	atomic force microscopy
APS	advanced photon source
BET	Brunauer-Emmett-Teller
CNTs	carbon nanotubes
d	diameter
DOD	depth of discharge
EDAX	Energy-dispersive X-ray spectroscopy
EV	electric vehicle
EXAFS	X-ray absorption fine structure
EXANS	X-ray absorption near edge structure
G(r)	probability of finding atomic pairs separated by the real space distance r
I	intensity
I(*f*)	peak intensity
LIBs	lithium-ion batteries
LFP	lithium iron phosphate
LMO	lithium manganese oxide

LTO	lithium titanate
MA	mechanical alloying
MO	metal oxide
MWNTs	multi-walled carbon nanotubes
NCA	lithium nickel cobalt aluminum oxide
NEXAFS	Near-edge X-ray Absorption Fine Structure
NMC	lithium nickel manganese cobalt oxide
NMP	N-Methylpyrrolidone
NOMAD	nanoscale ordered materials diffractometer
OAC	oxide alloy composite
PDF	pair distribution function
PHEV	plug-in electric vehicle
PVDF	Polyvinylidene fluoride
PSA	particle size analyzer
Q	magnitude of the scattering vector
RDF	radial distribution functions
R_w	refined residual value
SEI	solid-electrolyte interphase
SEM	scanning electron microscope
SLMP	solid lithium metallic powder
SNS	spallation neutron source
SPEX	a kind of commercial milling machine
SOC	state of charge

SWCNTs	single-walled carbon nanotubes
S(Q)	normalized scattering intensity
TOF	time-of-flight
UHEM	ultra high energy energy
V	volume
XAS	x-ray absorption spectroscopy
XRD	x-ray diffraction
$\mu(E)$	x-ray absorption coefficient
λ	wavelength
θ	angle
$\rho(r)$	microscopic pair density
ρ_0	average number density
$\chi(k)$	relative modulation
δ	isomer shift
H_{eff}	magnetic hyperfine field
ε	quadrupole splitting
^{o}	degree

ACKNOWLEDGEMENTS

I would like to express my deep gratitude to my professor Zhigang Z. Fang for his considerable support of my life and study. I am glad to have had the chance to do research in the Argonne National Laboratory. My supervisor Ali Abouimrane and I have gone through a lot of things during those few fleeting moments of time. I really appreciate his guidance and support.

I would like to express my thanks to colleagues of Chemical Science Engineering division for their help, patience, and suggestions. Zonghai Chen deserves special thanks.

I express my gratitude to the scientists, Yang Ren and Mahalingam Balasubramanian of Advanced Photon Source.

I also want to express my love to my parents. It is a long journey and I am grateful for their company.

Finally, I want to thank to all the colleagues and friends in Prof. Fang's group. Among them, Pei Sun deserves special thanks.

CHAPTER 1

INTRODUCTION

1.1 Background and Motivation

Science and technology have made rapid progress during the last 100 years. Meanwhile, the population growth on the globe is quite fast as well. The growth rate of the world population has expanded sharply from the last century. Obviously, our population cannot continue to expand without our incurring serious consequences-both for ourselves and for the planet as a whole. The emerging cityscape is often dazzling, but also energy intensive and polluting. The most recent example is Beijing's air pollution. Fig.1-1 reveals how serious the air pollution issue is in Beijing.[1]

According to some news reports, emissions from motor vehicles, coal-burning, and cooking contributed to the dense smog in Beijing.[2] Motor vehicles are blamed for nearly a quarter of the capital's PM2.5, or airborne particles measuring less than 2.5 micrometers in diameter. The continually occurring air pollution brings about a disaster to human health. Hence, this gives a great motivation to develop cleaner energy vehicles instead of gasoline engine vehicles.

1.2 Batteries

Batteries are an important energy storage device, which have been widely applied in portable power devices, laptops, cell phones, etc. A battery is a device consisting of one

Fig.1-1 Smog (left) and clear (right) weather in Beijing[1]

or more electrochemical cells that convert stored chemical energy into electrical energy.[3] There are various types of batteries, in general, which can be divided into two groups: primary batteries and secondary batteries. Primary batteries cannot be electrically charged, but these batteries have high energy density and good storage characteristics. Lithium primary batteries, which have been commercialized about 20 years ago, exist in many forms: for example, lithium-manganese dioxide, lithium-carbon monofluoride, and lithium-thionyl chloride batteries. They are used with the other batteries such as carbon-zinc, alkaline-manganese, zinc-air, and silver oxide-zinc batteries.[4] Secondary batteries can be electrically charged, and these batteries can offer savings in costs and resources. Lithium-ion and nickel-metal hydride batteries have been developed, and are used with the other secondary batteries, such as nickel-cadmium, lead-acid, and coin-type lithium secondary batteries.[4]

The lithium-ion battery is considered as the most promising candidate for portable tools, laptops, cell phones, and electric vehicles because of its many advantages, such as

light weight and high energy, no memory effect, and low self-discharge rate.[5] In recent years, some new types of secondary batteries like lithium-air batteries promise three to five time as much energy as lithium-ion, which allow cars to drive over 500 miles per full charge.[6] However, there still exist many challenges facing the design of Li-air batteries, which currently limit their use to the laboratory. One of the largest challenges lies in keeping the battery protected from the environment. Atmospheric oxygen must be present at the cathode, but the cathode can be degraded by humidity.[7] Safety and cycle life also need to be solved. Fig. 1-2 gives a summary of energy density of different secondary batteries.[8]

1.3 Lithium-ion Batteries

Lithium batteries were first proposed by M. S Whittingham in the 1970s.[9] Whittingham used titanium sulfide and lithium metal as the positive and negative electrodes, respectively. TiS_2, NbS_2, and $NbSe_2$ as the first-generation cathode materials

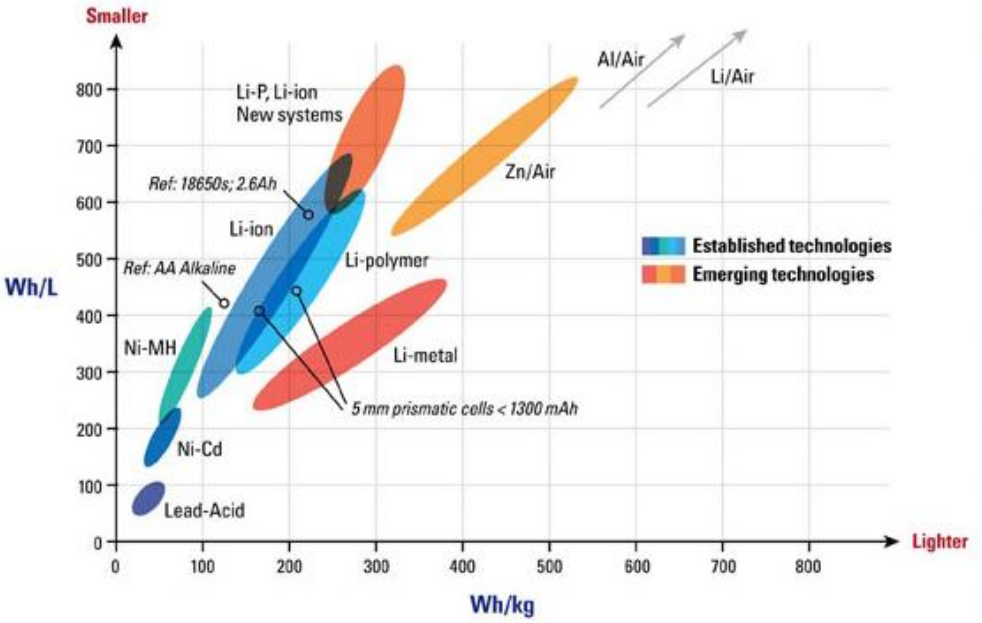

Fig.1-2 Energy density of various batteries[8]

were coupled with metallic lithium anodes for the lithium-ion battery.[4] The negative electrode that was employed was metallic lithium. However, the most fatal drawback is dendrite formation on the surface of metallic lithium, which may break the separator and lead to a battery short, even ignition. Also due to various defects like low voltage and degradation, this kind of nonlithiated cathode materials cannot meet the requirement for commercialization. In 1979, J. Goodenough and K. Mizushima reported a rechargeable cell with high cell voltage in the 4V range using lithium cobalt oxide ($LiCoO_2$) as the positive.[10] Hence, $LiCoO_2$ can be the source of lithium ions, which means that other negative electrode materials have the potential instead of lithium metal. By enabling the use of stable and easy-to-handle negative electrode materials, $LiCoO_2$ opened a whole new range of possibilities for novel rechargeable battery systems.[11] Until 1991, commercial Li-ion batteries were successfully introduced into the market by Sony, which used $LiCoO_2$ as a cathode material.[12] Ever since then, Li-ion batteries based on $LiCoO_2$ and carbon have been of the most popular products in the market because of their capability to be safely operated for thousands of cycles. Because of the considerations of price and environment, much research has been done to find a replacement instead of cobalt. Materials with the layer structure more extensively examined for positive electrodes include $LiCoO_2$, $LiNiO_2$, $LiCo_{1-x}Ni_xO_2$, and $LiMnO_2$.[13-18] M. Thackeray, Goodenough, and co-workers demonstrated the feasibility of manganese spinel as a cathode material.[19] It has some advantages like nontoxicity, low cost, and high voltage.[20,21] Unfortunately, it suffers from fast capacity fading, especially at elevated temperatures. Therefore, researchers are always studying metal ion dopants, which help to stabilize the structure. In 1996, Goodenough and co-workers identified lithium

phosphate ($LiFePO_4$) and other olivine structured cathode materials.[22] Olivine structured $LiFePO_4$ has attracted considerable research interest for Li-ion batteries as cathode materials due to its high theoretical capacity of 170 mAh/g, flat voltage at 3.45 V, good cycling stability, low cost, and environmentally benign nature. Various types of Li-ion batteries are used on different devices, according to chemistry, performance, cost, and safety characteristics. The lithium-ion batteries of most portable tools, electronics, cell phones and laptops use lithium cobalt oxide ($LiCoO_2$) as a cathode, which offers high energy density, but has well-known safety concerns, especially when damaged. Lithium iron phosphate (LFP), lithium manganese oxide (LMO), and lithium nickel manganese cobalt oxide (NMC) offer lower energy density, but longer lives and inherent safety. These chemistries are being widely used for electric tools, medical equipment, and other roles. NMC in particular is a leading contender for automotive applications. Lithium nickel cobalt aluminum oxide (NCA) and lithium titanate (LTO) are specialty designs aimed at particular roles.[11]

In the recent year, more and more hybrid vehicles and electric vehicles have come into our daily life. Nissan and Chevrolet, almost at the same time, announced their new models of the electric and plug-in hybrid vehicles, the Leaf and Volt, respectively. They all employ lithium-ion battery technology instead of a conventional internal combustion engine. The Chevy Volt plug-in hybrid vehicle can get 40 miles of all-electric range. It features a 16 kWh lithium-ion battery pack that weighs less than 400 pounds and its recharging takes about eight hours using a 120 V outlet.[23]

The performance of a cell or a battery is characterized by its voltage (volts, V), capacity (ampere-hours, Ah), specific capacity (ampere-hours/kilogram, Ah/kg), specific

energy (watt-hours/kilogram, Wh/kg), specific power (watts/kg, W/kg), cycle life, and rates. The voltage between two points is a short name for the electrical driving force that could determine an electric current between those points. Capacity, quoted in amp-hours, of a battery is equal to the amount of charge that can be delivered. The theoretical capacity in a lithium-ion battery can be calculated as shown in the following equation.

$$\text{Gravimetric Capacity} = \frac{N \times F}{M}\left(\frac{Coulomb}{g}\right)$$

$$= \frac{N \times F}{3.6M}\left(\frac{mAh}{g}\right) \quad (1.1)$$

$$\text{Volumetric Capacity} = \text{Gravimetric Capacity} \times \text{density}$$

N= moles of transportable Li-atoms (=electrons) per each mole of material

F= Faraday's constant (=96487 Coulomb or 26.8 Ah)

M= Formula weight of the material

Energy density is the amount of energy stored in a given system or region of space per unit mass. Power density indicates how much power a battery can deliver on demand. Cycle life is the number of cycles at which the discharge capacity has deteriorated to 80% of the first discharge capacity. In describing batteries, current is often expressed as a C-rate in order to normalize against battery capacity, which is often very different between batteries. A C-rate is a measure of the rate at which a battery is discharged relative to its maximum capacity. A 1C rate means that the discharge current will discharge the entire battery in 1 hour. For a battery with a capacity of 100 Amp-hrs, this equates to a discharge current of 100 Amps. A 5C rate for this battery would be 500 Amps, and a C/2 rate would be 50 Amps. The battery condition is always described by some variables.

State of Charge (SOC)(%) is generally calculated using current integration to determine the change in battery capacity over time. Depth of Discharge (DOD)(%) is expressed as a percentage of maximum capacity. A discharge to at least 80% DOD is referred to as a deep discharge. Terminal voltage is the voltage between the battery terminals with load applied. Open-circuit voltage is the voltage between the battery terminals with no load applied. It depends on the battery state of charge, increasing with state of charge. Cut-off voltage is the minimum allowable voltage. Nominal voltage is the reported or reference voltage of the battery. Internal resistance, known as impedance, is the reason of voltage drop with current load.

An electrochemical cell is a combination of an anode, electrolyte, separator, and cathode. The anode of the cell loses electrons and thus is oxidized during the electrochemical reaction. The cathode accepts these electrons and undergoes reduction. The electrolyte is the bridge aiding in the travel of charge between the two electrodes. The anode and the cathode of a cell are separated by a porous membrane that allows the ions to pass on either side but prevents electrons from passing, thus preventing short circuiting within the cell. A Li-ion cell consists of a cathode that is a source of Li ions and an anode sink. A cathode is generally a Li-rich transition-metal compound with high Li chemical potential to increase cell voltage. It not only should allow Li insertion/extraction reversibly but should undergo very little or no structural change during the entire process. The compound needs to be an excellent conductor of ions and electrons and be chemically stable over the entire potential range involving the Li-ion shuttling process. The anode is the host for the Li ions and should have the lattice structure to accommodate these ions in addition to possessing all the properties of the

cathode. A Li-ion cell is comprised of two current collectors that act as substrates to hold the electrode materials. These support the anode and cathode and provide a uniform current distribution along with low contact resistance to minimize the polarization of an electrode during the operation of the cell. The most common current collectors used are made of copper and aluminum. The reaction mechanism of a lithium-ion battery is exhibited in Fig. 1-3.[24]

1.4 Anode Materials

The earliest choice for an anode material in a lithium battery is lithium metal. It is an ideal anode material due to its light weight (the lightest metal), high electronegativity (-3.04 V vs. the standard hydrogen electrode), and high theoretical capacity (3860 mAh/g).[25] Based on these outstanding properties, lithium metal batteries were proposed

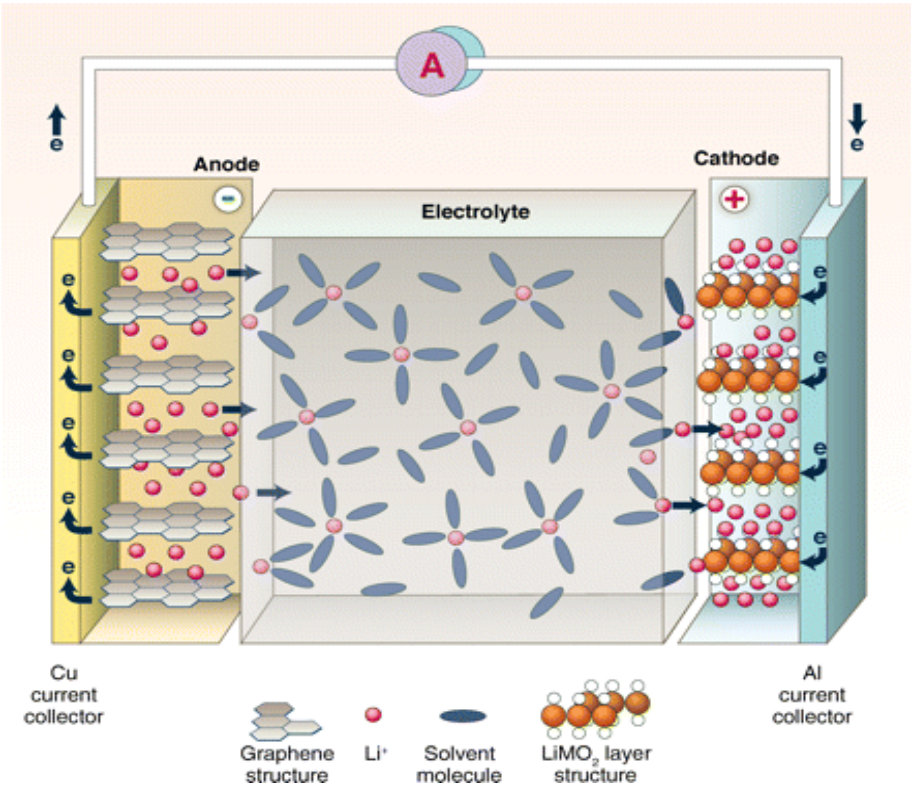

Fig. 1-3 The reaction mechanism of a Li-ion battery[24]

40 years ago as an ideal system for high energy-density applications. In fact, one of the first commercial rechargeable lithium systems was the Li metal anode versus MoS_2 cathode cell.[26] But Li metal as an anode material was flawed. When Li electroplates during a charge it tends to form dendrites that can grow to the extent that the separator is pierced, which can subsequently lead to a short. The dendrite formation can also result in poor cycle life. The heat associated with an internal short coupled with the increased heat produced by a larger and more reactive surface can result in a runaway exothermic reaction. Ultimately, this can lead to the ignition of the cell's components. Therefore, lithium itself is not considered to be an appropriate anode for several reasons, including its short lifecycle, the formation of dendrites upon cycling, and its high reactivity and low melting point, which may lead to combustion and explosion

Therefore, lithium alloys involved much attention. The advantage of lithium alloys is that the packing density is very close to, and sometimes higher than, that of lithium in lithium metal. But huge volume expansion when Li is inserted in alloys limits their application use. At present, mostly carbons are used as the negative electrode of commercial rechargeable lithium batteries. Table 1-1 compares the theoretical capacities of various alloy anode materials, carbon, and lithium metal.

1.4.1 Carbon

A variety of carbonaceous materials have been investigated as negative electrodes, such as graphite petroleum coke, carbon fibers, carbon wires, and mesocarbons,[33-35] but only graphite has dominated the commercial battery market because of its low cost, good reversibility, and safe disposal. Graphite exhibits all the desirable characteristics of anode materials, high capacity (372 mAh/g), low voltage in reference to lithium metal (0.2 V),

Table 1-1 Comparison of the theoretical capacities of various alloy anode materials, carbon, and lithium metal[26-32]

Compound	Gravimetric Capacity (mAh/g)	Volumetric Capacity (Ah/L)
$Li_{4.4}Si$	4199	9784
$Li_{4.4}Sn$	994	7266
$Li_{4.4}Pb$	569	6458
Li_3As	1073	6148
Li_3Sb	660	4416
LiAl	993	2680
LiC_6	372	818
Li	3861	2062

and good reversibility (graphite retains 80% of its first discharge capacity for 1200 cycles). Tremendous studies have been made to investigate the storage mechanism of graphite. It is made up of stacking sheets of hexagons with a carbon atom at each corner of the hexagon in a sequence held together by Van Der Waals forces. The forces between any two neighboring sheets are much weaker than the forces between any two given carbons in the same sheet. The layer distance is 3.35 Å, which provides the ideal site for lithium intercalation. When lithium intercalates in graphite, it occupies an interstitial site between two neighboring planes of graphite. Lithium ions can only combine on every 2nd carbon hexagon in the graphite sheet which limits the amount of lithium ions to 1 for every 6 carbon atoms, which is corresponding to the insertion reaction as below.[36] This

is directly corresponding to the theoretical energy storage capacity of 372 mAh/g.[37] Fig. 1-4 shows the typical intercalation process of lithium into graphite.[37]

As another class of carbon materials, carbon nanotubes (CNTs) have been presented as a competitive anode material.[38-43] Since the discovery of CNTs in 1991,[44] they have been demonstrated to be a good anode material because of their unique structure and good conductivity. Single-walled CNTs (SWCNTs) can have reversible capacities from 300 to 600 mAh/g, which is significantly higher than that of graphite.[45-50] Multiwalled CNTs (MWNTs) prepared through different synthesis methods exhibited reversible capacity up to 400 mAh/g.[51-53] The reversible capacity can be further improved up to 700 to 1000 mAh/g through opening the tubes by chemical etching and mechanical alloying.[54-57]

Unfortunately, carbon nanotubes have a relatively high irreversible lithium ion capacity.[58] Therefore, at the first charge, more lithium ions are inserted into the carbon nanotubes than ever come out. Another problem for CNT is the lack of a voltage plateau

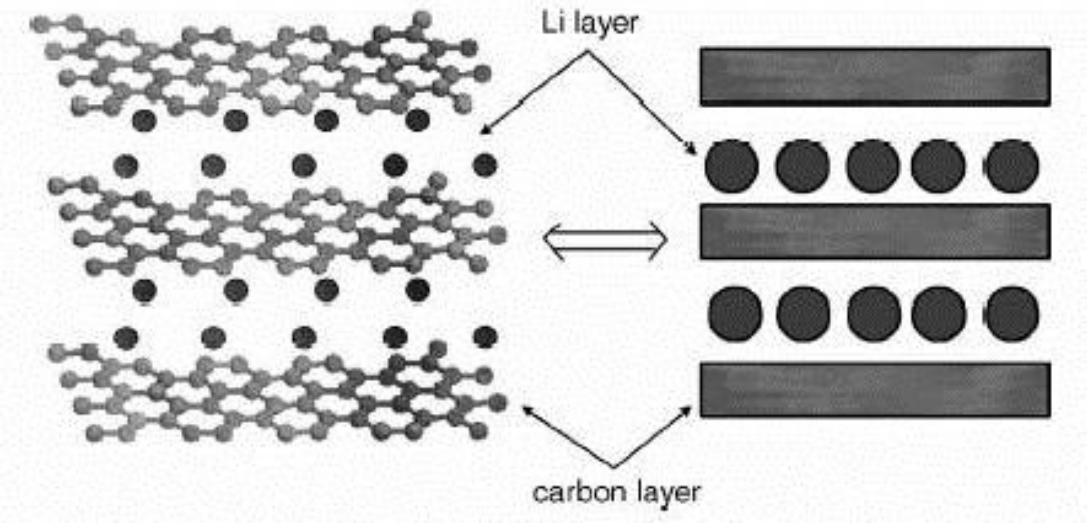

Fig. 1-4 Schematical illustration of lithium intercalation into the graphite structure[37]

while the battery is discharging. CNT anode has broad changes in voltage as the cell discharges, which is related with morphology. This can make them difficult to use in most electronics which require a stable voltage source. High irreversibility and large hysteresis greatly limit the use of Li-ion batteries.

1.4.2 Alloys

Due to the limitation of the theoretical capacity (372 mAh/g) of graphite, elemental metals are appealing candidates to replace graphite as anode materials for Li-ion batteries. In particular, among the various Li alloy elements, Group IV elements such as Si, Ge, and Sn attracted the most attention owing to their high capacity of Li-rich alloys. The reaction usually proceeds reversibly according to the general scheme shown in equation 1.2.[59-62]

$$Li_xM \leftrightarrow x\ Li^+ + x\ e^- + M \qquad (1.2)$$

The major challenge in the development of metallic anodes is the high volume change in the reaction, which leads to the degradation of the anode and the loss of electrical conductivity. Table 1-2 compares the volume changes of various alloy anode materials. Si, Ge, and Sn are the most attractive and widely investigated candidates, due to their

Table 1-2 Comparison of the volume expansions of various alloy anode materials[59-62]

Metal	Si	Ge	Sn	Graphite
Li alloys	$Li_{22}Si_5$	$Li_{22}Ge_5$	$Li_{22}Sn_5$	LiC_6
Volume expansion	323	370	300	9

high gravimetric and volumetric capacities. The electrochemical properties and lithiation mechanism of Si electrodes has been studied intensively.[63-73]

Many articles have reported that crystalline silicon becomes an amorphous Li-Si alloy when Si reacts with Li electrochemically.[66-69] At room temperature, the electrochemical lithiation mechanism was proposed as the following equations.[70-72]

During discharge:

$$\text{Si (crystalline)} + x\text{Li}^+ + x\text{e}^- \rightarrow \text{Li}_x\text{Si (amorphous)} + (3.75\text{-}x)\text{Li}^+ + (3.75\text{-}x)\text{e}^- \quad (1.3)$$

$$\rightarrow \text{Li}_{15}\text{Si}_4 \text{ (crystalline)} \quad (1.4)$$

During charge:

$$\text{Li}_{15}\text{Si}_4 \text{ (crystalline)} \rightarrow \text{Si (amorphous)} + y\text{Li}^+ + y\text{e}^- + \text{Li}_{15}\text{Si}_4 \text{ (residual)} \quad (1.5)$$

From ex-situ and in-situ X-ray diffraction results, crystalline Si becomes an amorphous Li-Si alloy, shown in the equation 1.3, and the amorphous phase crystallizes as a $Li_{15}Si_4$ phase around 50 mV *vs.* Li/Li^+, as in equation 1.4. High capacity is achieved on the first lithiation, but capacity quickly fades with cycle number. The large irreversible capacity loss of this Si anode comes from the first cycle. According to the equilibrium phase diagram, Li-Si binary intermetallic compounds involve $Li_{12}Si_7$, Li_7Si_3, $Li_{13}Si_4$, and $Li_{22}Si_5$. The metastable $Li_{15}Si_4$ phase can be characterized at the potentials lower than 50 mV versus lithium. During the delithiation process, the final product is amorphous Si (equation 1.5). The voltage profile of delithiation losses plateau becomes a sloping shape. To understand the failure mechanism of Si electrode, Yi Cui *et al*. outlined three fundamental materials challenges of Si electrode, as illustrated in Fig. 1-5.[74]

Firstly, the huge volume changes during the Li ion insertion/extraction cause cracking

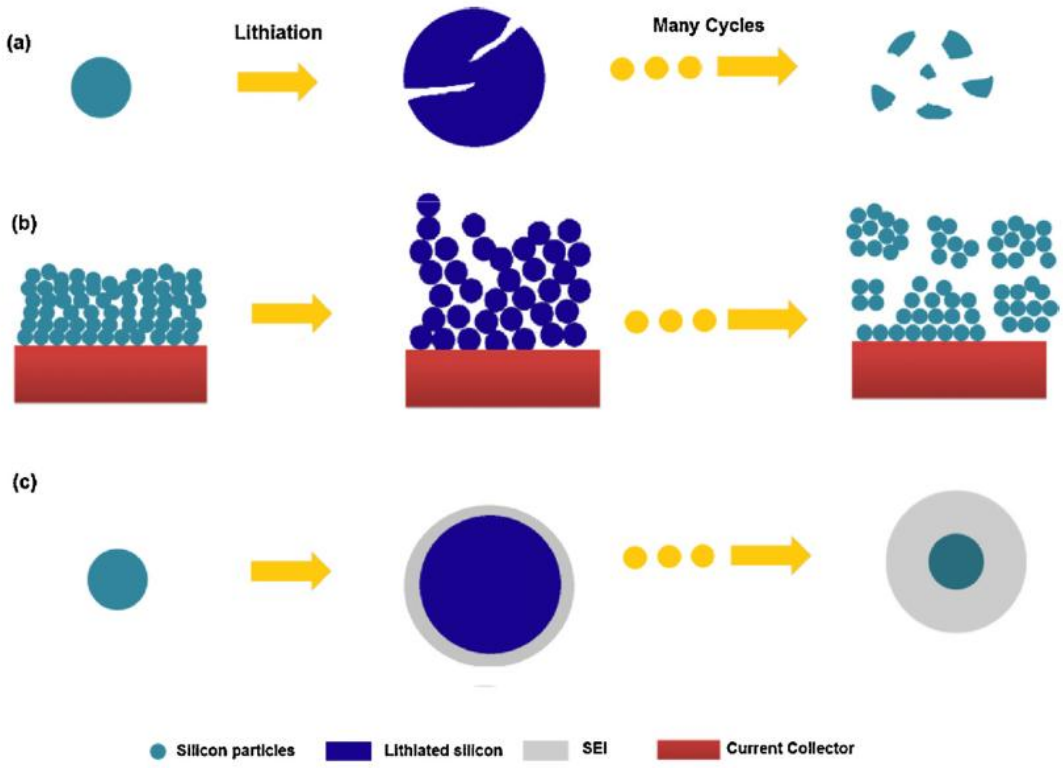

Fig. 1-5 Si electrode failure mechanisms: (a) material pulverization (b) morphology and volume change of the entire Si electrode (c) continuous SEI growth

and pulverization of the Si, which leads to loss of electrical contact and eventual capacity fading. Secondly, during lithiation, Si particles expand and impinge on each other. And during delithiation, Si particles contract, which can result in increased internal resistance that is caused by a loss of the contact area between Si and the carbon particles, which are a conducting agent. This is caused by volume contraction of the Si particles after expansion in the previous Li–Si alloying process. This morphology change can further contribute to capacity fading. Thirdly, the decomposition of organic electrolyte below ~1V versus Li/Li^+ forms a layer on the electrode material surface called the "solid-electrolyte interphase" (SEI). The SEI layer is used to protect the electrode and prevent further side chemical reactions. So the dense and stable SEI layer is a critical factor for

obtaining long cycle life. However, the large volume change makes it very challenging to form the stable SEI shown in Fig. 1-5c. The expansion and shrinking of Si electrodes can break the SEI layer and fresh material is exposed to electrolyte, resulting in a thicker and thicker SEI layer during the charge/discharge process. The electrochemical reactions of Sn and Ge electrodes are very similar with that of Si. The theoretical capacity of Sn is 960 mAh/g, corresponding to 4.25 atoms of lithium that can be accommodated into each Sn atom. Although Sn has a lower gravimetric capacity than Si, Sn is an attractive anode material due to its volumetric capacity of about 2000 mAh/cm^3. It is also limited by its poor capacity retention cause by large volume changes. The diffusivity of Li in Ge is 400 times higher than that in Si at room temperature, indicating that Ge may be an attractive electrode material for high-power-rate anodes.[75-76] Theoretically, Ge can uptake 4.4 Li, corresponding to 1623 mAh/g specific capacity. Meanwhile, the huge volume change is up to 370% accompanying de/alloying with lithium which is the fatal factor for cycle life.

1.4.3 Oxides

In 1997, Fuji announced its Stalion battery, which employed an amorphous tin composite oxide (TCO) anode.[76-79] The material, an amorphous tin oxide composite, was claimed to have theoretical volumetric and gravimetric capacity advantages over carbon of four and two times, respectively. The electrochemical studies of tin oxides have been reported, including SnO and SnO_2.[80-83] The electrochemical reaction of lithium with tin dioxide involves two main steps, in the following equations. First, SnO_2 reacts with Li_2O and metallic Sn, electrochemically, called a conversion reaction (equation 1.6):

$$4Li + SnO_2 \rightarrow 2Li_2O + Sn \qquad (1.6)$$

Second, Li^+ ion intercalates into metallic Sn and for Li_xSn intermetallic phases (equation 1.7):

$$xLi + Sn \rightarrow Li_xSn\ (0< x <4.4) \quad (1.7)$$

Assuming a reversible alloying process of 4.4 Li Li per Sn, the maximum theoretical capacity for SnO_2 would be 781 mAh/g. The Li_2O acts as a buffer matrix but remains electrochemically inactive. Most oxide anode materials obey above two step reactions, such as SnO, GeO_2, MoO_3, and CoO.[84-87] Beside the volume expansion like pure Sn, Ge, Mo, etc., a main drawback of the tin oxides is the large irreversible consumption of lithium in the first cycle. The formation of Li_2O and SEI film is the main reason of this irreversibility. For full cell configuration, positive electrodes are the Li source. So if anodes consume a large amount of Li, the capacity of full cells would be very low, limiting the commercial use. The practical implementation of oxides is hampered by poor material cycleability due to large volume change and coulombic efficiency. The SiO is another choice for the anode material in Li-ion batteries. It contains a relatively small amount of active Si compared to pure Si. Many researchers illustrated that SiO is thought to consist of nanoparticles of metallic silicon distributed in a matrix of SiO_2, which has a SiO_2 glass-like structure.[88] SiO_2 plays a matrix role for the buffer component of volume changes. Therefore, the cycle performance of SiO is much better than that of pure SiO.

1.4.4 Tin-Cobalt-Carbon

In 2005, SONY announced their NEXELION battery, which uses a Sn-Co-C composite as the anode material.[89] For anode materials, tin (Sn) is one of the most attractive materials for Li-ion batteries because it has a large capacity (as high as over

900 mAh/g) when forming $Li_{4.4}Sn$ alloys.[90] However, problems may arise from the poor cycling behavior associated with Sn aggregation and volume expansion and contraction upon the electrochemical alloying and dealloying with Li. In order to solve these problems, Sn-transition metal (Ti, V, Cr , Mn, Fe, Ni, Co) alloys have been studied. Dahn and co-workers studied the roles of Co and C in Sn-Co-C composites using Sn MÖssbauer spectroscopy and in situ AFM. They suggested that Co did not form the Co-carbide phase and led to the wide range of amorphous Sn-Co-C composites, which consisted of Sn-Co alloy grains surrounded by a carbon matrix.[91-98] In this alloy, the main electrochemical active material is Sn while the two other elements act as supporting components in order to buffer the large volume variations which occur in the course of the Li-Sn alloying-dealloying electrochemical process. The reciprocal and combined role of Co and C, however, may be more complex than that of a mere buffering action. Some researchers suggested that carbon has multifold actions which include promotion of amorphicity, increase of specific capacity, and stabilization of Li-Sn alloy on the atomic scale. These positive effects of carbon are supported by the third Co component which prevents the formation of intermetallic carbides over the entire useful composition range, thus finally avoiding the precipitation of Sn out of the composite. With more understanding of electrochemical properties of Sn-Co-C material, Dahn and co-workers employed combinatorial methods to synthesize a library of $(Sn_{0.55}Co_{0.45})_{1-y}C_y$ for $0 < y < 0.5$ by sputtering.[91-96] The best electrochemical performance was attained by the composition near $Sn_{30}Co_{30}C_{40}$. Subsequently, they compared the performance between mechanically alloyed and sputtered Sn-Co-C composites. Although both are characteristic of amorphous-like or nanostructured materials, the sputtered material

showed a reversible specific capacity over 600 mAh/g close to the theoretical capacity, while the ball-milled material had a specific capacity of 450 mAh/g. Even though sputtering is a better technique to synthesize nano-level particles and more uniform material as opposed to mechanical alloying, it is not suitable for producing Sn-Co-C alloys for industrial scale because of the high cost of the electrical power required.

1.5 Challenge

Li-ion battery technology has become very important in recent years as these batteries show great promise as power sources that can lead us to the electric vehicle (EV) revolution. The development of new materials for Li-ion batteries is the focus of research in prominent groups in the field of materials science throughout the world. Li-ion batteries can be considered to be the most impressive success story of modern electrochemistry in the last two decades. They power most of today's portable devices, and are gradually used on PHEV and EV.

As we know, the limited capacity (372 mAh/g) of the currently used graphite anode and the possibility of lithium plating and safety hazards arising from an operating voltage close to that of Li/Li^+ have prompted interest in alternative anodes. $Li_4Ti_5O_{12}$ with the spinel structure has emerged as an attractive alternative as its higher operating voltage of 1.5 V versus Li/Li^+ prevents SEI layer formation with the electrolyte and offers excellent safety.[99,100] However, its limited capacity of 175 mAh/g along with the higher operating voltage sacrifices the cell voltage and energy significantly. Despite the many merits of carbon anode materials and Lithium Titanium Oxide, low capacity or poor cycleability are problems too severe to meet the requirements of the next-generation anode for lithium ion batteries.

In this regard, several lithium alloy anode materials Li_xM_y have attracted much attention due to their high capacity values, $Li_{3.75}Si$ (3578 mAh/g),[101] $Li_{3.75}Ge$ (1385 mAh/g),[102] $Li_{4.4}Sn$ (993 mAh/g),[79] and Li_3Sb (660 mAh/g).[103] The major issue with the alloy anodes is the severe capacity fade, arising from a huge volume change occurring during the charge-discharge (lithium alloying/dealloying) process. The volume change leads to lattice stress and consequential cracking and crumbling of the alloy particles during cycling, resulting in abrupt loss in capacity within a few charge-discharge cycles. Volume expansion is an inevitable drawback for metal and oxide anode materials. Hence, composite materials have been pursued, involving volume expansion material, like Si, Sn, Ge, SnO_2, etc. and a buffer component acting as a matrix to absorb the volume change during the charge-discharge cycling. Silicon/graphite, silicon/graphene, silicon/SWCNT, and silicon /MWCNT composite materials have been studied by many groups.[104-117] Although these above-mentioned methods can prolong the cell life with the alloy anode, meanwhile, energy density of cells also has inflicted considerable loss due to low loading mass or tap density. Dahn proposed an active/inactive composite anode for lithium ion batteries, with “active” grains which can alloy with lithium and “inactive” grains which cannot. The inactive grains act as a matrix to hold the active grains as they repeatedly alloy with lithium during the operation of a lithium battery. For example, Sn-M-C systems with M = Ti, V, Cr, Mn, Fe, and Co have been pursued with this strategy,[91] and Sony Corporation has introduced a new lithium ion battery called Nexelion with an amorphous Sn-Co-C composite as the anode.[89] However, this strategy was not successful with any other Sn-M-C systems, and the high cost of Co prohibits the adoption of Sn-Co-C in large cells for vehicle and stationary storage applications. Clearly, design

of safe, low-cost alternatives is critical for these emerging applications.

1.6 Motivation and Objectives

Although oxides anode materials have high capacity, the large volume change is still an unsolved problem, which is detrimental to cycle life. That prevents the application greatly. In contrary, Sn-Co-C has an excellent cycle life as the anode material for lithium-ion batteries. It has been demonstrated on NEXELION AA lithium-ion batteries. However, it cannot be used as electric vehicles' batteries, due to the expensive transition metal cobalt. Moreover, the specific capacity is comparable with carbon, which is not an ideal candidate as the next-generation anode material. The objective is developing new anode material for Li-ion batteries with high capacity and long cycle life.

Our goal of this thesis is developing a new oxide composite anode material for lithium ion batteries, which has the potential to combine the advantageous properties of both Sn-Co-C (long cycle life) and MO (high capacity) and, thereby, improve the overall electrochemical performance. The next step will be reducing the cost further. For example, iron is an ideal candidate because it is low cost and environmentally benign.

The objectives of our research are listed below:

1. Develop new advanced high energy anode materials with long life and improved safety for PHEV and EV applications
2. Develop a low cost synthesis method to prepare high energy anodes
3. Structural understanding and electrochemical characterizations of the prepared anode materials

1.7 Organization of This Thesis

This thesis has the aim of developing oxide composite anode material for lithium ion batteries and making the electrochemical study and structural understanding. Chapter 1 provides a broad review of various batteries, mainly focusing on lithium ion batteries and the main kinds of anode materials. Chapter 2 introduces the background and objectives of this work.

Chapter 3 describes the experimental techniques used in this work and the material preparation method. This includes the characterization of materials by electrochemical methods, such as XRD, PDF, EXAFS, and Mössbauer spectroscopy. Composite materials were prepared by different kinds of milling methods, SPEX and Planetary millings.

Chapter 4 shows composite materials SnO_2-$Sn_{30}Co_{30}C_{40}$ and SiO_2-$Sn_{30}Co_{30}C_{40}$ as negative electrodes prepared by high-energy ball milling (SPEX). The SnO_2 composite anode showed 400 mAh/g for at least 100 cycles, but with poor rate performance. SiO_2 is known as an inactive material as a negative material. However, SiO_2 composite exhibits interesting electrochemical behaviors. Anomalous capacity releases when alloyed mechanically with commercial tin, cobalt, and graphite powders. We tried to screen out an appropriate oxide to couple with tin-cobalt-carbon for the best electrochemical performance.

Chapter 5 explores GeO_2-$Sn_{30}Co_{30}C_{40}$ as the negative electrode synthesized by high-energy ball milling (SPEX). The composite anode shows a reversible capacity over 800 mAh/g with good capacity retention. Furthermore, the first cycle coulombic efficiency has been improved up to 80%, which is much higher than that (34.6%) of pure GeO_2. The pair distribution function (PDF) demonstrated the reversible reaction of GeO_2 and SnO_2,

which is the key point of improved coulombic efficiency in the first cycle. The feature may explain the catalytic role of high temperature phase Co_3Ge_2, which can decompose Li_2O and act as an electronic conductive component for Ge and Sn oxidations.

Chapter 6 explores composite materials as the anode for lithium-ion batteries, xSiO·(1-x)$Sn_{30}Co_{30}C_{40}$, where $0 \leq x \leq 1$, synthesized by SPEX ball milling methods. The milled materials were studied by X-ray diffraction (XRD), pair distribution function (PDF), and electrochemical testing. The XRD and PDF data show that CoSn is the main phase and is detected in all seven samples. As the amount of SiO increases, $CoSn_2$ is formed. Also with increasing SiO, the reversible specific capacity of the composite anode materials increases, but the cycle performance declines. The composition of 50 wt. % SiO-50 wt. % $Sn_{30}Co_{30}C_{40}$ gives the best electrochemical performance, a reversible capacity of 633 mAh/g after 50 cycles. X-ray and neutron PDF techniques were used to probe the local structure of as-milled 50 wt. % SiO-50 wt. % $Sn_{30}Co_{30}C_{40}$. Ex-situ XRD and PDF study for samples taken at different cutoff voltages reveal a phase transformation during charge/discharge via an intercalation/conversion reaction. We took 50 wt. % SiO−50 wt. % $Sn_{30}Co_{30}C_{40}$ as an example, and found that ultra high-energy ball milling (planetary milling) offers more nanoparticles and higher capacity compared with conventional milling. High-energy X-ray diffraction indicates the presence of $CoSn_2$ and Co Bragg phases and highly distorted phases in the mixture. Extended X-ray absorption fine structure analysis reveals a tremendous difference between UHEM and SPEX samples. The pair distribution function shows the local structure and indicates that SiO and SnCoC are not only a physical mixture, but have reacted chemically. Full-cell testing established the feasibility of the composite as an anode material for high-energy, long-life Li-ion

batteries. These results demonstrate that the nanostructured SiO−$Sn_{30}Co_{30}C_{40}$ composite is a promising anode material for practical applications.

Chapter 7 begins by considering the replacement of cobalt with a cheaper and environmentally benign transition metal, Fe. A family of composite materials as anodes for lithium-ion batteries, SiO–$Sn_xFe_yC_z$ (x : y : z molar ratio), was synthesized by mechanical alloying. The aim of this work is to find the optimal point by tuning the composition of Sn–Fe–C in the hope of obtaining better electrochemical performance. Different combinations were studied by high-energy X-ray diffraction and electrochemical methods. The results indicated that carbon can improve the cycle life, the amount of iron affects phase formation greatly, and the $FeSn_2$ phase should be avoided because of its detrimental effect on cycle life. The 50 wt% SiO–50 wt% $Sn_{30}Fe_{30}C_{40}$ composition was studied using the pair distribution function and Mössbauer spectroscopy. This material exhibits high specific capacity (900 mAh/g at C/6 rate) with good cycle life and rate capability. Chapter 8 summarizes the above works and analyzes future work.

1.8 Reference

[1] http://www.theatlanticcities.com/politics/2013/02/exactly-how-bad-beijings-smog-crisis-one-photo/4838/

[2] http://www.wantchinatimes.com/news-subclass-cnt.aspx?id=20130204000066&cid=1105

[3] http://en.wikipedia.org/wiki/Battery_(electricity)

[4] Jürgen O. Besenhard, *Handbook of Battery Materials*

[5] M. Winter and J. Brodd, *Chemical Review*, 2004, **104**(104) 4245.

[6] http://theenergycollective.com/cliftonyin/83255/lithium-air-battery-rd-moves-forward

[7] http://en.wikipedia.org/wiki/Lithium%E2%80%93air_battery

[8] http://homework.uoregon.edu/pub/class/hc441/bstorage.html

[9] M. S. Whittingham, *Science*, 1976, **192** (4244) 1126.

[10] K. Mizushima, P. C. Jones, P. J. Wiseman and J. B. Goodenough, *Mater.Res.Bull*. 1980, **15**, 783.

[11] http://en.wikipedia.org/wiki/Lithium-ion_battery

[12] T. Nagaura and K. Tozawa, *Prog.Batt. Solar Cell*, 1990, **9**, 209.

[13] T. Ohzuku, A. Ueda and M. Nagayama, *J. Electrochem. Soc.*, 1993, **140**, 1862.

[14] W. Li, J. N. Reimers and J. R. Dahn, *Solid State Ionics*, 1993, **67**, 123.

[15] T. Ohzuku, A. Ueda and M. Kouguchi, *J. Electrochem. Soc.*, 1995, **142**, 4033.

[16] Y. Gao, M. V. Yakovleva and W. B. Ebner, *Electrochemical and Solid State Letters*, 1998, **1**, 117.

[17] R. J. Gummow and M. M. Thackeray, *J. Electrochem. Soc.*, 1994, **141**, 1178.

[18] L. X. Yuan , Z. H. Wang , W. X. Zhang , X. L. Hu , J. T. Chen , Y. H. Huang and John B. Goodenough, *Energy Environ. Sci*., 2001, **4**, 269–284.

[19] M. M. Thackeray, W. I. F. David, P. G. Bruce and J. B. Goodenough, *Materials Research Bulletin*, 1983, **18**(4), 461–472.

[20] M. M. Thackeray, P. J. Johnson, L. A. Depicciotto and P. G. Goodenough, *J. B. Mater. Res. Bull*., 1984, **19**,179.

[21] M. M. Thackeray and A. J. Dekock, *J. Solid State Chem*.1988, **74**, 414.

[22] A. K. Padhi, K. S. Nanjundaswamy and J. B. Goodenough, *J. Electrochem. Soc.*, 1997, **144**(4), 1188–1194.

[23] http://en.wikipedia.org/wiki/Chevrolet_Volt

[24] B. Dunn, H. Kamath, J. M. Tarascon, *Science*, 2011, **334**, 928-935.

[25] D. W. Murphy and P. A. Christian, *Science*, 1979, **205**, 651–656.

[26] R. R. Haering, J. A. R. Stiles and K. Brandt, *US Patent* No. 4 224 390 (1980).

[27] T. Zheng and J. Dahn, *Carbon Materials for Advanced Technologies*, 1999, 341.

[28] J. C. Arrebola, A. Caballero, J. L. G. Camer, L. Hernen, J. Morales and L. Sanchez, *Electrochem. Commun.*, 2009, **11**, 1061.

[29] M. J. Lindsay, G. X. Wang and H. K. Li, *J. Power Sources*, 2003, **84**, 119-121.

[30] M. Winter and J. O. Besenhard, *Electrochim. Acta*, 1999, **45**, 31.

[31] C. K. Chen, X. F. Zhang and Y. Cui, *Nano Lett*., 2008, **8**, 307.

[32] T. Tatsuma, M. Taguchi and N. Oyama, *Electrochem. Acta*., 2001, **46**, 1201.

[33] Y. Nishi, in Lithium Ion Batteries, M. Wakihara and O. Yamamoto, Editors, p.181, Kodansha Ltd., Tokyo, Japan (1998).

[34] S. Hossain, in *Handbook of Batteries*, 2nd ed., D. Linden, Editor, p. 36.1, McGraw-Hill Inc., New York (1995).

[35] M. Broussely, P. Biensan and B. Simon, *Electrochim. Acta*, 1999, **45**, 3.

[36] C. S. Wang, G. T. Wu and W.Z. Li, *J. Power Sources*, 1998, **76**, 1–10.

[37] M. Winter, Jürgen O. Besenhard, M. E. Spahr and P. Novak, *Adv. Mater*., 1998, **10**(10), 725-763.

[38] B. Gao, A. Kleinhammes, X. P. Tang, C. Bower, L. Fleming, Y. Wu and O. Zhou, *Chem. Phys. Lett*., 1999, **307**, 153–157.

[39] B. Gao, C. Bower, J. D. Lorentzen, A. Kleinhammes, X. P. Tang, L. E. McNeil, Y. Wu and O. Zhou, *Chem. Phys. Lett.*, 2000, **327**, 69.

[40] H. Shimoda, B. Gao, X. P. Tang, A. Kleinhammes, L. Fleming, Y. Wu and O. Zhou, *Phys. Rev. Lett*, 2002, **88**, 015502-1.

[41] Z. H. Yang and H. Q. Wu, *Mater. Lett*. 2001, **50**, 108–114.

[42] F. Leroux, K. Metenier, S. Gautier, E. Frackowiak, S. Bonnamy and F. Beguin, *J. Power Sources*, 1999, **81–82**, 317–322.

[43] A. S. Claye, J. E. Fischer, C. B. Huffman, A. G. Rinzler and R. E. Smalley, *J. Electrochem. Soc*. 2000, **147**, 2845–2852.

[44] S. Iijima, *Nature*, 1991, **354**, 55-58.

[45] S. Yang, J. Huo, H. Song and X. Chen, *Electrochim. Acta*, 2008, **53**, 2238–2244.

[46] C.H. Mi, G.S. Cao, X.B. Zhao, *J. Electroanal. Chem*. 2004, **562**, 217–221.

[47] K. Nishidate and M. Hasegawa, *Phys. Rev*. B. 2005, **71**, 245418(1)–245418(6).

[48] T. P. Kumar, R. Ramesh, Y.Y. Lin and G. Fey, *Electrochem. Commun*., 2004, **6**, 520–525.

[49] S. Kawasaki, T. Hara, Y. Iwai and Y. Suzuki, *Mater. Lett*., 2008, **62**, 2917–2920.

[50] R. S. Morris, B. G. Dixon, T. Gennett, R. Raffaelle and M. J. Heben, *J. Power Sources*, 2004, **138**, 277–280.

[51] G. Maurin, C. Bousquet, F. Henn, P. Bernier, R. Almairac and B. Simon, *Chemical Physics letters*, 1999, **312**, 14-18.

[52] G. Maurin, F. Henn, B. Simon, J. Colomer and J. B. Nagy, *Nano letters*, 2001, **1**, 75-79.

[53] E. Frackowiak, S. Gautier, H. Gaucher, S. Bonnamy and F. Beguin, *Carbon*, 1999, **37**, 61-69.

[54] B. Gao, C. Bower, J. D. Lorentzen, A. Kleinhammes, X. P. Tang, L.E. McNeil, Y. Wu and O. Zhou, *Chem. Phys. Lett*. 2000, **327**, 69.

[55] H. Shimoda, B. Gao, X. P. Tang, A. Kleinhammes, L. Fleming, Y. Wu and O. Zhou, *Phys. Rev. Lett*, 2002, **88**, 1.

[56] Z. H. Yang and H. Q. Wu, *Mater. Lett*., 2001, **50**, 108–114.

[57] G. Maurin, C. Bousquet, F. Henn, P. Bernier, R. Almairac and B. Simon, *Solid State Ionics*, 2000, **137**, 1295–1299.

[58] C. de las Casas, W. Z. Li, *J. Power Sources*, 2012, **208**, 74–85.

[59] T. Zheng and J. Dahn, *Carbon Materials for Advanced Technologies*, 1999, 341.

[60] J. C. Arrebola, A. Caballero, J. L. G. Camer, L. Hernen, J. Morales and L. Sanchez, *Electrochem. Commun.*, 2009, **11**, 1061.

[61] M. Winter and J. O. Besenhard, *Electrochim. Acta*, 1999, **45**, 31.

[62] C. K. Chen, X. F. Zhang and Y. Cui, *Nano Lett*., 2008, **8**, 307.

[63] B. A. Boukamp, G. C. Lesh and R. A. Huggins, *J. Electrochem. Soc.*, 1981, **128**, 725.

[64] C. J. Wen and R. A. Huggins, *J. Solid State Chem.*, 1981, **37**, 271.

[65] W. J. Weydanz, M. Wohlfahrt-Mehrens and R. A. Huggins, *J. Power Sources,* 1999, **237**, 81–82.

[66] B. Gao, S. Sinha, L. Fleming and O. Zhou, *Adv. Mater.*, 2001, **13**, 816.

[67] H. Li, X. Huang, L. Chen, G. Zhou, Z. Zhang, D. Yu, Y. J. Mo and N. Pei, *Solid State Ionics*, 2000, **135**, 181.

[68] P. Limthongkul, Y. I. Jang, N. J. Dudney and Y.-M. Chiang, *Acta Mater.*, 2003, **51**,

1103.

[69] A. Netz, R. A. Huggins and W. Weppner, *J. Power Sources*, 2003, 95, 119–121.

[70] M. N. Obrovac and L. Christensen, *Electrochem. Solid-State Lett.*, 2004, **7**, A93.

[71] T. D. Hatchard and J. R. Dahn, *J. Electrochem. Soc*., 2004, **151**, A838.

[72] J. Li and J. R. Dahn, *J. Electrochem. Soc*., 2007, **154**, A156.

[73] J. H. Ryu, J. W. Kim, Y. E. Sung and S. M. Oh, *Electrochem. Solid-State Lett*., 2004, **7**, A306.

[74] H. Wua and Y. Cui, *Nano Today*, 2012, **7**, 414-429.

[75] J. Graetz, C. C. Ahn, R. Yazami and B. Fultz, *J. Electrochem. Soc*., 2004, **151**, A698-A702.

[76] C. S. Fuller and J. C. Severiens, *Phys. Rev*. 1954, **96**, 21.

[77] Y. Idota, *US Pat*., 5 478 671, 1995.

[78] H. Tomyama, *Jpn Pat*., 06-029608, 1995.

[79] Y. Idota, T. Kubota, A. Matsufuji, Y. Maekawa and T. Miyasaka, *Science*, 1997, **276**, 1395.

[80] I. A. Courtney and J. R. Dahn, *J. Electrochem. Soc.*, 1997, **144**, 2045.

[81] D. Aurbach, A. Nimberger, B. Markovsky, E. Levi and A. Gedanken, *Chem. Mater.*, 2002, **14**, 4155.

[82] A. P. Hightower, P. Delcroix, G. LeCaer, C. K. Huang, B. V. Ratnakumar, C. C. Ahn and B. Fultz, *J. Electrochem. Soc.*, 2000, **147**, 1.

[83] R. Alcántara, F. J. Fernandez-Madrigal, C. Perez-Vicente, J. L. Tirado, J. C. Jumas, J. Olivier-Fourcade, *Chem. Mater.*, 2000, **12**, 3044.

[84] U. Kasavajjula, C. Wang and A. John Appleby, *J. Power Sources*, 2007, **163**, 1003.

[85] S. H. Lee, Y. H. Kim, R. Deshpande, P.A. Parilla, E. Whitney, D.T. Gillaspie, K.M. Jones, A.H. Mahan, S. Zhang, and A.C. Dillon, *Adv. Mater.*, 2008, **20**, 3627.

[86] P. Poizot, S. Laruelle, S. Grugeon, L. Dupont, and J. M. Tarascon, *Nature*, 2000, **407**, 496.

[87] M. S. Park, G. X. Wang, Y. M. Kang, D. Wexler, S. X. Dou and H. K. Liu, *Angew. Chem. Int. Ed*., 2007, **46**, 750-753.

[88] Y. Nagao, H. Sakaguchi, H. Honda, T. Fukunaga and T. Esaka, *J. Electrochem. Soc*., 2004, **151**(10), A1572-A1575.

[89] http://www.sony.net/SonyInfo/News/Press/200502/05-006E/.

[90] A. Finke, P. Poizot, C. Guéry, and J. M. Tarascon, *J. Electrochem. Soc*., 2005, 152(12) ,2364.

[91] A. D. W. Todd, R. E. Mar and J. R. Dahn, *J. Electrochem. Soc*., 2006, **153**(10), A1998-A2005.

[92] A. D. W. Todd, R. E. Mar and J. R. Dahn, *J. Elecrochem. Soc*., 2007, **154**(6), A596-A604.

[93] P. P. Ferguson, A. D. W. Todd and J. R. Dahn, *Electrochem. Commun*., 2008, **10**, 25–31.

[94] P. P. Ferguson, R. A. Dunlap and J. R. Dahn, *J. Electrochem. Soc*., 2010, **157**(3), A325-A332.

[95] A. D. W. Todd, R. A. Dunlap and J. R. Dahn, *J. Alloys and Compounds*, 2007, **443**, 114–120.

[96] P. P. Ferguson, M. L. Martine, R. A. Dunlap and J. R. Dahn, *Electrochim. Acta*, 2009, **54**, 4534–4539.

[97] P. P. Ferguson, Peng Liao, R. A. Dunlap and J. R. Dahn, *J. Electrochem. Soc*. 2009, **156** (1), A13-A17.

[98] R. B. Lewis, A. Timmons, R. E. Mar and J. R. Dahn, *J. Electrochem. Soc*., 2007, **154** (3), A213-A216.

[99] E. Ferg, R. J. Gummow, A. de Kock and M. M. Thackeray, *J. Electrochem. Soc*., 1994, **141**, A147–A150.

[100] P. Reale, S. Panero, B. Scrosati, J. Garche, M. Wohlfahrt-Mehrens and M. Wachtler, *J. Electrochem. Soc*., 2004, **151**, A2138–A2142.

[101] S. H. Ng, J. Wang, D. Wexler, K. Konstantinov, Z. P. Guo and H. K. Liu, *Angew. Chem., Int. Ed.*, 2006, **45**, 6896–6899.

[102] S. Yoon, C. M. Park and H. J. Sohn, *Electrochem. Solid-State Lett*. 2008, **11**, A42–A45.

[103] J. Yang, Y. Takeda, N. Imanish and O. Yamamoto, *J. Electrochem. Soc*., 1999, **146**, 4009–4013.

[104] J. G. Ren, Q. H. Wu, G. Hong, W. J. Zhang, H. M. Wu, K. Amine, J. B. Yang and S. T. Lee, *Energy Technol*. 2013, **1**, 77–84.

[105] Y. Fan, Q. Zhang, C. X. Lu, Q. Z. Xiao, X. H. Wang and B. K. Tay, *Nanoscale*, 2013, **5**, 1503-1506.

[106] T. Song, J. Xia, J. H. Lee, D. H. Lee, M. S. Kwon, J. M. Choi, J. Wu, S. K. Doo, H. Chang, W. I. Park, D. S. Zang, H. Kim, Y. Huang, K.-C. Hwang, J. A. Rogers and U. Paik, *Nano Lett*., 2010, **10**, 1710–1716.

[107] M. H. Park, M. G. Kim, J. Joo, K. Kim, J. Kim, S. Ahn, Y. Cui and J. Cho, *Nano Lett*., 2009, **9**, 3844–3847.

[108] C. Zhao, Q. Li, W. Wan, J. Li, J. Li, H. Zhou and D. Xu, *J. Mater. Chem*., 2012, **22**, 12193–12197.

[109] L. Su, Z. Zhou and M. Ren, *Chem. Commun*., 2010, **46**, 2590–2592.

[110] A. Esmanski and G. A. Ozin, *Adv. Funct. Mater*., 2009, **19**, 1999–2010.

[111] J. Liu, W. Li and A. Manthiram, *Chem. Commun*., 2010, **46**, 1437–1439.

[112] L. Su, Y. Jing and Z. Zhou, *Nanoscale*, 2011, **3**, 3967–3983.

[113] C. K. Chan, H. Peng, G. Liu, K. McIlwrath, X. F. Zhang, R. A. Huggins and Y. Cui, *Nat. Nanotechnol*., 2008, **3**, 31–35.

[114] Y. Fan, K. Huang, Q. Zhang, Q. Xiao, X. Wang and X. Chen, *J. Mater. Chem*., 2012, **22**, 20870–20873.

[115] H. Kim, B. Han, J. Choo and J. Cho, *Angew. Chem., Int. Ed*., 2008, **47**, 10151–10154.

[116] L. Ji and X. Zhang, *Energy Environ. Sci*., 2010, **3**, 124–129.

[117] X. Li, P. Meduri, X. Chen, W. Qi, M. H. Engelhard, W. Xu, F. Ding, J. Xiao, W. Wang, C. Wang, J. G. Zhang and J. Liu, *J. Mater. Chem*., 2012, **22**, 11014–11017.

CHAPTER 2

EXPERIMENTAL TECHNIQUES

2.1 Mechanical Alloying

Mechanical alloying (MA) is a solid-state powder processing technique involving repeated welding, fracturing, and rewelding of powder particles in a high-energy ball mill. Originally developed to produce oxide-dispersion strengthened (ODS) nickel- and iron-base superalloys for applications in the aerospace industry, MA has now been shown to be capable of synthesizing a variety of equilibrium and nonequilibrium alloy phases starting from blended elemental or prealloyed powders. The nonequilibrium phases synthesized include supersaturated solid solutions, metastable crystalline and quasicrystalline phases, nanostructures, and amorphous alloys.

Mechanical alloying is normally a dry, high-energy ball milling technique and has been employed to produce a variety of commercially useful and scientifically interesting materials. The formation of an amorphous phase by mechanical grinding of a Y-Co intermetallic compound in 1981[1] and in the Ni-Nb system by ball milling of blended elemental powder mixtures in 1983[2] brought about the recognition that MA is a potential nonequilibrium processing technique. Beginning from the mid-1980s, a number of investigations have been carried out to synthesize a variety of stable and metastable phases including supersaturated solid solutions, crystalline and quasi-crystalline intermediate phases, and amorphous alloys.[3-4] Additionally, it has been recognized that

powder mixtures can be mechanically activated to induce chemical reactions, i.e., mechanochemical reactions at room temperature or at least at much lower temperatures than normally required to produce pure metals, nanocomposites, and a variety of commercially useful materials.[5] Efforts were also under way since the early 1990s to understand the process fundamentals of MA through modeling studies.[6] Because of all these special attributes, this simple, but effective, processing technique has been applied to metals, ceramics, polymers, and composite materials.

Different types of high-energy milling equipment are used to produce mechanically alloyed powders. They differ in their capacity, efficiency of milling, and additional arrangement for cooling, heating, etc. A brief description of the different mills is provided below.

In this thesis, 8000D mixer/mill of SPEX CertPrep was used to synthesize composite anode material. The mill has two separate vial sets, which are 35mL round-ended hardened steel grinding vial sets. The vial is 23/8 in. diameter x 3 in. long (6.0 cm x 7.62 cm). Each set includes one screw-on cap, one O-ring, two 1/2 in. (12.7 mm) and four 1/4in. (6.35 mm) steel balls (8001B Hardened Steel Ball Set). Vials are secured in the clamp and swung energetically back and forth several thousand times a minute. Extended Running Time Chip is available for extending timer range to 1,000 or 10,000 minutes. The mill can load a 0.2 - 10 gram sample for grinding or 60 mL for mixing. It reduces samples to analytical fineness and can be utilized for mechanical alloying and nano-milling. A variety of vial materials is available for the SPEX mills and these include hardened steel, alumina, tungsten carbide, zirconia, stainless steel, silicon nitride, agate, plastic, and methacrylate. The majority of the research on the fundamental aspects of MA

has been carried out using some version of these SPEX mills. All specific parameters of SPEX milling machine used in this work are summarized in Table 2-1.

The planetary mill owes its name to the planet-like movement of its vials. Usually, three or four vials rotate around the central axis and simultaneously around their own axes in the opposite direction. Material and milling bodies (usually balls) are loaded into the jars. The treated material particles undergo multiple collisions with the grinding media and the jar walls. Even though the linear velocity of the balls in this type of mill is higher than that in the SPEX mills, the frequency of impacts is much more in the SPEX mills.

Table 2-1 Specifications of SPEX milling machine

Voltage	115V/60Hz or 230V/50Hz
CE Approved	YES
Dimensions	19 in (48cm) x 14 in (36cm) x 18 in (46cm)
Net Weight (lbs)	76 lbs (35kg)
Gross Weight (lbs)	89 lbs (40.4kg)
Motor	1/3 hp, 1725 RPM @ 60Hz, 1425 RPM @ 50Hz
Power Cord	3-prong grounded plug, 115V 60Hz or CEE 7/7 2-prong
Clamp Movement	2 1/3 in (5.9cm) back-and-forth, 1 in (2.5cm) side-to-side
Clamp Speed	1060 cycles/minute (115V) or 875 cycles/minute (230V)
Timer/Controls	100 minute range. Expandable up to 1,000 or 10,000 range.*

* Above data from SPEX CertiPrep.

An attritor (a ball mill capable of generating higher energies) consists of a vertical drum with a series of impellers inside it. Attritors are the mills in which large quantities of powder (from about 0.5 to 40 kg) can be milled at a time. The velocity of the grinding medium is much lower (about 0.5 m/s) than in Fritsch or SPEX mills and consequently, the energy of the attritors is low. The velocity of the grinding medium is much lower (about 0.5 m/s) than in Fritsch or SPEX mills and consequently, the energy of the attritors is low.

In this thesis, a novel design of the planetary mill was used to custom-design a milling machine. This is a dual-drive planetary mill, which can achieve higher grinding rates and better milling effect compared with common mills. This limitation of common mills results from the particles being weakly confined in the breakage zone of these mills. Our custom-made milling machine works by a planetary mill method that creates a very high centrifugal field, confining the particles in the milling area and reducing the “dead zone” effect.[6-9]

2.2 X-ray Diffraction (XRD)

Powder X-ray diffraction is one of the most powerful techniques used for identification of crystal structures. The crystal phases present in all the samples are characterized by high energy X-ray diffraction. All data acquisition and processing were carried out at 11-ID-C of sector 11 (High-energy diffraction beamline) in the Advance Photon Source of the Argonne National Laboratory. 11-ID-C is a fixed high-energy beamline operating at 115 keV and wavelength at 0.10798 Å. It is used for diffraction measurements on both crystalline and amorphous materials using 2D area detection primarily for structural studies or exploration of phase changes. A wide array of ancillary equipment may be

used, in some cases in combination.

2.3 Pair Distribution Function (*PDF*)

The atomic pair distribution function (*PDF*) technique is a powerful tool to study disordered material. In the past for a long time, X-ray diffraction has been the common technique which reveals information about crystal structure, chemical composition, phase identification, crystallinity, etc. However, with increasing complexity of materials, especially that non-equilibrium state material and amorphous alloys become more and more popular in different applications, the traditional crystal structure technique is no longer sufficient to understand properties of materials on atomic scale. The limitation of XRD yields the long-range order of the material. Instead, the Pair Distribution Function technique can give short-range order information.

The *PDF* gives the probability of finding an atom at a given distance r from another atom. In other words, it can be understood as a bond length distribution. In some sense, the *PDF* is similar to the Patterson function well known to crystallographers, but one has to be aware that normally, the Patterson function will only give interatomic vectors within a unit cell corresponding to the average structure since only Bragg intensities contribute to the Fourier transform. The *PDF*, on the other hand, is obtained via the Fourier transform of the total scattering pattern and yields the local structure on length scales beyond the unit cell size.

The *PDF* can be obtained from the powder diffraction data via a Fourier transform of the normalized scattering intensity S(Q) (equation 2.1):

$$G(r) = 4\pi r[\rho(r) - \rho_0] = \frac{2}{\pi}\int_0^\infty Q[S(Q) - 1]\sin(Qr)dQ \qquad (2.1)$$

where $\rho(r)$ is the microscopic pair density, ρ_0 is the average number density, and Q is the magnitude of the scattering vector. For elastic scattering, $Q = 4\pi \sin(\theta)/\lambda$ with 2θ being the scattering angle and λ the wavelength of the radiation used.

All *PDF* tests were tested at 11-ID-C of sector 11 (High-energy diffraction beamline) in the Advance Photon Source of the Argonne National Laboratory. 11-ID-C is a fixed high-energy beamline operating at 115 keV and wavelength at 0.10798 Å.

2.4 X-ray Absorption Spectroscopy (XAS)

X-ray absorption spectroscopy (XAS) is a widely-used technique for the local geometric and/or electronic structure of matter. The experiment is usually performed at synchrotron radiation sources, which provide intense and tunable X-ray beams. Bulk XAS methods have long been important for studying real materials under real conditions, and numerous examples are found in materials and chemical science (i.e., catalysis, batteries and fuel cells), and the environmental sciences. XAS includes both Extended X-ray Absorption Fine Structure (EXAFS) and X-ray Absorption Near Edge Structure (XANES).[10]

XAS is the measurement of the X-ray absorption coefficient (μ(E) in the equations below) of a material as a function of energy. The number of X-ray photons that are transmitted through a sample ($I_t = I_0 e^{-\mu x}$) is equal to the number of X-ray photons showed on the sample (I_0) multiplied by a decreasing exponential that depends on the type of atoms in the sample, the absorption coefficient μ ($\mu = -ln(I_t/I_0)/x$), and the thickness of the sample *x*. When the incident X-ray energy matches the binding energy of an electron of an atom within the sample, the number of X-rays absorbed by the sample increases dramatically, causing a drop in the transmitted X-ray intensity. This results in an

absorption edge. Each element on the periodic table has a set of unique absorption edges corresponding to different binding energies of its electrons. This gives XAS element selectivity. XAS spectra are most often collected at synchrotrons.

There are three main regions found on a spectrum generated by XAS data (Fig. 2-1).[11] The dominant feature is called the "rising edge", and is sometimes referred to as XANES (X-ray Absorption Near-Edge Structure) or NEXAFS (Near-edge X-ray Absorption Fine Structure). The pre-edge region is at energies lower than the rising edge. The EXAFS (Extended X-ray Absorption Fine Structure) region is at energies above the rising edge, and corresponds to the scattering of the ejected photoelectron off neighboring atoms. The combination of XANES and EXAFS is referred to as XAFS.

The special characteristics of the APS allow XAS measurements to be extended into the time regime with sub-100 psec resolution, and with submicron resolution using X-ray microprobes. XAS experiments were carried out at beamline 20-BM-B of the Advanced

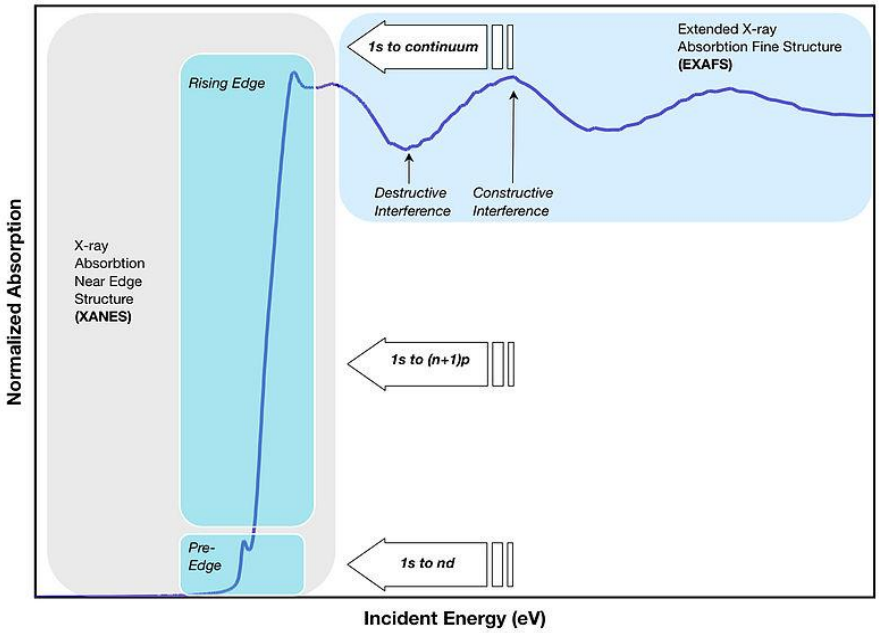

Fig. 2-1 Three regions of XAS data[15]

Photon Source at the Argonne National Laboratory. The incident beam was monochromatized using a Si (111) fixed-exit, double-crystal monochromator. Co K-edge spectra of UHEM and SPEX OAC were acquired in transmission mode utilizing gas ionization chambers as detectors. X-ray Absorption Near Edge Structure (XANES) and Extended X-ray Absorption Fine Structure (EXAFS) data were extracted with established methods. The normalized EXAFS was converted from energy to k-space. These data were then Fourier transformed to R-space.

2.5 Mössbauer Spectroscopy

To make up for the low scattering of XRD for nanostructured or amorphous materials, Mössbauer spectroscopy gives more information about the small-scale structure of a material by probing the material on the atomic scale. Mössbauer spectrometry is based on the “Mössbauer effect”. Mössbauer used solid state absorbers and emitters in gamma ray fluorescence experiments. The recoil energy from single nuclear decay events in a lattice can be too low to excite phonons, which means that for the purpose of recoiling, the decaying nucleus is effectively rigidly bound to all the other nuclei in its crystal lattice. Since the recoil momentum must be imparted to the entire lattice, not just a single nucleus, the kinetic energy that goes into the recoil drops dramatically. This recoilless absorption and emission of gamma rays is known as the Mössbauer effect. Mössbauer spectroscopy is a technique in which interaction between the electromagnetic moment of the nuclear charge and electromagnetic field produced by the extra-nuclear electrons. This interaction gives splitting/shifting of the nuclear energy levels. In our work, Mössbauer spectroscopy was used to identifiy the state of Fe of as-milled samples by their magnetic properties.

2.6 Electrochemical Test

The process of CR 2032-type coin cells involve three steps: 1) slurry, 2) lamination, and 3) cell. The slurry is composed of active material, conductive agent (super P or acetylene black), and binder. Electrode lamination is prepared as a thin film by doctor-blade deposition on a copper or aluminum substrate. The thickness can be adjusted by using a different doctor-blade. The anode material usually is coated on copper foil and aluminum foil is often used on the cathode material. Coin cells are tested on a Maccor battery cycler.

2.7 Reference

[1] A.E. Ermakov, E. E. Yurchikov and V. A. Barinov, *Phys Met Metallogr*, 1981, **52**(6), 50.

[2] C. C. Koch, O. B. Cavin, C. G. McKamey and J. O. Scarbrough, *Appl Phys Lett*, 1983, **43**, 1017.

[3] C. Suryanarayana, *Metals and Materials*, 1996, **2**, 195-209.

[4] B. S. Murty and S. Ranganathan, *Internat Mater Rev*, 1998, **43**, 101.

[5] P. G. McCormick, *Mater Trans Japan Inst Metals*, 1995, **36**, 161.

[6] D. R. Maurice and T. H. Courtney, *Metall Trans*, 1990, **21**, 289-303.

[7] L. Milin and R. K. Rajamani, *Mater. Manufact. Proc*., 1997, **12** (2), 241-260.

[8] J. Lu, Y. J. Choi, Z. Z. Fang, H. Y. Sohn and E. Rönnebro, *J. Am. Chem. Soc*., 2009, **131**(43), 15843-15852.

[9] B. G. Butler, J. Lu, Z. Z. Fang and R. K. Rajamani, *International Journal of Powder Metallurgy*, 2007, **43**(1), 35-43.

[10] http://en.wikipedia.org/wiki/Extended_X-ray_absorption_fine_structure

[11] http://en.wikipedia.org/wiki/X-ray_absorption_spectroscopy

CHAPTER 3

OXIDE/TIN-COBALT-CARBON (OXIDE = TIN OXIDE AND SILICON DIOXIDE) COMPOSITE

3.1 Introduction

Lithium-ion batteries (LIBs) are the state-of-the-art power sources for portable electronics, plug-in hybrid electric vehicles, and pure electric vehicles. The electrode material is the key point to the improvement of the LIB electrochemical properties. As low voltage anodes, three types of material have been developed to date: Li metal, carbonaceous materials, and alloy/oxides.[1-5] Lithium dendrite growth on metal Li anodes represents one of the major safety issues. Carbon material, presently used as the anode in LIBs, is insufficient to meet the future performance requirement because of its low theoretical capacity (372 mAh/g).[6,7] Much attention has been thus paid to silicon and tin because of its high capacity.[8,9] Unfortunately, they suffer from a huge volume expansion and contraction during lithiation and delithiation, which leads to pulverization of the active materials and their becoming “dead particles”. The resulting poor cycle life restricts the practical use.

By contrast, oxides, like tin oxide, appear particularly promising because of their longer cycle life.[8,9] Oxides, like amorphous tin oxide, have attracted much attention for rechargeable lithium ion batteries. The amorphous tin oxide composite can provide theoretical volumetric and gravimetric capacity advantages over carbon of four and two

times, respectively. A series of oxides (MO) were studied extensively, e.g., SiO_x, MoO_3, SnO_2, GeO_2, etc.[10-13] Unfortunately, all of them suffer from volume changes and local stresses, which can induce pulverization and particle cracking. All these can cause irreversibility and poor capacity retention. Hence, future research must focus on finding an anode material combining high capacity and good cyclic performance.

In addition, nanostructured Sn-Co-C alloy as the anode material has been commercialized by SONY, called "Nexelion".[14] Dahn and co-workers studied the Sn-Co-C system, which they fabricated by sputter deposition and mechanical alloying methods.[15-21] The carbon does not act only as a buffering agent. Addition of a sufficient amount of carbon into the $Sn_{1-x}Co_x$ system prevents the tin atoms from aggregating, even though the materials are initially amorphous. The carbon matrix separates the CoSn grains and prevents aggregation of Sn during charge–discharge cycling and leads to excellent charge–discharge capacity retention.

Here we report a series of MO-SnCoC (MO = SnO_2 and SiO_2) as anode material for lithium ion batteries. The MO-SnCoC composite materials have the potential to combine the advantageous properties of both Sn-Co-C (long cycle life) and MO (high capacity) and, thereby, improve the overall electrochemical performance eventually.

3.2 Experimental Procedure

3.2.1 Preparations of the MO-$Sn_xCo_yC_z$ Composites

The raw material for this work, Tin oxide (SnO_2, 99.99%, -325 mesh, Sigma-Aldrich), Silicon dioxide (SiO_2, 99%, powder, Sigma-Aldrich), Tin (Sn, 99%, powder, Sigma-Aldrich), Cobalt (Co, 99.5%, -325 mesh, Alfa Aesar) and Graphite from Hitachi were purchased. Then, these powders were blended with a weight ratio of 50 wt.% SnO_2/50

wt.% $Sn_xCo_yC_z$ (*x*, *y, z* atomic ratio: 30/30/40) and 50 wt.% SiO_2/50 wt.% $Sn_xCo_yC_z$ (*x*, *y, z* atomic ratio: 30/30/40), respectively, using a mixing machine overnight to obtain a homogeneous distribution. Around 5 grams of the mixture powders were milled with 200 grams 1/4 and 1/8 inch diameter stainless steel balls using a SPEX milling machine (8000D Mixer/Mill) for 48 hours. All the handling processes for ball milling were carried out in a glove box filled with purified argon to avoid oxidation.

3.2.2 Electrochemical and Physical Characterization

To characterize the as-milled samples electrochemically, the MO-$Sn_xCo_yC_z$ negative electrodes were assembled in a CR 2032-type coin cell configuration. Charge-discharge profiles and cycle performance data were collected using a Maccor battery cycler (Maccor, Inc., Tulsa). The laminates were prepared as thin film by doctor-blade deposition (150 μm) on a copper substrate of a slurry composed of 80 wt.% active materials, 10 wt.% acetylene black as the conductive agent, and 10 wt.% polyimide binder. The binder was solidified and NMP was completely evaporated at 300 ^oC in an argon-flowed oven for 2 hours. The loading density of the active material was around 6.5 mg/cm^2. The electrode area is 1.6 cm^2. Lithium foil served as the counter electrode and the electrolyte consisted of a 3:7 w/w mixture of ethylene carbonate and ethyl methyl carbonate, with 1.2 M $LiPF_6$. The cells were assembled in an argon-filled glove box and tested in the cut-off potentials of 0.005 and 2.5 V. The cells were charged and discharged at a current of 100 mA/g for 2 cycles and then cycled upon a fixed current of 300 mA/g. In order to test the rate capability, different current rates (50 mA/g, 100 mA/g, 200 mA/g, 400 mA/g, 600 mA/g, 800 mA/g, 1000 mA/g, and 100 mA/g) were loaded on the composite electrodes.

The morphology of as-milled MOAC was visualized via Quanta 600 scanning electron microscopy (SEM). The ex situ experimental powder diffraction data and pair distribution function (*PDF*) data were collected at 11-ID-C beam line at the Advanced Photon Source of the Argonne National Laboratory. The wavelength of X-ray used was preset to 0.10798 Å (fixed wavelength for this sector). The high-energy X-ray source is important for obtaining excellent penetration capability to detect structural changes and collecting diffraction data at high wave vectors. The high flux of the X-ray beam at APS is an advantage to carry out fast experiments at one spectrum per minute. The samples were loaded in a cylindrical geometry glass capillary (d=0.5mm). The detector was set up at a different distance to samples for diffraction and *PDF*. For the *PDF* test, 30 spectras were collected to reduce the error at high angle. The final *PDF* data are the average of these 30 spectras. The *PDF*gui software was employed to simulate the *PDF* profile of the composites.

3.3 Material Characterization and Electrochemical Properties of 50 wt.%MO-50 wt.%$Sn_{30}Co_{30}C_{40}$ (SnO_2 and SiO_2)

Fig. 3-1 shows SEM images of the SnO_2 composite and SiO_2 composite anode materials. They show very similar morphology. It can be seen that the particles do not have uniform geometric shape and homogeneous particle size distribution. The particle size ranges are from nanoparticles to micron size particles. The overall particles of ball-milled samples consist of agglomerated nanoscale primary particles. This morphology is common for the ball milled powder because of the existence of dead zones in the milling jar. Some big particles stack at dead zones as to be not grounded intensively. The particle size is an important factor for the performance of batteries, which is related to the Li^+ ion

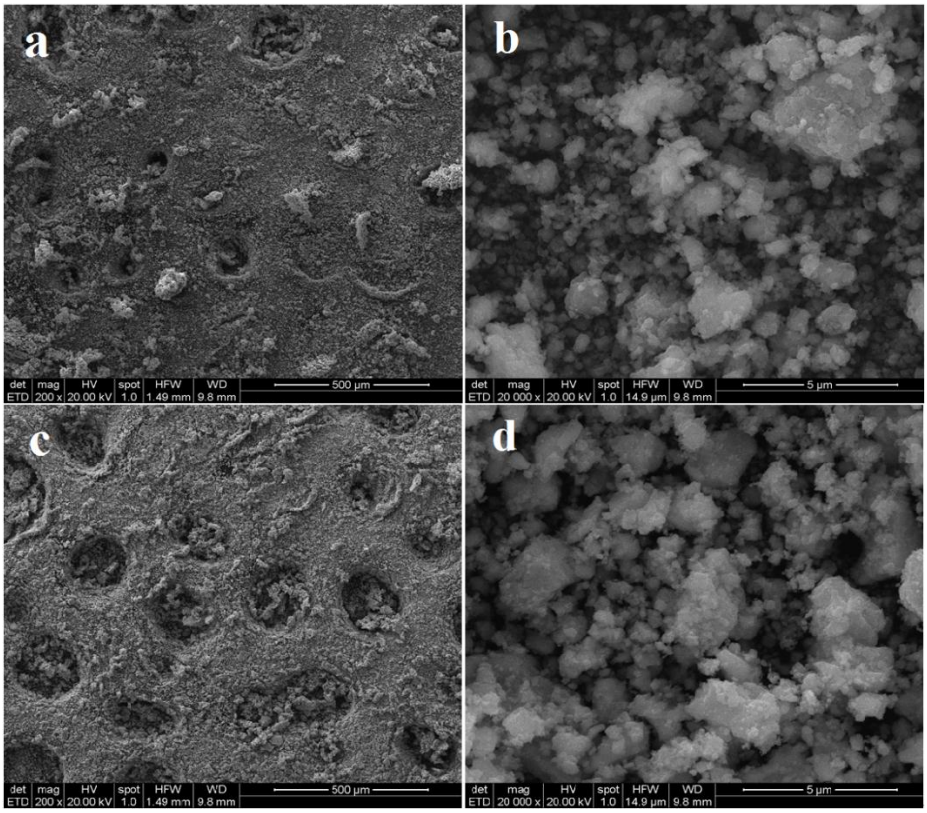

Fig. 3-1 SEM images of the composite samples a) SnO_2 composite (200x), b) SnO_2 composite (20,000x), c) SiO_2 composite (200x), and d) SiO_2 composite (20,000x) after SPEX ball milling

diffusion kinetics and battery lifespan closely. From this point, nanostructured material is good at battery performance.

In order to identify crystalline structure, X-ray diffraction patterns of ball-milled SnO_2 composite and SiO_2 composite are given in Fig. 3-2. The main peaks for as-milled SnO_2 composite powder correspond well with SnO_2 (Tetragonal, *P42/mnm*). The five strong peaks match well with (1 1 0), (1 0 1), (2 0 0), (2 1 1), and (2 2 0) planes of tetragonal SnO_2 powder. Crystal structured Sn, Co, Sn-Co alloys peaks are not detected, which means that they exist in the form of an amorphous or highly distorted state. The XRD pattern of SiO_2 composite shows four detectable peaks, corresponding to *d* values of 2.729 Å, 2.124 Å, 2.038 Å, and 1.935 Å, respectively. However, they cannot be identified

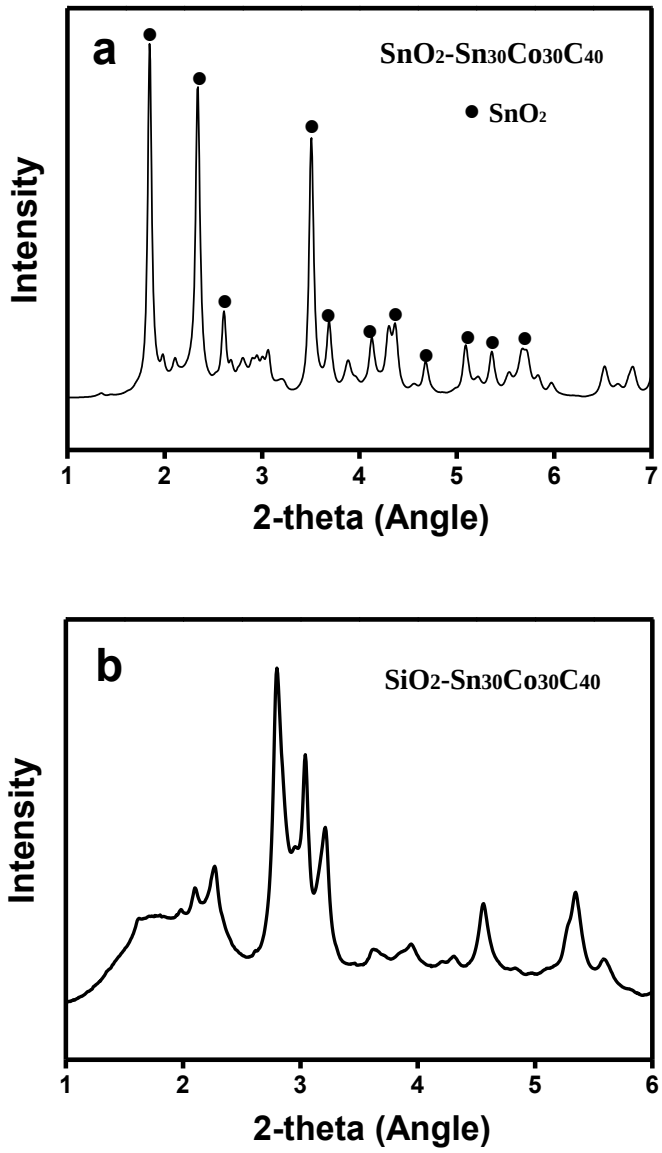

Fig. 3-2 XRD patterns of as-milled a) SnO_2 composite and b) SiO_2 composite powder

by standard cards in the JCPDS database. A broad peak is also apparent at low angle, which can be attributed to an amorphous phase. The strange peaks might be associated with an unknown structure, which is formed during the milling process. Although the MA technique is relatively simple, the physical mechanisms involved are not yet fully understood. A better understanding is desirable in future research. This unknown phase might be associated with anomalous electrochemical capacity. Other techniques should

be used to study the local structure of amorphous material.

Because of the low X-ray scattering, X-ray diffraction is inadequate to characterize amorphous material. Hence, X-ray pair distribution function (*PDF*) analysis has been employed to probe local structures that are correlated with specific electrochemical properties. Recently, *PDF* analysis has been successfully used to investigate short-range order in lithium-ion battery electrode materials.[22] The *PDF* technique considers total scattering (Bragg and diffuse scatterings) and converts it to real space by a Fourier transformation, while standard XRD patterns only contain information about the long-range average structure. The G(r) gives the probability of finding an atom at a distance r from another atom and can be considered as a bond length distribution. PDF technique is a highly effective tool for characterizing those materials that do not possess the periodicity of a crystal structure. In this work, we performed a series of PDF experiments to study the local structure of oxide composites. Fig. 3-3a shows the *PDF* patterns of SnO_2 and as-milled SnO_2 composite. The main inter-atomic distance peaks of SnO_2 appear at 2.052 Å (peak 1), 3.186 Å (peak 2), 3.710 Å (peak 3), and 4.738 Å (peak 4), corresponding to the atomic distance of Sn-O (1^{st} correlation), Sn-Sn (1^{st} correlation), Sn-Sn (2^{nd} correlation), and Sn-Sn (3^{rd} correlation), respectively. These peaks also appear in the pattern of SnO_2 composite, which is consistent with the XRD pattern of SnO_2 composite. Sn, Co, or Sn-Co alloys are not detected in previous XRD results, which may exist as an amorphous state. The peak 2 of SnO_2 composite corresponds to the atomic distance of Co-Sn belonging to the 1^{st} correlation of CoSn. Obviously, SnO_2 composite consists of SnO_2 and amorphous CoSn. The *PDF* pattern of SiO_2 exhibits a short range order, which demonstrates that the pristine SiO_2 is an amorphous material. Atoms of SiO_2

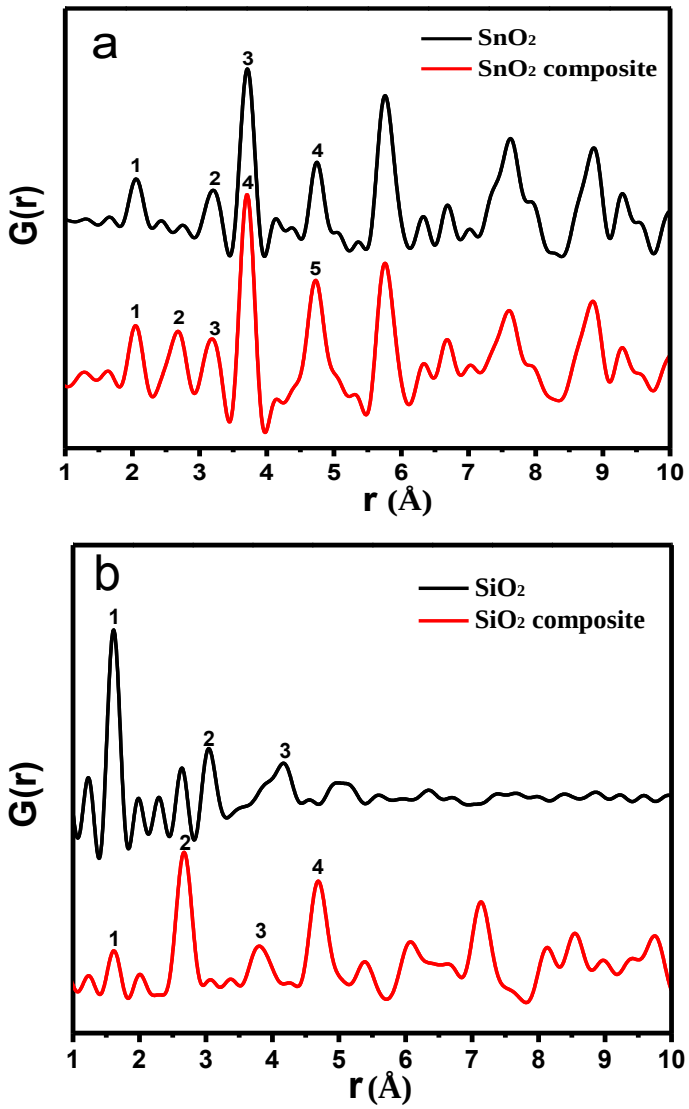

Fig. 3-3 Pair distribution function profile of (a) SnO_2, SnO_2 composite, and $Sn_{30}Co_{30}C_{40}$, (b) SiO_2, SiO_2 composite, and $Sn_{30}Co_{30}C_{40}$

are organized in the range from 0 to 5 Å (Fig. 3-3b). The peaks located at 1.62 Å (peak 1), 3.058 Å (peak 2), and 4.367 Å (peak 3) correspond to the atomic distance of Si-O (1st correlation), Si-Si (1st correlation), and Si-Si (2nd correlation), respectively. It loses the crystal structure in long range (over 5 Å), which is imaged on the *PDF* curve that trends to flat. The atomic distances Co-Sn (2.619 Å), Sn-Sn (3.718 Å), and Co-Sn (4.572 Å) of CoSn alloy can be observed clearly in the *PDF* pattern of SiO_2 composite, which implies

the existence of amorphous CoSn alloy. The interatomic distances of oxides and oxide composites are summarized in Table 3-1. The oxide composite can be considered as two parts: oxide and Sn-Co-C alloy. In order to understand the phase of as-milled $Sn_{30}Co_{30}C_{40}$, we carry out an auxiliary experiment in which pristine tin, cobalt, and carbon are milled in molar ratio 30:30:40 as a reference sample. *PDF*gui is employed to simulate the experimental curve shown in Fig. 3-4. The milled $Sn_{30}Co_{30}C_{40}$ pattern presents three peaks: 2.62 Å, 3.72 Å, and 4.64 Å, which correspond to the CoSn phase. The CoSn phase is fitting with the experimental curve very well. Therefore, it is certain that the CoSn was formed in oxide composite material after milling.

Table 3-1 The interatomic distance of MO and MO composite (MO=SnO_2 and SiO_2)*

Sample	Peak 1(Å)	Peak 2(Å)	Peak 3(Å)	Peak 4(Å)	Peak 5(Å)
SnO_2	Sn-O (2.052)	Sn-Sn (3.186)	Sn-Sn (3.710)	Sn-Sn (4.738)	-
SnO_2 composite	2.052	2.619	Sn-Sn (3.186)	Sn-Sn (3.710)	Sn-Sn (4.738)
SiO_2	Si-O (1.62)	Si-Si (3.058)	Si-Si (4.367)	-	-
SiO_2 composite	1.61	2.62	3.77	4.6	-
CoSn	Co-Sn (2.619)	Sn-Sn (3.718)	Co-Sn (4.572)	-	-

* All bond distance information in the table from ICSD database

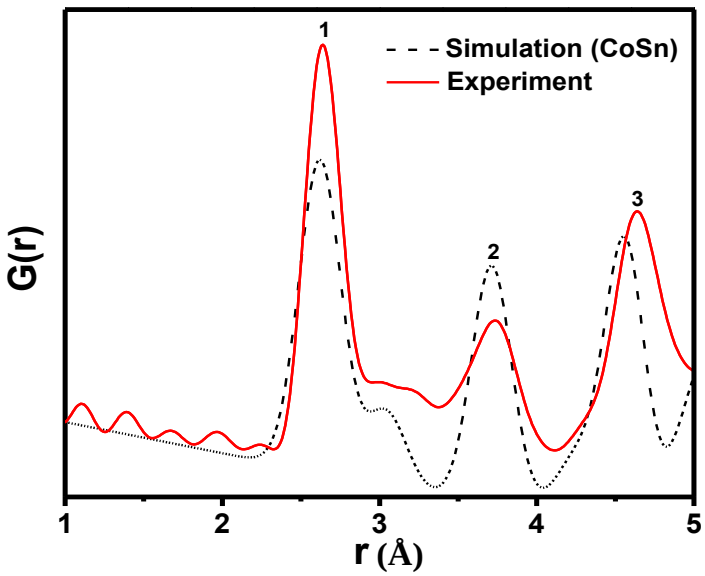

Fig. 3-4 *PDF* patterns of $Sn_{30}Co_{30}C_{40}$ (experiment and simulation)

Fig. 3-5 shows the discharge-charge profiles of three oxide alloy composites electrodes at a constant current of 100 mA/g with the cut-off potentials of 0.005 and 2.5 V. It can be seen that SnO_2 has a flat plateau located around 0.9 V in Fig. 3-5a. However, the SnO_2 composite electrode shows a sloping voltage curve, which may be associated with grain size. Due to the voltage plateau of the SnO_2 electrode, the average discharge voltage is higher than that of the SnO_2 composite electrode, which means the SnO_2 composite anode can obtain higher energy density. The SnO_2 electrode shows the first discharge-charge capacities of 2010 mAh/g and 1324 mAh/g, implying the first cycle Coulombic efficiency of 65%. SnO_2 composite shows a discharge capacity of 1267 mAh/g and charge capacity of 818 mAh/g, respectively, at the first cycle, corresponding to 64.5% Coulombic efficiency. The SiO_2 electrode exhibits little capacity at the first cycle and then decrease to almost zero at the second cycle (Fig. 3-5b). Pristine SiO_2 is an inactive material as the anode for lithium batteries. SiO_2 composite delivers a discharge capacity

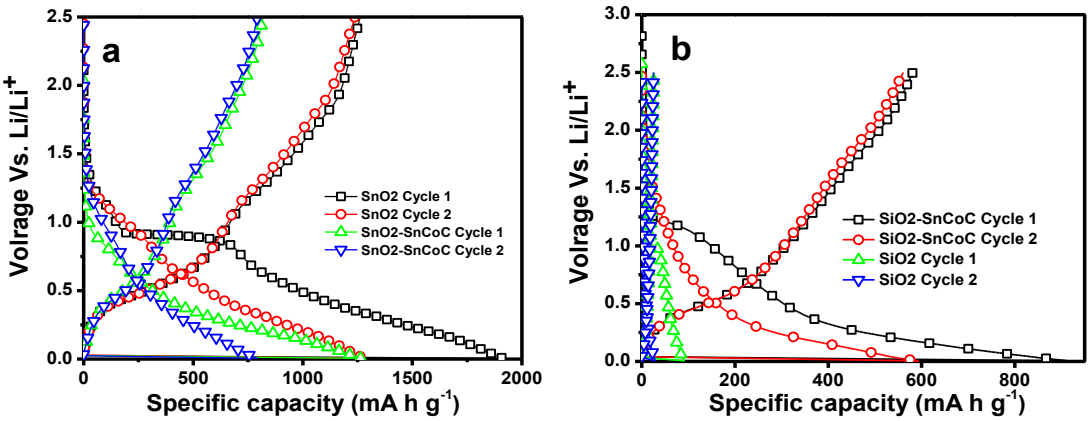

Fig. 3-5 Voltage profile of oxides and oxide composites (oxide=SnO_2 and SiO_2)

of 914 mAh/g and charge of 580 mAh/g at the first cycle. According to *PDF* result, CoSn alloy as amorphous state is detected after milling. Assuming that the lithium ion intercalation occurs according to the equation 3.1[23]

$$4.4Li + CoSn \rightarrow Li_{4.4}Sn + Co \qquad (3.1)$$

The estimated theoretical capacity is 664 mAh/g for CoSn. Obviously, the delivered capacity of SiO_2 composite is more than the theoretical capacity of CoSn alloy. Assuming that all capacity is from CoSn alloy, the excess anomalous capacity is delivered by SiO_2.

Fig. 3-6 compares the cycleability of different oxides (SnO_2 and SiO_2) and oxide composites electrodes between 0-2.5 V upon a constant current of 300 mA/g. The cyclic performance of SnO_2 and SnO_2 composite are shown in Fig. 3-6a. The SnO_2 electrode delivers ~800 mAh/g specific capacity at initial cycles, which is much higher than that (~400 mAh/g) of the SnO_2 composite electrode. However, the SnO_2 electrode exhibits continuous capacity fade within 50 cycles, and then suffers from degradation sharply in following cycles. The SnO_2 composite retains a capacity of 400 mAh/g after 100 cycles without any degradation. Although SnO_2 composite exhibits good cyclic performance, it

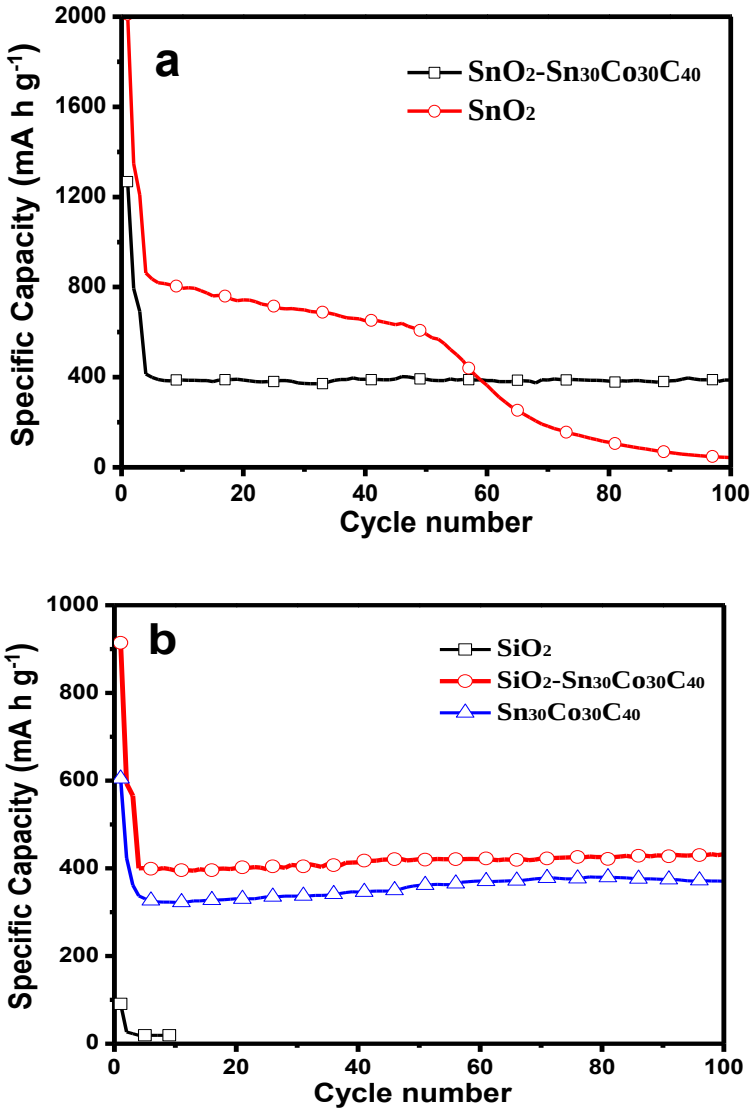

Fig. 3-6 Cyclic performance of oxides and oxide composites (oxide=SnO_2 and SiO_2)

improves little capacity compared with the carbon anode (specific capacity, 372 mAh/g). In Fig. 3-6b, SiO_2 is known as an inactive material for lithium-ion batteries. The capacity of the SiO_2 electrode drops abruptly to almost zero in five cycles. By contrast, the SiO_2 composite electrode exhibits more than 400 mAh/g and maintains steadily over 100 cycles. Tin-cobalt-carbon milled at a molar ratio of 30:30:40 is loaded into the same test program, which delivers 380 mAh/g. Based on a simple calculation, SiO_2 composite

involves 50 wt.% SiO_2 and 50 wt.% $Sn_{30}Co_{30}C_{40}$. Assuming that only Sn-Co-C was able to react with Li^+ ion and SiO_2 is inert, SiO_2 composite electrode should exhibit specific capacity around 190 mAh/g. Apparently, it delivers much more capacity than the calculation. In other words, SiO_2 is activated for lithium insertion after milling. As to the mechanism, we need to work on future research.

The rate capability of oxide (SnO_2 and SiO_2) composite cycled between 0 and 2.5 V has also been investigated. As shown in Fig. 3-7a, the different current densities were loaded in steps from 50 mAh/g to 1200 mAh/g and then back to 100 mAh/g and held on each rate for 3 cycles. The specific capacity of the SnO_2 composite electrode decreases from 945 to 121 mAh/g when the current rate increased respectively from 100 to 1200 mA/g, and the capacity returns to 709 mA/g at 100 mA/g, shown in Fig. 3-7b. Therefore, SnO_2 composite has a poor rate capability. The specific capacity of the SiO_2 composite electrode decreases from 495 to 211 mAh/g when the current rate increased respectively from 100 to 1200 mA/g, and the capacity returns to 450 mA/g when the current was switched 100 mA/g. The SiO_2 composite exhibits the best rate capability among the three oxide composite anode materials.

3.4 Conclusion

In this work, we have developed and characterized a series of oxide composite anode material (MO = SnO_2 and SiO_2) for lithium batteries and investigated its electrochemical performance. Due to the buffer effect of tin-cobalt-carbon, the capacity retention of oxide gains remarkable improvement, compared with pure oxide. The improvement of cycle life could be achieved for oxide composite. The SnO_2 composite retains a capacity of 400 mAh/g with slight degradation in 100 cycles. X-ray diffraction reveals that SnO_2 has non-

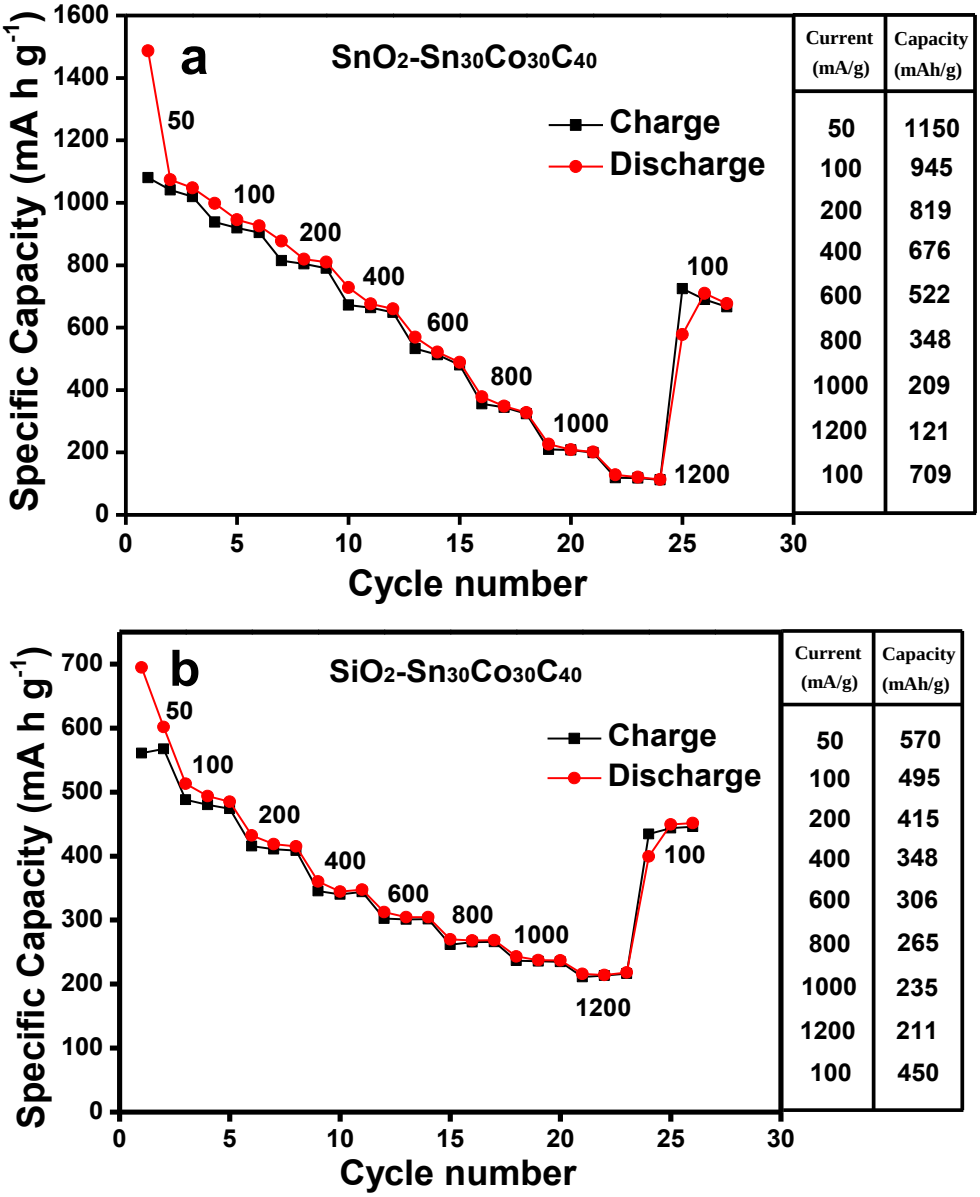

Fig. 3-7 Rate performance of oxides and oxide composites (oxide=SnO_2 and SiO_2)

chemically reacted with Sn-Co-C. Therefore, SnO_2 composite has a poor rate capability. The SiO_2 composite exhibits anomalous capacity. The mechanism of anomalous capacity delivered by SiO_2 composite remains unclear, but it shows very stable cycling performance and rate capability.

3.5 Reference

[1] C. J. Wen and R. A. Huggins, *J. Electrochem. Soc*., 1981, **128**, 1181.

[2] R. Yazami and P. Touzain, *J. Power Sources*, 1983, **9**, 365.

[3] A. M. Wilson, J. N. Reimers, E. W. Fuller, and J. R. Dahn, *Solid State Ionics*, 1994, **74**, 249.

[4] J. Yang, M. Wachtler, M. Winter and J. O. Besenhard, *Solid-State Lett*., 1999, **2**(4), A161.

[5] P. Poizot, S. Laruelle, S. Grugeon, L. Dupont and J. M. Tarascon, *Nature*, 2000, **407**, 495-373.

[6] T. Tran, J. Feikert, X. Song and K. Kinoshita, *J. Electrochem. Soc*., 1995, **142**, 3297.

[7] B. A. Johnson and R. E. White, *J. Power Sources*, 1998, **70**, 48.

[8] Y. Idota, M. Nishima, Y. Miyaki, T. Kubota, T. Miyasaki, EP0651450A1, 1994.

[9] Y. Idota, et al. *Science*, 1997, **276**, 1395.

[10] U. Kasavajjula, C. Wang and A. John Appleby, *J. Power Sources*, 2007, **163**, 1003.

[11] S. H. Lee, Y. H. Kim, R. Deshpande, P. A. Parilla, E. Whitney, D. T. Gillaspie, K. M. Jones, A. H. Mahan, S. Zhang and A. C. Dillon, *Adv. Mater.*, 2008, **20**, 3627.

[12] P. Poizot, S. Laruelle, S. Grugeon, L. Dupont and J. M. Tarascon, *Nature*, 2000, **407**, 496.

[13] M. S. Park, G. X. Wang, Y. M. Kang, D. Wexler, S. X. Dou and H. K. Liu, *Angew. Chem. Int. Ed*., 2007, **46**, 750-753.

[14]
Sony News Release, accessed at http://www.sony.net/SonyInfo/News/Press/200502/05-006E/.

[15] A. D. W. Todd,R. E.Mar and J. R.Dahn, *J. Electrochem. Soc*., 2006, **153**(10), 1998.

[16] A. D. W. Todd, R. E. Mar and J. R. Dahn, *J. Elecrochem. Soc*., 2007, **154**(6), 597.

[17] P. P. Ferguson, A. D. W. Todd and J. R. Dahn, *Electrochem. Commun*., 2008, **10**, 25.

[18] P. P. Ferguson, R. A. Dunlap and J. R. Dahn, *J. Electrochem. Soc*., 2010, **157**(3), 326.

[19] A. D. W. Todd, R. A. Dunlap and J. R. Dahn, *J. Alloys and Compounds*, 2007, **443**, 114.

[20] P. P. Ferguson, M. L. Martine, R. A. Dunlap and J. R. Dahn, *Electrochim. Acta*, 2009, **54**, 4534.

[21] P. P. Ferguson, Peng Liao, R. A. Dunlap and J. R.Dahn, *J. Electrochem. Soc.*, 2009, **156**(1), 13.

[22] B. Key, M. Morcrette, J. M. Tarascon and C. P. Grey, *J. Am. Chem. Soc*. 2011, **133**(3), 503–512.

[23] Jing-jun Zhang and Yong-yao Xia, *J. Electrochem. Soc*., 2006, **153**(8), A1465-A1471.

CHAPTER 4

GERMANIUM OXIDE/TIN-COBALT-CARBON COMPOSITE

4.1 Introduction

In recent years, there is a great interest in developing novel anode materials for high-performance Li ion batteries, particularly in seeking higher-density alternatives for a graphite anode, which has a limited theoretical specific capacity of 372 mAh/g. The ideal anode material for the next generation should meet the following requirements: large reversible capacity, high coulombic efficiency, safe potential, good rate capability, and stable cycle life. Many studies have been devoted to the development of metal alloy anodes because of high capacity such as Si, Ge, Sn, and Sb.[1-6] Among them, Si and Ge are the two most promising stars.[6-9] Although Ge has attracted less attention than Si because of its higher cost, the diffusivity of Li in Ge is 400 times higher than that in Si at room temperature, indicating that Ge may be an attractive electrode material for high-power-rate anodes.[10,11] Theoretically, Ge can uptake 4.4 Li, corresponding to 1623 mAh/g specific capacity. Meanwhile, the huge volume change is up to 370% accompanying de/alloying with lithium, which is the fatal factor for cycle life. To minimize such volume strain during charge and discharge, multiple approaches are proposed, including (i) nano dimensional size (e.g., nanoparticles, thin films, porous structure),[12,13,14] (ii) 3D structure, like nanowires, nanotubes, and nanofibers,[15,16,17] (iii) mixing with a buffer component, such as Ge/carbon, Ge/graphene, and GeO_2.[18,19]

Although these above-mentioned methods can prolong the cell life with an alloy anode, meanwhile, energy density of cells also has inflicted considerable loss due to low loading mass or tap density. Therefore, alloy anode materials arouse little interest of commercial use.

In this work, we proposed a kind of new oxide composite anode material for lithium-ion batteries prepared by a simple and cheap method. This composite material was synthesized by mechanical milling of germanium oxide (GeO_2) and tin-cobalt-carbon. Compared with metallic Ge, GeO_2 has several advantages, such as better cycle life, high theoretical capacity (1126 mAh/g), and lower cost. Nevertheless, the cycle life of oxides is still far from practical use. Amorphous ternary Sn-Co-C nanostructured alloy was developed by SONY as the anode material for lithium-ion batteries.[20] Dahn's group studied various compositions of $Sn_xCo_yC_z$ using magnetron sputtering and mechanical milling methods.[21-28] Combinatorial electrochemical studies of $Sn_{1-x}Co$ ($0<x<0.6$) and $[Sn_{0.55}Co_{0.45}]_{1-y}C_y$ ($0<y<0.5$) series prepared by magnetron sputtering was studied minutely. Composition near $Sn_{30}Co_{40}C_{40}$ shows the best electrochemical performance. They also synthesized $Sn_{30}Co_{40}C_{40}$ using mechanical alloying, which had a specific capacity of 450 mAh/g in 100 cycles. The GeO_2-SnCoC composite material has the potential of combining the advantageous properties of both GeO_2 (high capacity) and SnCoC (long cycle life) and, thereby, improving the overall electrochemical performance eventually.

MA is a common metal processing method, which has many advantages, such as low temperature processing, relatively inexpensive equipment, and the possibility of scaling up, etc. Another interesting feature related to MA is the possibility of producing phases

that usually require extreme conditions, like high temperatures or pressures (or both) to be formed, at room temperature and pressure. Some high temperature phases and non-equilibrium alloy phases can be achieved by MA. Besides, MA is also known to produce nano-sized particles and is mostly used for improving electrochemical properties.[29,30]

4.2 Experimental Procedure

4.2.1 Preparations of the GeO_2-$Sn_{30}Co_{30}C_{40}$ Composites

The raw materials for this work, Germanium oxide (GeO_2, 99.99%, powder, Sigma-Aldrich), Tin (Sn, 99%, powder, Sigma-Aldrich), and Cobalt (Co, 99.5%, -325 mesh, Alfa Aesar) were purchased. Graphite is surface-modified graphite (SMG) NAL1-10C from Hitachi. Then, these powders were blended with a weight ratio of 50 wt.% GeO_2/50 wt.% $Sn_xCo_yC_z$ (*x*, *y, z* atomic ratio: 30/30/40) using a mixing machine overnight to obtain a homogeneous distribution. Around 5 grams of the mixture powders were milled with 200 grams of 1/4 and 1/8 inch diameter stainless steel balls using a SPEX milling machine (8000D Mixer/Mill) for 48 hours. All the handling processes for ball milling were carried out in a glove box filled with purified argon to avoid oxidation.

4.2.2 Electrochemical and Physical Characterization

To characterize the as-milled samples electrochemically, the GeO_2-$Sn_xCo_yC_z$ negative electrodes were assembled in a CR 2032-type coin cell configuration. Charge-discharge profiles and cycle performance data were collected using a Maccor battery cycler (Maccor, Inc., Tulsa). The laminates were prepared as thin film by doctor-blade deposition (150 μm) on a copper substrate of a slurry composed of 80 wt.% active materials, 10 wt.% acetylene black as the conductive agent, and 10 wt.% polyimide binder. The binder was solidified and NMP was completely evaporated at 300 ^oC in an

Argon-flowed oven for 2 hours. The loading density of the active material was around 3 mg/cm^2. The electrode area is 1.6 cm^2. Lithium foil served as the counter electrode and the electrolyte consisted of a 3:7 w/w mixture of ethylene carbonate and ethyl methyl carbonate, with 1.2 M $LiPF_6$. The cells were assembled in an argon-filled glove box and tested in the cut-off potentials of 0.005 and 2.5 V. The cells were charged and discharged at current 100 mA/g for 2 cycles and then cycled upon a fixed current 300 mA/g. In order to test the rate capability, different current rates (50 mA/g, 100 mA/g, 200 mA/g, 400 mA/g, 600 mA/g, 800 mA/g, 1000 mA/g, and 100 mA/g) were loaded on the composite electrodes.

The morphology of as-milled GeO_2 composite was visualized via Quanta 600 scanning electron microscopy (SEM). The particle size distribution of as-milled sample was determined by a Cilas 1090 particle size analyzer (PSA), with a measurement range of 0.04−500 μm. The specific surface area was tested on a NOVA 2200e instrument and calculated by the Brunauer−Emmett−Teller (BET) method. In order to study the structural changes during de/lithiation, the cells were discharged and charged to the fixed potential cutoff and relaxed on open circuit. Then, cells were disassembled in an Argon-filled glove box. The active material was scratched off and packed in polyimide tube for material characterization.

The ex-situ experimental powder diffraction data and pair distribution function (PDF) data were collected at 11-ID-C beam line at the Advanced Photon Source of the Argonne National Laboratory. The wavelength of X-ray used was preset to 0.10798 Å (fixed wavelength for this sector). The high-energy X-ray source is important for obtaining excellent penetration capability to detect structural changes and collect diffraction data at

high wave vectors. The high flux of the X-ray beam at APS is advantage to carry out fast experiments at one spectrum per minute. The samples were loaded in a cylindrical geometry glass capillary (d=0.5mm). The detector was set up at a different distance to samples for diffraction and PDF. For the PDF test, 30 spectras were collected to reduce the error at high angle. The final PDF data are the average of these 30 spectras.

XAS experiments were carried out at beamline 20-BM-B of the Advanced Photon Source at the Argonne National Laboratory. The incident beam was monochromatized using a Si (111) fixed-exit, double-crystal monochromator. 50mg target sample powders were mixed with 300mg boron nitride. Then, they were pressed into pellets for the XAS test. Co K-edge spectra of UHEM and SPEX OAC were acquired in transmission mode utilizing gas ionization chambers as detectors. X-ray Absorption Near Edge Structure (XANES) and Extended X-ray Absorption Fine Structure (EXAFS) data were extracted with established methods. The normalized EXAFS was converted from energy to *k*-space. These data were then Fourier transformed to *R*-space.

4.3 Material Characterization and Electrochemical Properties of 50 wt.%GeO_2-50 wt.% $Sn_{30}Co_{30}C_{40}$

Fig. 4-1 shows SEM images of the GeO_2 composite anode material. It can be seen that the particles do not have uniform geometric shape from nanoparticles to micron size particles, and homogeneous particle size distribution. The as-milled sample has 50% cumulative particles below 10.2 μm. The BET surface area is 4.725 m^2/g, approximately. The photon at high magnification shows that tiny particles can be as small as hundreds of nanometers. The overall particles of ball-milled samples consist of agglomerated nanoscale primary particles shown in Fig. 4-1 (left). This morphology is common for the ball milled powder because of the existence of dead zones in the milling jar. Some big

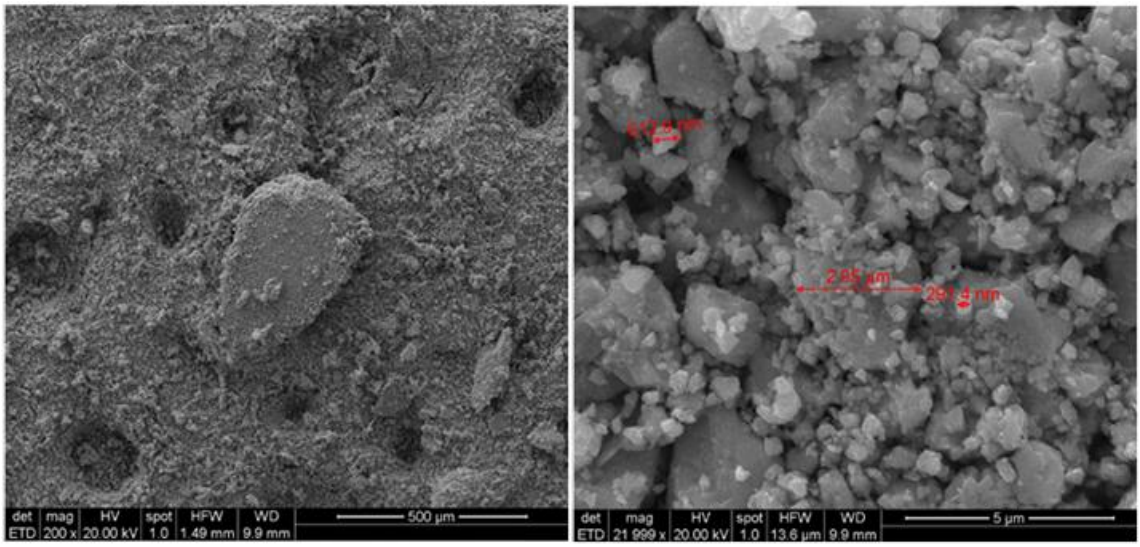

Fig. 4-1 SEM images of the composite samples GeO_2 composite (200x), left, GeO_2 composite (20,000x), right

particles stack in dead zones as to be not grounded intensively.

In order to identify crystalline structure, the X-ray diffraction pattern of milled GeO_2 composite is given in Fig. 4-2. The reference of Co_3Ge_2 peaks is provided in the inset. The pattern of GeO_2 composite shows three sensible bragg peaks and a very broad peak. The peaks can be identified as the (1 0 1), (1 0 2), and (1 1 0) planes of hexagonal Co_3Ge_2 alloy. A very broad hump can be observed at low angle in the XRD pattern, which is attributed to an amorphous phase. The Co_3Ge_2 is a high-temperature phase. An interesting feature related to mechanical alloying is the possibility of producing phases that usually require extreme conditions, like high temperatures or pressures to be formed, at room temperature and pressure. Although the MA technique is relatively simple, the physical mechanisms involved are not yet fully understood. No diffraction peaks from GeO_2 and Sn, Co or Sn-Co alloys were observed. They might be as an amorphous or nanostructure state after milling. XRD is not inadequate to characterize nanostructured material or material with short-range order. Further characterizations will be described below.

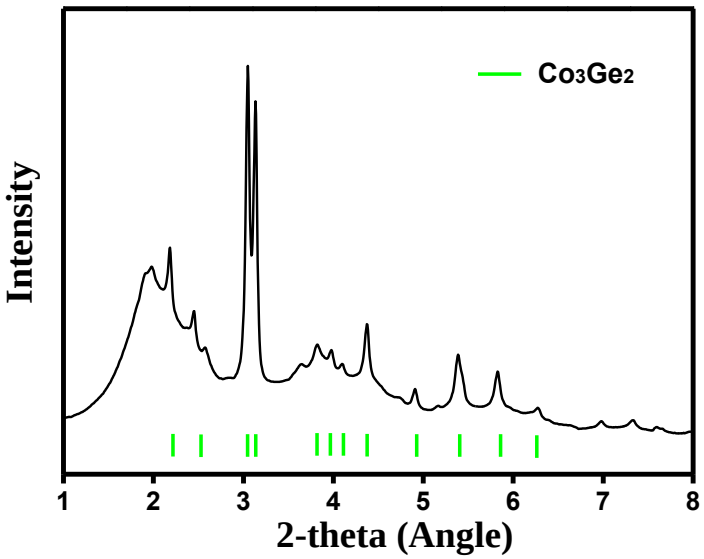

Fig. 4-2 X-ray diffraction (XRD) pattern of the GeO_2 composite material

Because of the low X-ray scattering, X-ray diffraction is not suitable to characterize nano or amorphous materials. Hence, the room temperature Ge K-edge, Sn K-edge, and Co K-edge X-ray absorption spectroscopy (XAS) experiments were performed at sector 20 bending magnet beamline at the Advanced Photon Source (APS). For a referencing purpose, the spectra for Ge, Sn, and Co were obtained in the condition. The results of X-ray absorption near edge spectra (XANES) provided the information of oxidation state and chemical state. Fig. 4-3a and 4-3b show that the oxidation states of Ge and Sn elements for the milled composite sample are higher than those of reference Ge and Sn. As shown in Fig. 4-3c, it is clear that the cobalt in the milled composite sample is present as largely metallic and possibly a nonoxidized cobalt compound. Together with the XRD result, the cobalt compound can be attributed to a Co_3Ge_2 intermetallic compound. The fine structure of the milled composite material was scrutinized by analyzing the EXAFS. Fig. 4-3d illustrates that the Ge has a large correlation (< 2 Å) lower than the Ge-Ge bond distance of Ge tape, corresponding to Ge-O bonds of GeO_2. Similarly, Sn K-edge EXAFS

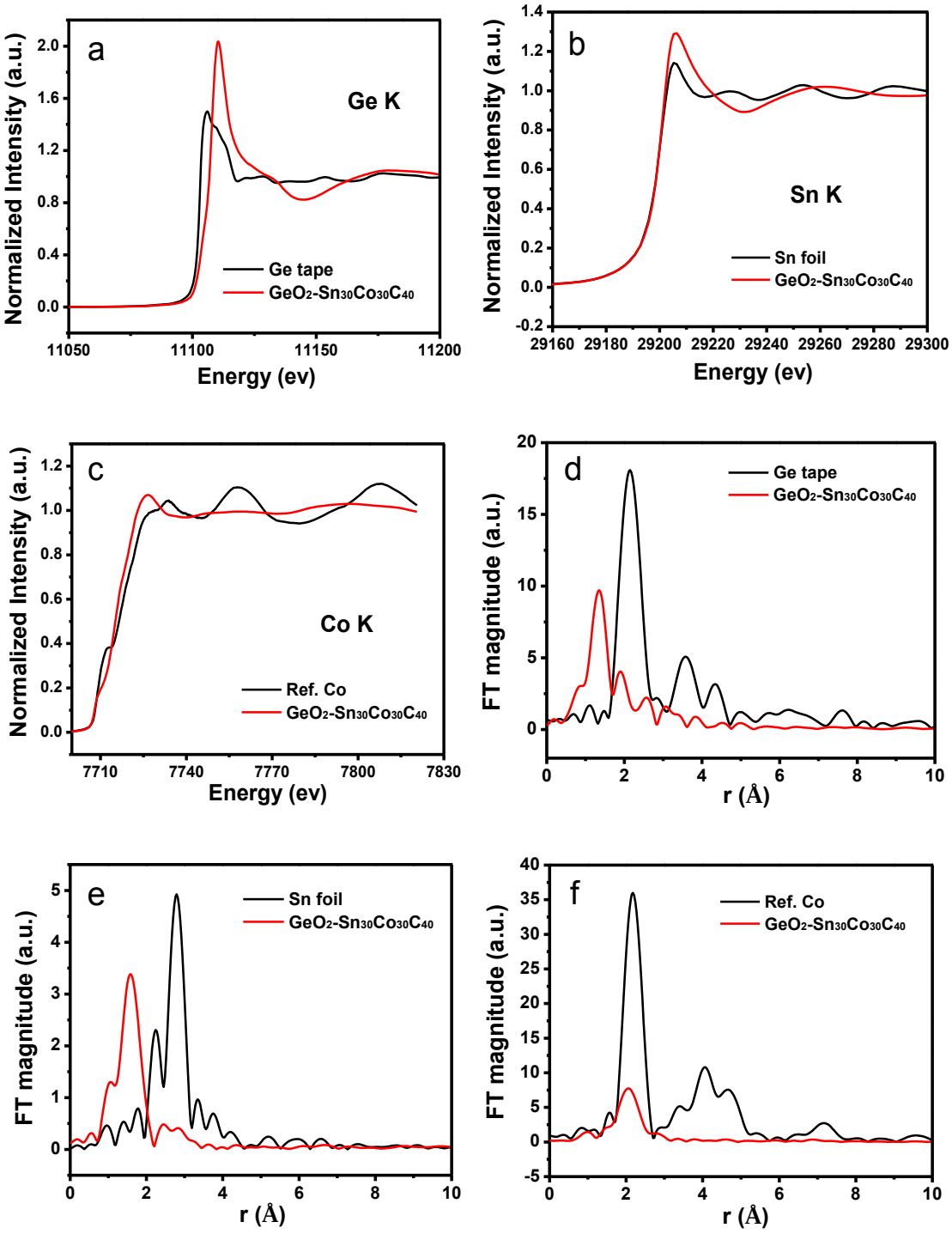

Fig. 4-3 The X-ray absorption spectra (XAS) of GeO_2-$Sn_{30}Co_{30}C_{40}$: (a) XANES of Ge K-edge, (b) XANES of Sn K-edge, (c) XANES of Co K-edge, (d) EXAFS of Ge K-edge, (e) EXAFS of Sn K-edge, (f) EXAFS of Co K-edge

spectra show a large amount of Sn-O correlation in Fig. 4-3e.

The milling process can produce a large amount of heat, which leads to many unpredictable reactions. GeO_2 probably loses oxygen and reacts with cobalt, and forms Co_3Ge_2 intermetallic compound, a high-temperature phase. Then, the lost oxygen bonds with Sn and forms SnO_2. From Fig. 4-3f, the spectra of Co K-edge EXAFS has a significant contribution from Co-Ge and Co-Co correlations as expected for the Ge-Co alloy identified in XRD. Obviously, XAS is a very helpful technology to provide us detailed information of local structure, which is invisible under XRD.

In order to trace the lithiation/de-lithiation pathway for the GeO_2 composite electrode, the high-energy XRD data were obtained in sector 11-ID-C of the Advanced Photon Source. Three samples were packed and sealed in polyimide tubes for XRD tests, which were taken from cells of fully discharged (discharge to 0.005 V), cycled (discharge to 0.005 V and charge to 2.5 V), and cycle-discharged (discharge to 0.005 V, charge to 2.5 V, and discharge to 0.005 V) states, respectively. As shown in Fig. 4-4, after discharge, Co_3Ge_2 peaks were still observed and the peak density had no noticeable change, which means that Co_3Ge_2 is almost electrochemical inactive.[31,32] Crystalline Co_3Sn_2 and Co_3Ge_2 share the same space group (*P63/mmc*) and atom sites. Co_3Ge_2 only has Ge instead of Co, and there are minute differences on atomic parameters. Fig. 4-5 illustrates the crystal structure of the Co_3Ge_2 crystal and Table 4-1 lists the structure information, accordingly. Fig. 4-6 lists bond distances of Co_3Ge_2. The reason that the capacity of Co_3Ge_2 is poor could be attributed to two aspects. Firstly, as common reported, Co is completely inactive for lithium. As shown in Fig. 4-5, there exist few diffusion tunnels for Li ion. Li can only react with accessible Ge atoms (at the surfaces of grains and/or

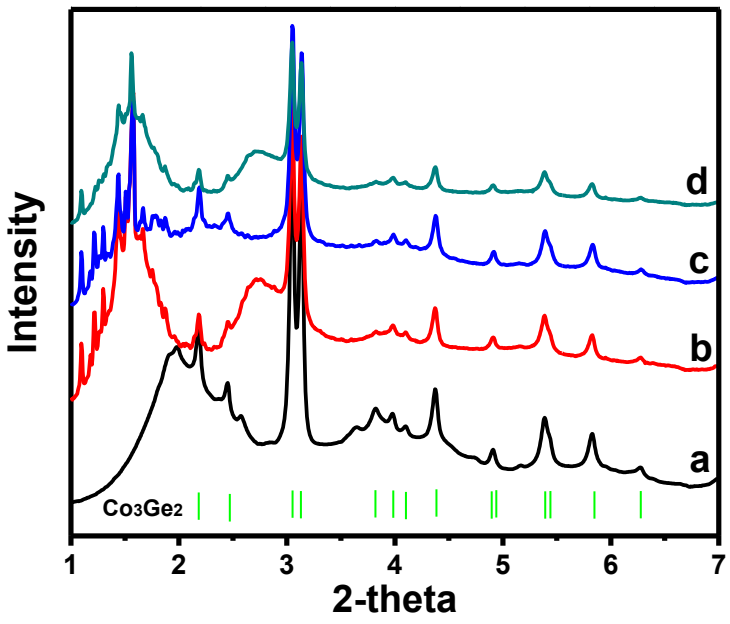

Fig. 4-4 X-ray diffraction (XRD) patterns of GeO_2 composite samples a) as-milled, b) discharged, c) cycled, and d) cycle-discharged

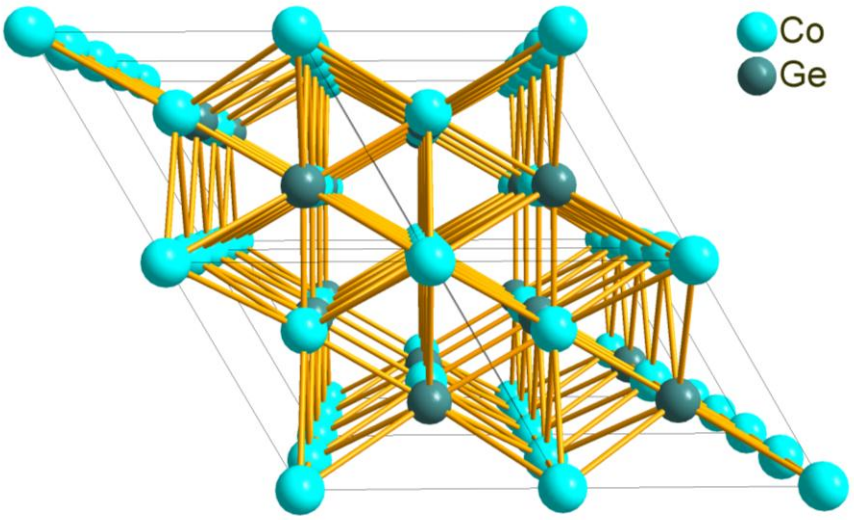

Fig. 4-5 Crystal structure of Co_3Ge_2

Table 4-1 Atomic parameters of Co_3Ge_2

Phase data		Atomic parameters					
Space-group	P 63/m m c (194) - hexagonal	**Atom**	**Wyck.**	**Site**	**x/a**	**y/b**	**z/c**
Cell	a=3.9640 Å	Co1	2a	-3m.	0	0	0
	c=4.9920 Å	Co2	2d	-6m2	1/3	2/3	3/4
	c/a=1.2593	Ge1	2c	-6m2	1/3	2/3	1/4
	V=67.93 $Å^3$						

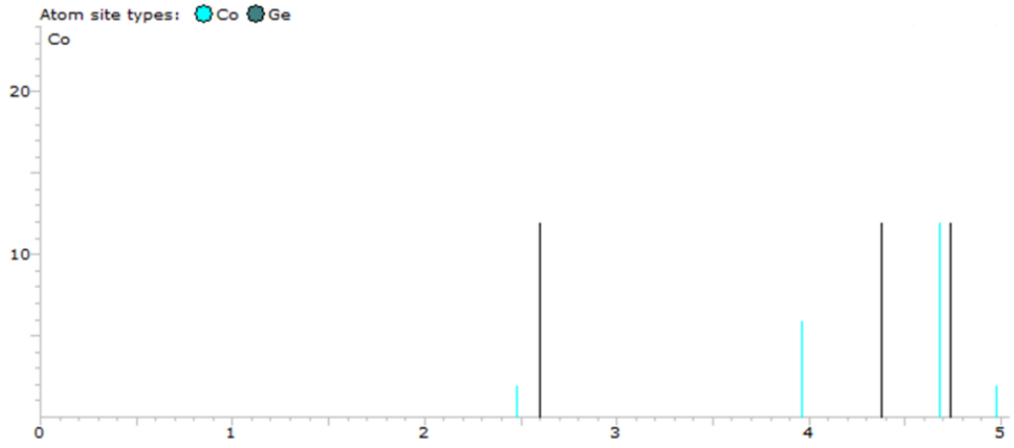

Fig. 4-6 Bond distances of Co_3Ge_2 (range: 1-5 Å)

particles) in materials. Active Ge atoms are trapped by so many Co atoms that these form an impenetrable cover on the surface, preventing further reaction. Secondly, according to many studies,[31-33] nanoparticles and/or grain size could increase the capacity greatly, which makes more active material like Ge exposed to Li ion. If particle size reduction is caused by cycling, then perhaps this is why the capacity of Co_3Sn_2 cells increase with cycle number. In our case, Co_3Ge_2, apparently, exists in the form of crystalline but not a nano or amorphous state. A set of new peaks appeared at very low angle after discharge, which might be ascribed to some macromolecular crystals from electrolyte depositing on

the surface of the electrode which formed during electrochemical reaction. Also, two humps were found at 1.5^{o} and 2.7^{o} 2-theta angle, which might be associated with nanoparticles or amorphous phases of oxides. That is going to be discussed below. The pattern of the cycled sample looks very close to that for the discharged one except for the hump at 2.7^{o} 2-theta angle, which implies that corresponding a nano or amorphous phase decomposed after delithiation. That broad peak was observed again in the diffraction pattern of the cycle-discharged sample, which means the electrochemical reaction had been stable.

The EXAFS is used to determine the distances, coordination number, and species of the neighbor of the absorbing atom. Due to its inherently element-unique property, a pair distribution function (PDF) experiment was carried out at 11-ID-C beamline in APS. PDF can give the probability of finding an atom at a given distance r from another atom and can be considered as a bond length distribution. Because it has no elemental limitation, it may provide different information compared with XAS. Fig. 4-7 exhibits the PDF patterns of GeO_2, SnO_2, as-milled GeO_2 composite, discharged, and cycled GeO_2 composite. Table 4-2 lists all the peaks corresponding to the interatomic distance of the various samples. By comparison, the 1st peak of the as-milled sample corresponds to Ge-O (1.74 Å) atomic distance of GeO_2, which demonstrates that there is still an amount of GeO_2 in the presence after milling. But the 2nd peak can be attributed to the Sn-O bond (2.05 Å) of SnO_2, which is consistent with the results of EXAFS. Fig. 4-6 shows the bond distances of Co_3Ge_2, (atom A is Co, atom B is Ge or Co). Obviously, the 3rd peak is ascribed as the Ge-Co (2.6 Å) atomic distance of Co_3Ge_2, which is also observed in the XRD pattern of GeO_2 composite. Similarly, the very broad 5th peak is mainly contributed

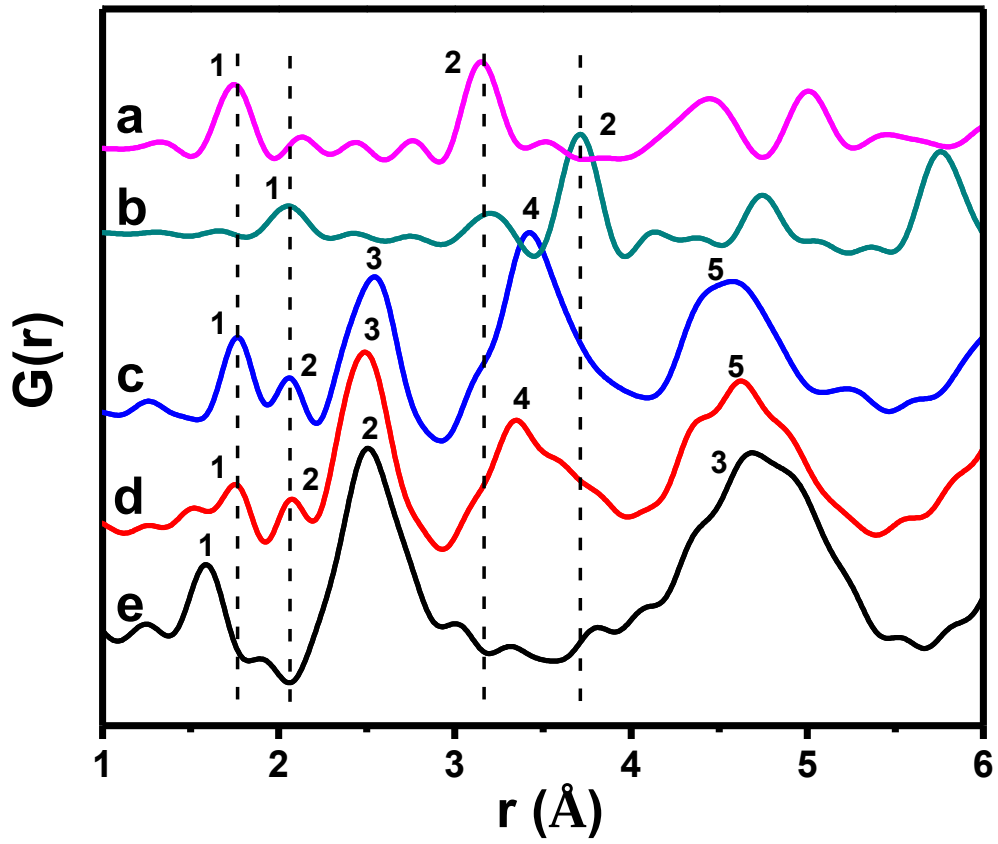

Fig. 4-7 Pair distribution function (PDF) patterns of the samples a) GeO_2, b) SnO_2, c) as-milled GeO_2 composite, d) cycled GeO_2 composite, and e) discharged GeO_2 composite

Table 4-2 The interatomic distance of the various samples*

Sample	Peak 1(Å)	Peak 2(Å)	Peak 3(Å)	Peak 4(Å)	Peak 5(Å)
GeO_2 (pristine)	Ge-O	Ge-Ge	Ge-Ge	-	-
	(1.74)	(3.152)	(4.5)		
SnO_2 (pristine)	Sn-O	Sn-Sn			
	(2.05)	(3.706)			
As-milled composite	1.74	2.05	2.6	3.42	4.57
Cycled composite	1.74	2.05	2.5	3.36	4.57
Discharged composite	1.59	2.5	4.57		

* All bond distance information in the table from ICSD database

from Co-Co, Co-Ge, and Ge-Ge atomic distances of Co_3Ge_2. The 4th peak is also very broad, which most likely is attributed to the interaction of GeO_2 and SnO_2. The pattern of the discharge sample shows three main peaks located at 1.59 Å, 2.5 Å, and 4.57 Å. The first peak cannot be identified. Analysis of the in-situ EXAFS data is currently underway, and expected to provide more detailed information on the change of this peak, which might be helpful to make it clear. The 2nd and 3rd peaks belong to Co_3Ge_2, which means that Co_3Ge_2 is electrochemically inactive. The bond distance peaks of GeO_2 and SnO_2 have vanished during the discharge process. The atomic distance peaks of GeO_2 and SnO_2 reappear at the 1.74 Å, 2.05 Å, and 3.36 Å shown in the pattern of the cycled sample, which means GeO_2 and SnO_2 can be reversible in this case. This phenomenon was also found by other researchers. P. Poizot and co-workers first reported transition-oxides (MO, where M is Co, Ni, Cu, or Fe) can be reversible during lithiation and delithiation.[34] They explained that decreasing particle size led to enhanced electrochemical activity towards the reversibility. C. H. Kim *et al.* synthesized $MGeO_3$ (M = Cu, Fe, and Co) by solid-state reaction with GeO_2, CuO, Fe_2O_3, and CoO.[35] They found that nano-sized metal particles indeed generated and catalyze the reversible reaction, such that the first coulombic efficiency is greatly improved compared to that for metal-absent GeO_2 electrodes, which is illustrated by X-ray absorption spectroscopy (XAS) experiments. Recently, Kim *et al*. published a report on the reversible reaction of GeO_2/Ge/C nanocomposite.[36] Germanium in this system plays a similar role as to that of the metallic copper, iron, or cobalt. In this work, Co_3Ge_2 might act as the catalyzer to trigger this reversible reaction. In this circumstance, the first cycle efficiency is also increased, accordingly.

Fig. 4-8 shows the discharge-charge profiles of the GeO_2 composite electrode at a constant current of 100 mA/g with the cut-off potentials of 0.005 and 2.5 V. It can be seen that GeO_2 has a flat plateau potential around 0.25~0.4 V. The voltage-capacity curve of the GeO_2 composite shows the slope style which is associated with Li^+ insertion in various stage and amorphous phase. The GeO_2 electrode delivered the discharge and charge capacities of 2209 mAh/g and 764 mAh/g in the first cycle, respectively. The first cycle capacity loss of GeO_2 is up to 65.4%. GeO_2 reacts with lithium during the initial cycle, forming Li_2O and metallic Ge, and causes poor coulombic efficiency and cycle performance. Oxides resulted in the formation of a lithium inactive Li_2O phase during the first charge (lithium insertion), leading to a decrease in coulombic efficiency. The mechanism of this lithiation reaction is described by an initial conversion reaction (equation 4.1) followed by an alloying reaction (equation 4.2).[12]

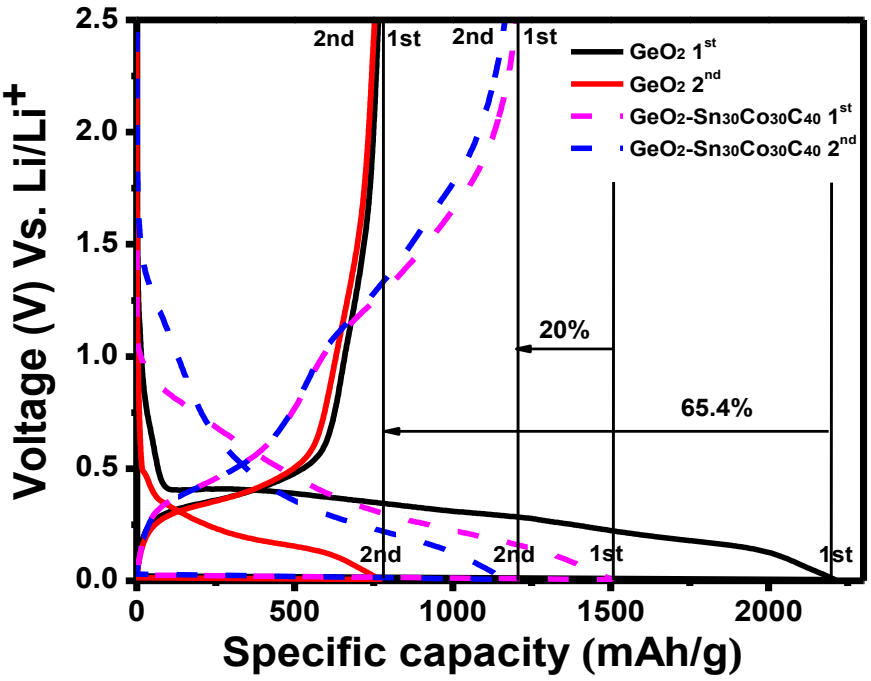

Fig. 4-8 Voltage profile of GeO_2 and GeO_2 composites

$$GeO_2 + 4Li \rightarrow Ge + 2Li_2O \quad (4.1)$$

$$Ge + 4.4Li \leftrightarrow Li_{4.4}Ge \quad (4.2)$$

However, GeO_2 composite shows the first cycle discharge-charge capacities of 1501 mAh/g and 1200 mAh/g with the first cycle efficiency of 80 %. Obviously, the composite electrode has a much higher coulombic efficiency. From the above PDF results, we already found the decomposition and reformation of Ge-O and Sn-O bonds during Li^+ release/uptake. This reversible conversion reaction plays an important role on the first cycle efficiency, which is the key point of significant improvement of Coulombic efficiency. One extra benefit of reversible conversion reaction is the increase of lithium storage. According to some calculations, if the Ge oxidation reaction happened, GeO_2 can store up to 8.4 Li^+, corresponding to a theoretical capacity of 2152 mAh/g, much higher than that of GeO_2.

Cycling performances of the samples (GeO_2 composite, GeO_2, and $Sn_{30}Co_{30}C_{40}$) were tested in a coin type half-cell shown in Fig. 4-9. A cut-off voltage window of 0.005-2.5 V was used for all the tests upon a constant current of 100 mA/g in the initial two cycles and 300 mA/g in subsequent cycles. GeO_2 composite exhibits significantly superior specific capacity compared with GeO_2 and $Sn_{30}Co_{30}C_{40}$. The GeO_2 electrode delivers high capacity over 2000 mAh/g initially, but suffers from a rapid degradation with a low Coulombic efficiency. The GeO_2 composite exhibits reversible capacity over 800 mAh/g in 100 cycles without negligible fading. Obviously, Sn-Co-C added can improve the capacity retention significantly. Tin-cobalt-carbon milled as a molar ratio of 30:30:40 is loaded into the same test program, which exhibits 380 mAh/g in 100 cycles. GeO_2 composite material makes a great progress in terms of combining capacity and lifespan.

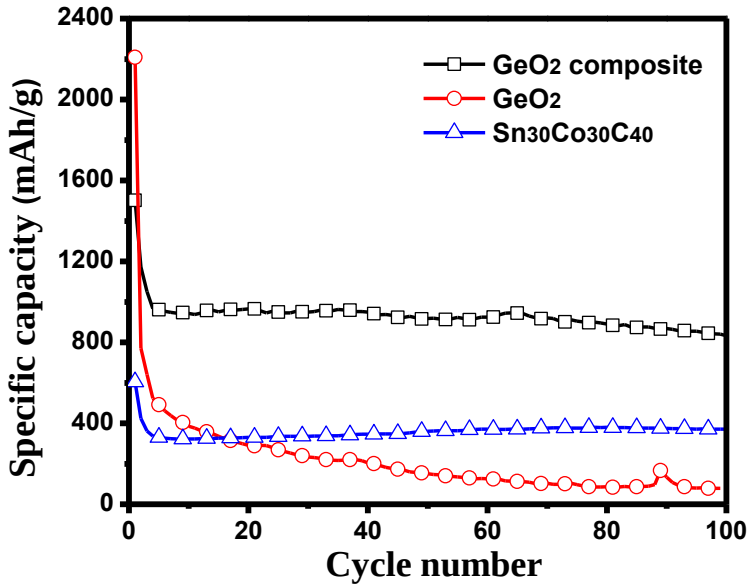

Fig. 4-9 Cycle performance of GeO_2 and GeO_2 composites

The rate capability of GeO_2 composite cycled between 0 and 2.5 V has also been investigated. It is a very important factor, especially for the applications in electric vehicles. As shown in Fig. 4-10, the cell was loaded on a stepwise rate from 50 mAh/g to 1200 mAh/g. Then, current was switched back to 100 mAh/g. The specific capacity of the GeO_2 composite electrode maintains 493 mAh/g under a high current density (1200 mA/g). It exhibits good recoverable performance after switching back to a low current density (100 mA/g).

4.4 Conclusion

In this work, the composite anode material of GeO_2-$Sn_{30}Co_{30}C_{40}$ showed good electrochemical properties of large reversible capacity, high coulombic efficiency, good rate capability, and long cycle life. In particular, the first cycle efficiency has remarkable improvement, compared with pure GeO_2. The X-ray diffraction reveals that high-temperature temperature phase Co_3Ge_2 was obtained during milling. The EXAFS data

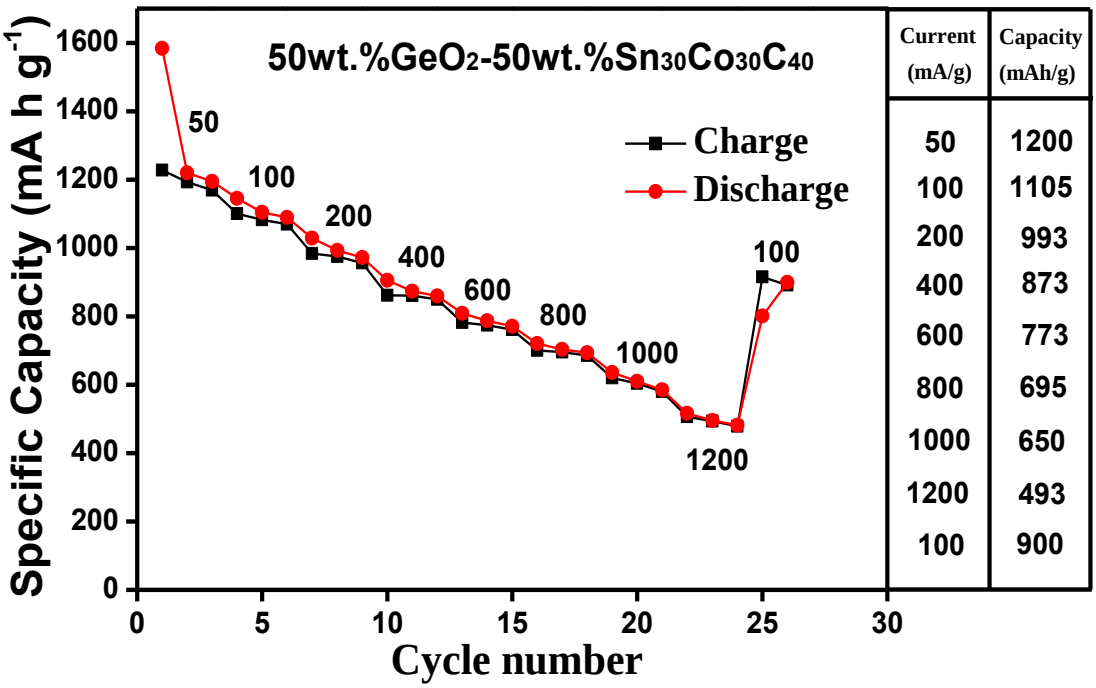

Fig. 4-10 Rate performance of GeO_2 composites

illustrated that GeO_2 and SnO_2 had existed after mechanical milling. The partial Ge-O bonds suffered from the breakage by external force and the released oxygen atoms reacted with Sn under high temperature during milling. The PDF technique pointed out the reversible conversion reaction of GeO_2 and SnO_2. The mechanism of reversible reactions might be attributed to the catalytic effect of Co_3Ge_2. In all, GeO_2- $n_{30}Co_{30}C_{40}$ composite material shows a promising practical use for lithium ion batteries.

4.5 Reference

[1] W. J. Lee, M. H. Park, Y. Wang, J. Y. Lee and J. Cho, *Chem. Commun.*, 2010, **46**, 622.

[2] H. Kim and J. Cho, *Chem. Mater.*, 2008, **20**, 1679.

[3] H. Kim and J. Cho, *J. Mater. Chem.*, 2008, **18**, 771.

[4] M. G. Kim and J. Cho, *Adv. Funct. Mater.*, 2009, **19**, 1497.

[5] M. S. Whittingham, *Dalton Trans.*, 2008, 5424.

[6] H. Li, Z. Wang, L. Chen and X. Huang, *Adv. Mater.*, 2009, **21**, 4593.

[7] K. Amezawa, N. Yamamoto, Y. Tomii and Y. Ito, *J. Electrochem. Soc*., 1998, **145**, 1986.

[8] B. Gao, S. Sinha, L. Fleming and O. Zhou, *Adv. Mater*., 2001, **13**, 816.

[9] B. Key, M. Morcrette, J. M. Tarascon and C. P. Grey, *J. Am. Chem. Soc*., 2011, **133**(3), 503–512.

[10] J. Graetz, C. C. Ahn, R. Yazami and B. Fultz, *J. Electrochem. Soc*., 2004, **151**, A698-A702.

[11] C. S. Fuller and J. C. Severiens, *Phys. Rev*. 1954, **96**, 21.

[12] J. K. Feng, M. O. Lai and L. Lu, *Electrochim. Acta*, 2012, **62**, 103−108.

[13] D. J. Xue, S. Xin, Y. Yan, K. Ch. Jiang, Y. X. Yin, Y. G. Guo and L. J. Wan, *J. Am. Chem. Soc*. 2012, **134**, 2512−2515.

[14] N. G. Rudawski, B. L. Darby, B. R. Yates, K. S. Jones, R. G. Elliman and A. A. Volinsky, *Appl. Phys. Lett*., 2012, **100**, 083111.

[15] M. H. Seo, M. Park, K. T. Lee, K. Kim, J. Y. Kim and J. Cho, *Energy Environ. Sci.*, 2011, **4**, 425–428.

[16] C. K. Chan, X. F. Zhang and Y. Cui, *Nano Lett*., 2008, **8**(1), 306-309.

[17] A. M. Chockla, K. C. Klavetter, C. B. Mullins and B. A. Korgel, *Appl. Mater. Interfaces*, 2012, **4**, 4658−4664.

[18] X. L. Wang, W. Q. Han, H. Y. Chen, J. M. Bai, T. A. Tyson, X. Q. Yu, X. J. Wang and X. Q. Yang, *J. Am. Chem.Soc*., 2011, **133**, 20692−20695.

[19] K. H. Seng, M. H. Park, Z. P. Guo, H. K. Liu and J. Cho, *Nano Lett*., 2013, **13**, 1230−1236.

[20] http://www.sony.net/SonyInfo/News/Press/200502/05-006E/

[21] A. D. W. Todd, R. E. Mar and J. R. Dahn, *J. Electrochem. Soc*., 2006, **153**(10), A1998-A2005.

[22] A. D. W. Todd, R. E. Mar and J. R. Dahn, *J. Elecrochem. Soc*., 2007, **154**(6), A596-A604.

[23] P. P. Ferguson, A. D. W. Todd and J. R. Dahn, *Electrochem. Commun*., 2008, **10**, 25–31.

[24] P. P. Ferguson, R. A. Dunlap and J. R. Dahn, *J. Electrochem. Soc*., 2010, **157**(3),

A325-A332.

[25] A. D. W. Todd, R. A. Dunlap and J. R. Dahn, *J. Alloys and Compounds*, 2007, **443**, 114–120.

[26] P. P. Ferguson, M. L. Martine, R. A. Dunlap and J. R. Dahn, *Electrochim. Acta*, 2009, **54**, 4534–4539.

[27] P. P. Ferguson, P. Liao, R. A. Dunlap and J. R. Dahn, *J. Electrochem. Soc*., 2009, **156**(1), A13-A17.

[28] R. B. Lewis, A. Timmons, R. E. Mar and J. R. Dahn, *J. Electrochem. Soc*., 2007, **154**(3), A213-A216.

[29] J. Yang, M. Winter and J. O. Besenhard, *Solid State Ionics*, 1996, **90**, 281-287.

[30] C. Syryanarayana, *Prog. Mater. Sci*., 2001, **46**, 1-184.

[31] J. Xie, X. B. Zhao, G. S. Cao and J. P. Tu, *J. Power Sources*, 2007, **164**, 386.

[32] J. R. Dahn, R. E. Mar and A. Abouzeid, *J. Electrochem. Soc*., 2006, **153**, A361.

[33] V. V. Kharton, *Handbook of Solid State Electrochemistry*, Volume 2, Wiley-VCH Verlag GmBH & Co. KGaA (2011).

[34] P. Poizot, S. Laruelle, S. Grugeon, L. Dupont and J. M. Tarascon, *Nature*, 2000, **407**, 496.

[35] C. H. Kim, Y. S. Jung, K. T. Lee, J. H. Ku and S. M. Oh, *Electrochim. Acta*, 2009, **54**(18), 4371−4377.

[36] K. H. Seng, M. H. Park, Z. P. Guo, H. K. Liu and J. Cho, *Nano Lett*. 2013, **13**, 1230−1236.

CHAPTER 5

SILICON MONOXIDE/TIN-COBALT-CARBON COMPOSITE

5.1 Introduction

Lithium-ion batteries (LIBs) are considered the most promising candidate as the power source for portable electronic devices and electric vehicles. Especially for plug-in hybrid and all electric vehicles, LIBs will undoubtedly play a more important role in the future because of their advantages with regard to petroleum consumption and environmental protection. These applications necessitate the development of batteries with very high energy density. Accordingly, much effort has been devoted to the development of high-capacity electrode materials. Three types of anode material have been developed to date: Li metal, carbonaceous materials, and alloy/oxide. Lithium metal was the initial candidate as the anode material for LIBs. Unfortunately, dendrite forms on the Li electrode surface and affects battery durability and intrinsic safety. The carbon anode has been scaled up by industry for use in vehicle LIBs. Recently, Nissan and Chevrolet, almost at the same time, announced their new models of the electric and plug-in hybrid vehicles, the Leaf and Volt, respectively, which both employ carbon as the anode. However, carbonaceous material is limited by its theoretical capacity, and it is therefore not being pursued as a new-generation LIB anode.

In 1997, Idota and co-workers of Fuji Photo Film reported that they had synthesized a tin-based amorphous oxide anode (specific capacity, >600 mAh/g) as a substitute for the

carbon anode (specific capacity, 372 mAh/g).[1] The amorphous tin oxide composite provided theoretical volumetric and gravimetric capacity improvements over carbon of four and two times, respectively. After that, other researchers investigated alternative oxides, including SiO_x, MoO_3, SnO_2, and Co_3O_4.[2–5] Among them, SiO is of considerable interest owing to its high theoretical specific capacity (>1400 mAh/g). The amorphous SiO is thought to consist of nanoparticles of metallic silicon distributed in a matrix of SiO_2, which has a SiO_2 glass-like structure.[6] The SiO_2 structure is believed to dampen the deformational stress resulting from the lithiation process (Si → Li_xSi), thus restraining the pulverization of the active material. It has been known for a long time that Si can provide a specific discharge capacity of 3580 mAh/g.[7] However, the cycle life is problematic due to its huge volume expansion, over 300%.[8] To overcome this shortcoming, researchers have studied various alternative materials, which include pure silicon nanoscale powder, silicon nanowires, silicon thin films, silicon alloys (Si-M, where M = Sn, Ag, Zn, Mg, V, etc.), and silicon dispersed in an inactive/active matrix (Si/C, Si/graphene, SiO_x, SiO/C, etc.).[9–16] With regard to the latter, pristine SiO shows better cycle performance than pure micrometer-size silicon powder because of its composite structure. However, its cycle performance is not good enough to meet the needs of transportation applications.

In 2005, SONY introduced a new lithium-ion battery, NEXELION, employing an amorphous ternary Sn−Co−C composite as the anode material.[17] Recently, they successfully updated their NEXELION technology by increasing its capacity from 2.2 A h to 3.5 A h with the 18650 WH1 cell. The success of NEXELION demonstrated that Sn−Co−C alloy is a promising replacement for carbonaceous materials in the next-

generation anode. Dahn's group developed an extensive infrastructure for combinatorial and thorough studies of nanostructured Sn−Co−C alloys.[18−25] They produced various compositions of $Sn_xCo_yC_z$ by using magnetron sputtering and mechanical milling methods. They also completed electrochemical studies of $Sn_{1-x}Co$ ($0 < x < 0.6$) and $[Sn_{0.55}Co_{0.45}]_{1-y}C_y$ ($0 < y < 0.5$) prepared by magnetron sputtering. The best electrochemical performance was attained by the composition near $Sn_{30}Co_{30}C_{40}$. Subsequently, they compared the performance between mechanically alloyed and sputtered Sn−Co−C composites. Although both are characteristic of amorphous like or nanostructured materials, the sputtered material showed a reversible specific capacity over 600 mAh/g close to the theoretical capacity, while the ball-milled material had a specific capacity of 450 mAh/g. Even though sputtering is a better technique to synthesize nano level particles and more uniform material as opposed to mechanical alloying, it is not suitable for producing Sn−Co−C alloys for industrial scale because of the high cost of the electrical power required.

Silicon monoxide can produce high capacity but suffers from poor cycle life. Sn−Co−C has good cycleability and high tap density, but its reversible capacity is not significantly better than that of the commercial carbon anode. Our work reports a new anode material based on 50 wt % SiO-50 wt % $Sn_{30}Co_{30}C_{40}$ composite (molecular composition: $SiSn_{0.23}Co_{0.23}C_{0.3}O$), synthesized by the custom-made ultra high-energy ball milling (UHEM) method depicted in Fig. 5-1. The SiO−$Sn_xCo_yC_z$ composite has the potential to combine the advantageous properties of both Sn-Co-C (long cycle life) and SiO (high capacity) and, thereby, improve the overall electrochemical performance.

Mechanical ball milling, which is known to produce nanosized particles, is often used

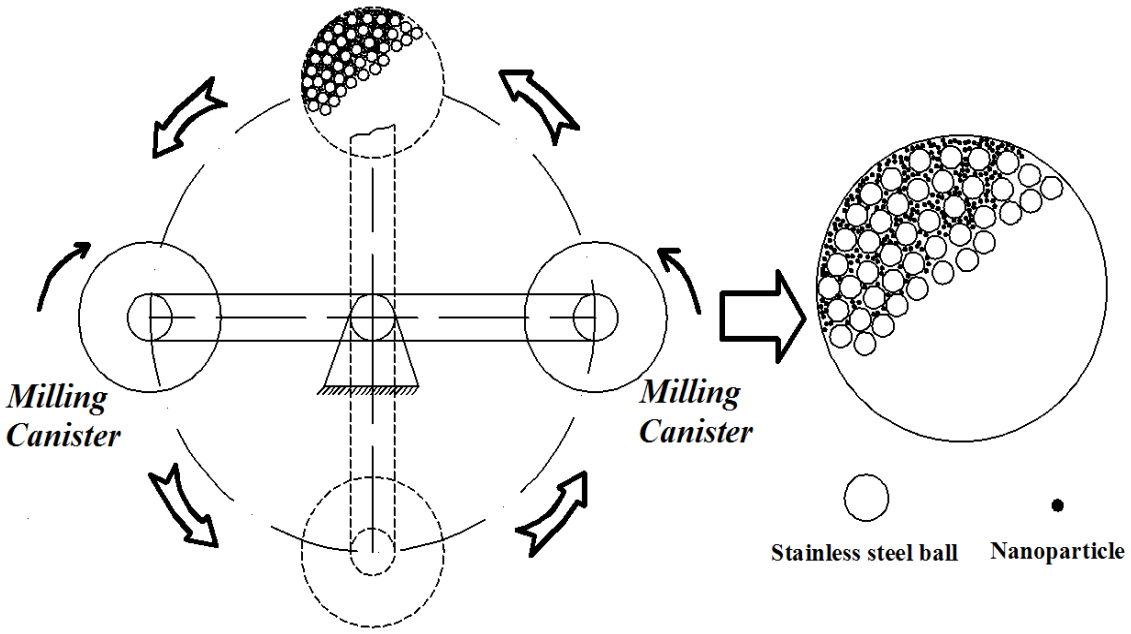

Fig. 5-1 Scheme for ultra high-energy ball milling machine

for improving electrochemical properties.[26] The ball milling method is employed not only to reduce the particle size but also to synthesize nonequilibrium alloys starting from blended elemental or pre-alloyed powders.[27] Traditional ball mills adopt stirred mills or vibration mills. However, these mills exhibit a limitation regarding product fineness: a size limit of 1 μm is often observed after several hours of grinding. This limitation is due to the particles being weakly confined in the breakage zone of these mills. Our custom-made milling machine works by a planetary mill method that creates a very high centrifugal field, confining the particles in the milling area and reducing the "dead zone" effect.[28−30]

In this work, X-ray absorption spectroscopy (XAS) and pair distribution function (*PDF*) are used to analyze local structural changes after UHEM and SPEX ball milling. The results reveal a tremendous difference between UHEM and SPEX samples and indicate the formation of Si_xSn_{1-x} alloys after milling. Si_xSn_{1-x} alloy was reported to be prepared

in an ultra high-vacuum chamber by simultaneous condensation on cold substrates (77 K) of evaporated silicon and tin.[31] When the concentration *x* of Sn is lower than 0.5, the alloys are observed to be amorphous. Some techniques such as rapid solidification, mechanical alloying, and vapor deposition are employed to synthesize nonequilibrium material (Fig. 5-2). Vapor deposition has very large departure from equilibrium (G_1-G_0, see Fig. 5-2). Mechanical alloying allows the material to be prepared much farther from equilibrium than rapid solidification.[32] So far, no article has reported Si_xSn_{1-x} amorphous alloy synthesized by mechanical alloying.

We also made a more detailed study on SiO-$Sn_{30}Co_{30}C_{40}$ anode material, including the electrochemical screening and charge-discharge reaction mechanism and structure characterization. We undertook X-ray diffraction (XRD) and pair distribution function (*PDF*) studies and electrochemical testing of xSiO • (1-x)$Sn_{30}Co_{30}C_{40}$ (x=0, 0.1, 0.3, 0.5, 0.7, 0.9, and 1) composite anode materials prepared by SPEX milling. Mechanical alloying is an effective and low-cost way to synthesize nanoscale and amorphous materials. Earlier, Whittingham and co-workers studied crystalline and amorphous Sn-Co

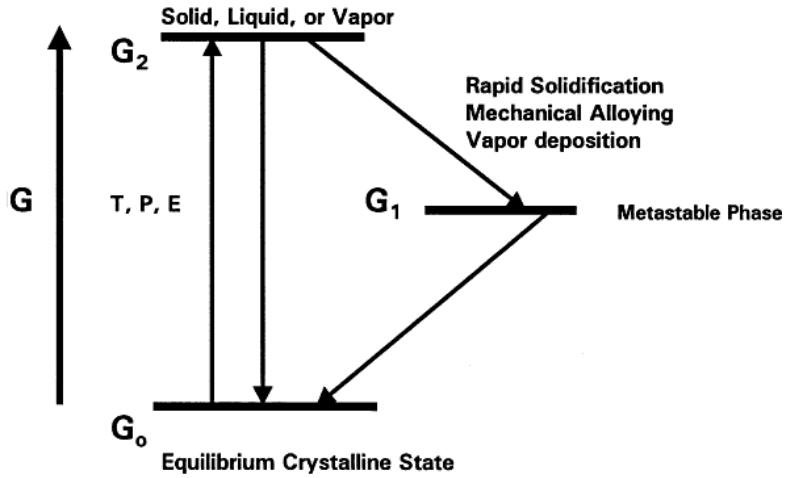

Fig. 5-2 The basic concept to synthesize nonequilibrium materials[32]

alloys and characterized them using the *PDF* method.[23,24] They concluded that nanosized amorphous tin–cobalt materials show enhanced cycling behavior over the crystalline SnCo analog and over crystalline tin. The focus of our work is on better understanding the variation of the reversible capacity of these samples with composition. According to our work, the composition of 50 wt.% SiO-50 wt.% $Sn_{30}Co_{30}C_{40}$ exhibits the best electrochemical performance in terms of cycle life and capacity. For detailed XRD and *PDF* study, we selected several cut-off voltages in the discharge-charge profile where major reactions occur. We employed the XRD and *PDF* techniques because they are powerful tools that simulate in-situ study and provide information about the long- and short-range order within the microstructure, respectively, at different voltages. They thus offer the possibility of gaining a deep understanding on the relationship between electrochemical properties and the material structure.

5.2 Experimental Procedure

5.2.1 Preparation of SiO-$Sn_xCo_yC_z$ Composites

The raw materials for this work, Silicon monoxide (99.99%, −325 mesh, Sigma-Aldrich), Tin (99%, powder, Sigma-Aldrich), Cobalt (99.5%, −325 mesh, Alfa Aesar), and Graphite (SMG-NAL1-10C, Hitachi), were purchased commercially. Two batches of these powders were blended overnight using a mixing machine with a weight ratio of 50 wt % SiO/50 wt % $Sn_xCo_yC_z$ (x, y, z molar ratio of 30:30:40) to obtain a homogeneous dispersion. Two mill apparatuses characterized by different mechanical energy intensity were used. Running a custom-made UHEM machine for 12 hours, we milled around 150 g of the mixture powder with 800 g of 1/4 in.-diameter stainless steel balls. For comparison, the same composition was milled with a SPEX milling machine (8000D

Mixer/Mill) for 24 hours. Hereafter, this oxide alloy composite will be abbreviated as OAC. For the *PDF* study, 50 wt % Si/50 wt % Sn and 50 wt % SiO/50 wt % Sn were milled with the SPEX machine for 24 hours. For more understanding about electrochemical reaction and structural changes during milling and lithiation/delithiation, a series of xSiO • (1-x)$Sn_{30}Co_{30}C_{40}$ (x=0, 0.1, 0.3, 0.5, 0.7, 0.9, and 1) composite anode materials were prepared by SPEX milling under the same condition above. All the material handling was carried out in a glove box filled with purified Argon.

5.2.2 Electrochemical and Physical Characterization

The OAC anodes were assembled in a CR 2032-type coin cell configuration. The OAC electrode laminate was prepared as a thin film by doctor-blade deposition (150 μm) on a copper substrate of a slurry composed of 80 wt.% active material, 10 wt.% acetylene black as the conductive agent, and 10 wt % U-Varnish polyimide binder. The laminate was heated at 300 °C in an Argon-flow oven for 2 hours to vaporize the solvent (Nmethyl-2-pyrrolidone) and accelerate the imidization reaction. The microstructure of the laminate had almost no change after annealing. The loading density of the active material was around 2.5 mg/cm^2. The electrode area was 1.6 cm^2. Lithium foil served as the counter electrode, and the electrolyte consisted of a 3:7 weight ratio of ethylene carbonate and ethyl methyl carbonate, with 1.2 M $LiPF_6$. The cells were assembled in an Argon-filled glove box and tested to cutoff potentials of 0.005 and 1.5 V. The cells were charged and discharged at various rates (C/9, C/3, and 1C). For testing high-temperature performance, the cells were placed in a 55 °C oven and cycled at the C/3 and 1C rates. Charge−discharge profiles and cycle performance data were collected with a Maccor battery cycler (Maccor, Inc., Tulsa). Solid lithium metallic powder (SLMP) technology

was employed in order to increase the first cycle efficiency for application. A half-cell configuration with SLMP was set up for electrochemical testing. SLMP is a technology developed by FMC Corporation that can effectively compensate the irreversible capacity and increase the energy density. The amount of lithium powder for coating was calculated according to the first cycle capacity loss of the OAC electrode. Then, SLMP was dispersed in solvent (p-xylene) and built up to a homogeneous suspension and then coated on the electrode surface. The process was completely handled in the Argon-filled glove box. Furthermore, the full-cell configuration was tested to exhibit the feasibility of using $Li_{1.2}Ni_{0.2}Mn_{0.6}O_2$ as the cathode and OAC as the anode with SLMP coating. For ex-situ XRD and *PDF* measurements, cells were cycled between 0.005 and 1.5 V under 50 mA/g. In order to detect the phase transformation during the charge-discharge process, the cell were discharged or charged to key cutoff potentials. When a select potential cutoff was reached, the cells were held on open circuit. Then, the cells were disassembled in the Argon-filled glove box. The active material was scratched off and packed in a polyimide tube for characterization. We employed this ex-situ method to simulate in-situ measurement and avoid the inevitable interference from the Cu current collector.

The particle size distributions of the UHEM and SPEX samples were determined by a Cilas 1090 particle size analyzer (PSA), with a measurement range of 0.04−500 μm. The specific surface area was tested on a NOVA 2200e instrument and calculated by the Brunauer−Emmett−Teller (BET) method. Raman spectroscopy was carried out for graphite measurement. Raman measurement was performed with a Renishaw inVia microscope spectrometer at ambient temperature. A HeNe (633 nm) laser was used, and the spectrum was signal averaged over 10 scans. The powder (500 mg) was evacuated at

220 °C for 2 hours prior to nitrogen adsorption. The morphology of the as-milled OAC was visualized via a Hitachi S4700 scanning electron microscope (SEM). Energy-dispersive X-ray spectroscopy (EDX) mapping was used to determine the elemental distribution of Si, O, Co, C, and Sn. Conventional lab X-ray diffraction data were collected on a Bruker D8 advance X-ray diffractometer, using a Cu−Kα radiation source (λ =1.5406 Å). The samples were scanned from 20° to 80° at a scan rate of 0.05° per minute.

XAS experiments were carried out at beamline 20-BM-B of the Advanced Photon Source (APS) at the Argonne National Laboratory. The incident beam was monochromatized using a Si (111) fixed-exit, double-crystal monochromator. Target sample powders (50 mg) were mixed with boron nitride (300 mg). Then, they were pressed into pellets for XAS test. Co K-edge spectra of UHEM and SPEX OAC were acquired in transmission mode using gas ionization chambers as detectors. X-ray absorption near edge structure (XANES) and extended X-ray absorption fine structure (EXAFS) data were extracted with established methods. The normalized EXAFS data were converted from energy to k-space. These data were then Fourier transformed to R-space.

Ex-situ experimental powder diffraction and *PDF* data were collected from the 11-ID-C beamline at the APS. The X-ray wavelength was preset to 0.10798 Å (fixed wavelength for this beamline). Use of a high-energy X-ray beam is important for obtaining excellent penetration to detect structural changes and for collecting diffraction data at high wave vectors. The high flux of the X-ray beam at APS is able to carry out fast experiments at one spectrum per minute. The samples were loaded in a cylindrical

geometry glass capillary (d = 0.5 mm). The detector was set up at different distances to the samples for diffraction and *PDF*. For the *PDF* test, 30 spectra were collected to reduce the error at high angle. The final *PDF* value is the average of 30 spectra.

Neutron *PDF* measurements were carried out at the Nanoscale Ordered Materials Diffractometer (NOMAD) at the Spallation Neutron Source (SNS), Oak Ridge National Laboratory. About 0.5 g powder of each sample was loaded into a vanadium sample can, with data acquisition time of 1 hour. The neutron scattering intensities were collected by multiple detector banks and rebinned to give a time-of-flight (TOF) spectrum for each sample. The spectrum from an empty vanadium can was collected and subtracted from the data of the sample with a vanadium can. All data treatment and conversion to the final *PDF* were performed using the software package developed for the NOMAD instrument.

5.3 Material Characterization and Electrochemical Properties of 50 wt.%SiO-50 wt.%$Sn_{30}Co_{30}C_{40}$

Table 5-1 summarizes the surface area and particle size of the UHEM and SPEX sample. It can be seen that 50% cumulative particle size of UHEM is less than 2.5 μm, and the SPEX-milled sample has 50% cumulative particles below 13μm. The BET surface areas are 7.521 m^2/g for the UHEM sample and 4.733 m^2/g for the SPEX sample. The larger surface area of the UHEM sample is in agreement with particle size distributions. Due to the tiny particle size of UHEM sample, the tap density, accordingly,

Table 5-1 The surface area and particle size and tap density of UHEM and SPEX-milled samples

OAC	Surface area (m^2/g)	Particle size
UHEM	7.521	50% particle size < ~2.5μm
SPEX	4.733	50% particle size < ~13 μm

decreases compared with the SPEX-milled sample. The different particle sizes obtained by the two milling methods can result in significantly different electrochemical properties. As we know, nanoscale material can introduce improved active material reactions as the lithium ion diffusion paths can be shortened. Furthermore, nanomaterial can decrease the solid-electrolyte interface (SEI) resistance and lead to higher specific capacities at high charge/discharge rates.

Fig. 5-3 shows SEM images of the OAC after UHEM. It can be seen that the particles do not have uniform geometric shape, and homogeneous particle size distribution. This morphology is common for the ball-milled powder because of dead zones in the milling jar. Most particle sizes range from nanometer to 10 μm. Although agglomeration does occur, the nanosize of the single particle is maintained. The SPEX sample has similar morphology to the UHEM sample. EDX mapping images for Si, O, Sn, Co, and C are taken with a UHEM sample (OAC). The results indicate that Si (Fig. 5-3e) and Sn (Fig. 5-3f) exhibit very similar distribution, especially in the yellow-circled areas. Large particles or agglomerates of cobalt can be seen in Fig. 5-3c (blue-circled areas), which is consistent with the XRD results (Fig. 5-4).

In the XRD patterns for the OAC materials prepared by UHEM and SPEX milling (Fig. 5-4), Bragg peaks from tin and graphite are not observed. Graphite readily loses its crystalline structure under external stress. This may account for graphite being invisible in the XRD pattern. According to the Raman spectrum, the carbon is graphitic. Two Raman scattering peaks at 1578 and 1340 cm^{-1} are assigned as G and D bands, respectively. These peaks are due to intrinsic phenyl ring stretching (G band) and the disordered band (D) in graphite. Dahn and co-workers have synthesized a Sn−Co−C thin

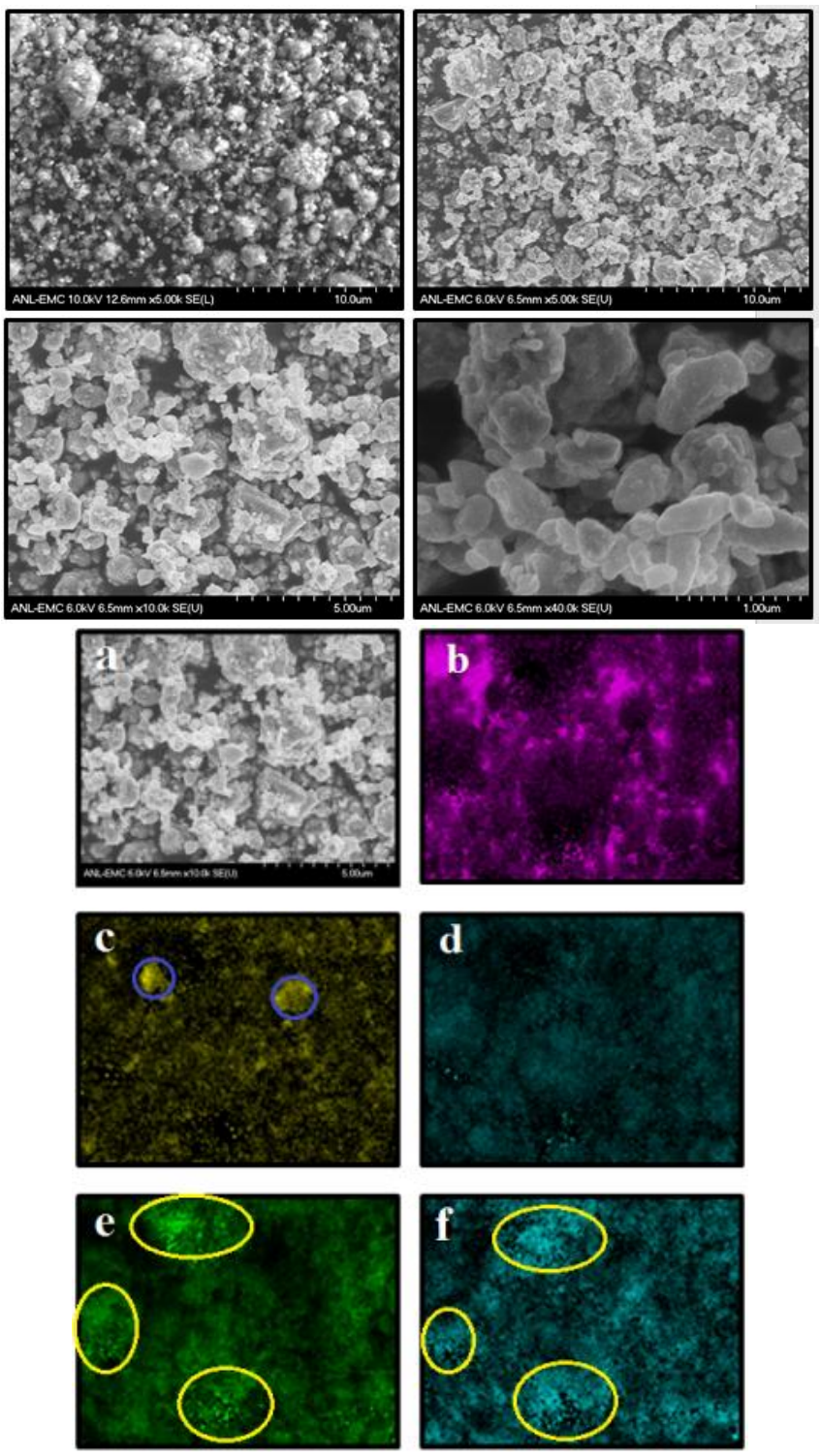

Fig. 5-3 SEM images of UHEM sample at different resolutions and EDX elemental mapping of (b) C, (c) Co, (d) O, (e) Si, and (f) Sn for the UHEM SiO-$Sn_{30}Co_{30}C_{40}$ composite. Scale bar in micrograph: 5.00 μm

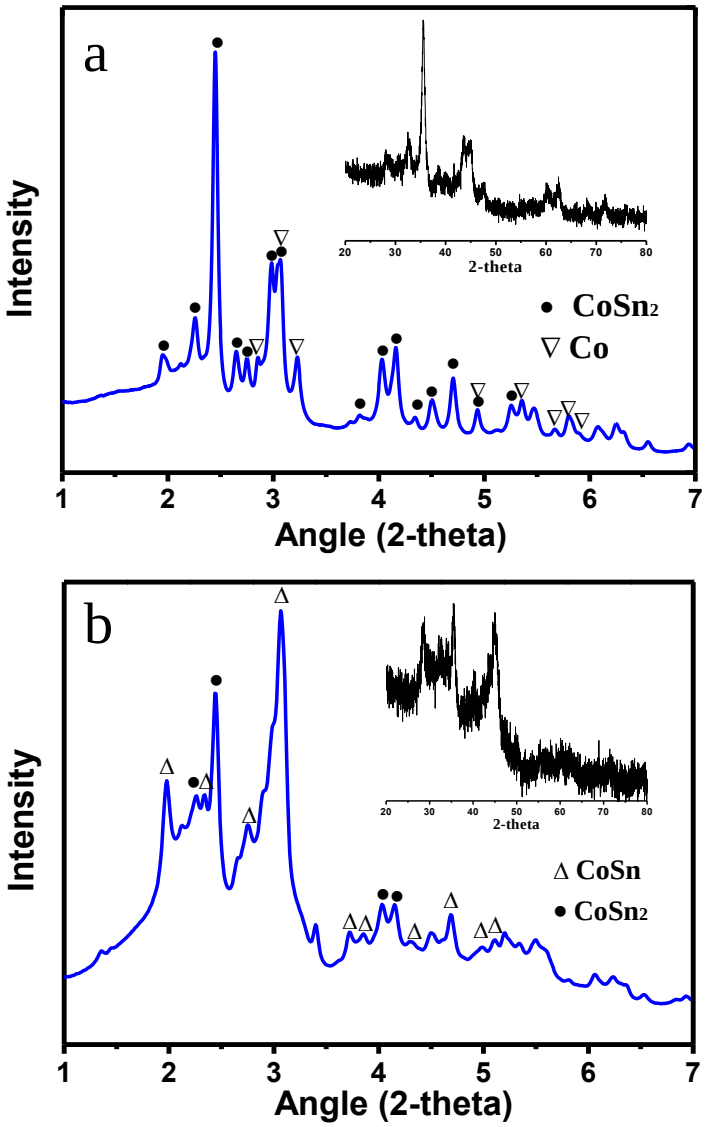

Fig. 5-4 XRD patterns of (a) UHEM sample and (b) SPEX-milled sample

film by using sputtering, which showed grains of amorphous Co−Sn separated by a carbon matrix.[22] Transmission electron microscopy by the Whittingham group on a commercial Sony hybrid lithium-ion battery with an amorphous tin−cobalt anode showed the presence of nanometer-sized CoSn grains.[33] Therefore, the carbon may play a buffer role in restraining the volume expansion and limiting capacity. An in-situ study by Dahn and co-workers demonstrated that the insertion of lithium in nanostructured $Sn_{30}Co_{30}C_{40}$

proceeds via the following reaction, where only the fully charged (left) and fully discharged (right) states are indicated,

[132 (1–*z*) + 40 *y*] Li+ $Sn_{30}Co_{30}C_{40}$ ↔ (1–*z*) (6 $Li_{22}Sn_5$ + 30 Co) + *z* CoSn + 40 Li_yC,

where $y = 0.5$.[21] Oxide peaks are not detectable in Fig. 5-4, which implies that milling occurred without oxidation. The inset images are conventional lab XRD patterns. Due to the amorphization of the as-milled samples, the lab XRD apparatus is limited by low energy and low resolution to index peaks. Therefore, high-energy XRD was carried out. Diffraction peaks for $CoSn_2$ and Co are clearly present in the XRD pattern for the UHEM sample (Fig. 5-4a). Commercial SiO is known to be an amorphous phase. The structure of SiO consists of nanoparticles of Si distributed in a matrix of amorphous SiO_2. Nagao and co-workers[6] found that amorphous SiO is composed of silica-like glass and metallic silicon cluster based on a comparison between the radial distribution functions [*RDF*(r)] of SiO and SiO_2. A very broad hump can be observed at low 2θ in the XRD pattern of the UHEM sample (from 1 to 3.3°), which is attributed to an amorphous phase.

By comparison, the XRD pattern of the SPEX-milled sample presents completely different phases of the material prepared by UHEM (Fig. 5-4b). The main phases after SPEX milling are CoSn and $CoSn_2$. The lithium intercalation process for Co−Sn alloys ($CoSn_2$, Co_3Sn_2, and CoSn) was reported earlier.[34] Cobalt serves as “matrix glue” that holds the structure and restrains the pulverization. Therefore, $CoSn_2$ exhibits a larger capacity but poorer cycleability, whereas CoSn presents the better cycle performance but has lower capacity.

Room-temperature Co K-edge transmission X-ray absorption studies were performed at the APS Sector 20 bending magnet beamline. Fig. 5-5a shows a comparison of the Co

XANES (near edge) of the milled samples with Co metal foil. It is clear that the cobalt in both the SPEX and UHEM samples is largely metallic, and no oxidized cobalt compound is present. Fig. 5-5b shows the EXAFS $\chi(k)$ function, and Fig. 5-5c, the corresponding Fourier transform. The EXAFS spectra of the UHEM and SPEX samples are different, indicating that the average Co atoms in these samples have distinctly different local environments. In particular, the EXAFS spectrum of the UHEM sample with Co foil clearly shows that ~40% of the Co atoms is present as metallic cobalt. This finding is consistent with the XRD spectra, which show distinct peaks corresponding to metallic Co. Additional contributions from other correlations are evident in the low-*k* signal, in agreement with the presence of other Co-containing compounds in the XRD of the UHEM sample. The spectra of the SPEX sample indicate a significant contribution from Co−Sn and Co−Co correlations, as expected for the Co−Sn alloys identified in XRD. Significant pure cobalt metal-like environments are not evident in the EXAFS spectra of the SPEX sample, consistent with the absence of distinct peaks in the XRD that can be indexed to Co metal. Analysis of the Co EXAFS data in conjunction with the EXAFS at the Sn edge is expected to provide detailed information on the local structure of the Co and Sn in the various samples and is underway.

Galvanostatic charge-discharge experiments with the OAC anode material are carried out at current rates of 100 mA/g, 300 mA/g, and 900 mA/g, respectively, within a voltage window of 0.005-1.5 V. In the first cycle, UHEM anode exhibits charge and discharge capacities of 1030 mAh/g and 1480 mAh/g at 300 mA/g current (~C/3). All the discharge capacity is delivered below 0.4 V. A small variation is observed in the voltage profile with continued cycling at 300 mA/g and 900 mA/g (Fig. 5-6), indicating excellent

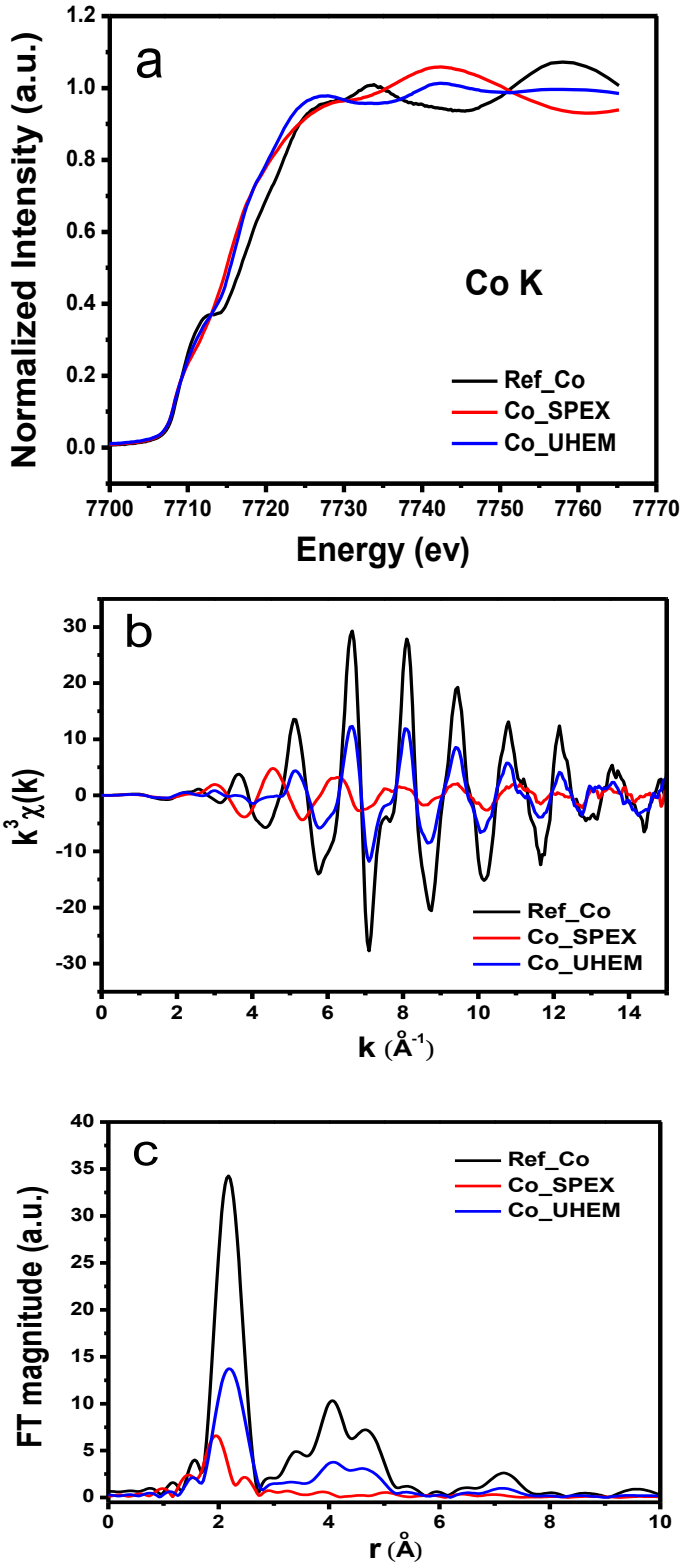

Fig. 5-5 X-ray absorption studies of milled composite samples (a) Co K-edge XANES showing. (b) EXAFS χ(k) function of UHEM and SPEX OAC (c) Magnitude of the Fourier transformed Co K-edge data for UHEM and SPEX OAC

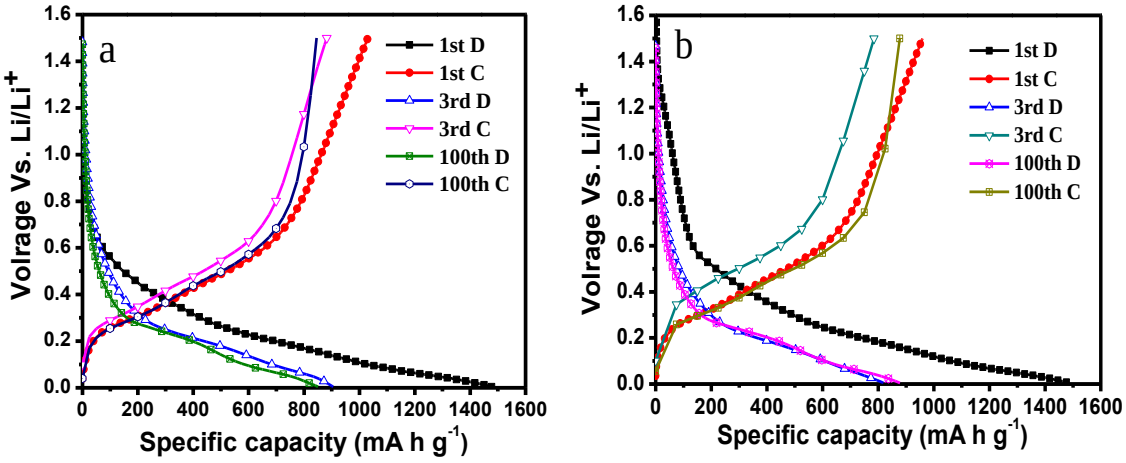

Fig. 5-6 Charge-discharge curves of cells with UHEM anode cycled at rates of (a) 300 mA/g (~C/3) and (b) 900 mA/g (~1C)

capacity retention.

Fig. 5-7a shows the discharge/charge specific capacity versus cycle number for the OAC electrode, along with its Coulombic efficiency. The UHEM anode delivered a specific capacity of 900 mAh/g at the rate of 300 mA/g, much higher than that (~600 mAh/g) of the SPEX anode at the same current. Moreover, at low current of 100 mA/g (~C/9), the specific capacity of the UHEM anode increased to 1040 mAh/g. The first cycle efficiencies of the SPEX and UHEM anode are 78 and 69.6%, respectively, at 300 mA/g. The superior first cycle efficiency of the SPEX electrode may be explained by its different particle size, surface area, and morphology compared with the UHEM electrode. The greater capacity loss at the first cycle of the UHEM anode may be attributed to more Li^+ ions trapped in electrode particles and consumed on SEI formation. After the initial cycles, the Coulombic efficiency rapidly increases to near 100%, remaining stable thereafter, indicating that the formed passivating film on the electrode remained intact and allowed excellent reversible cycling. The main initial capacity loss is due to SiO (the first cycle efficiency: 50−55%). The $Sn_{30}Co_{30}C_{40}$ not only prolongs cycle life, but also

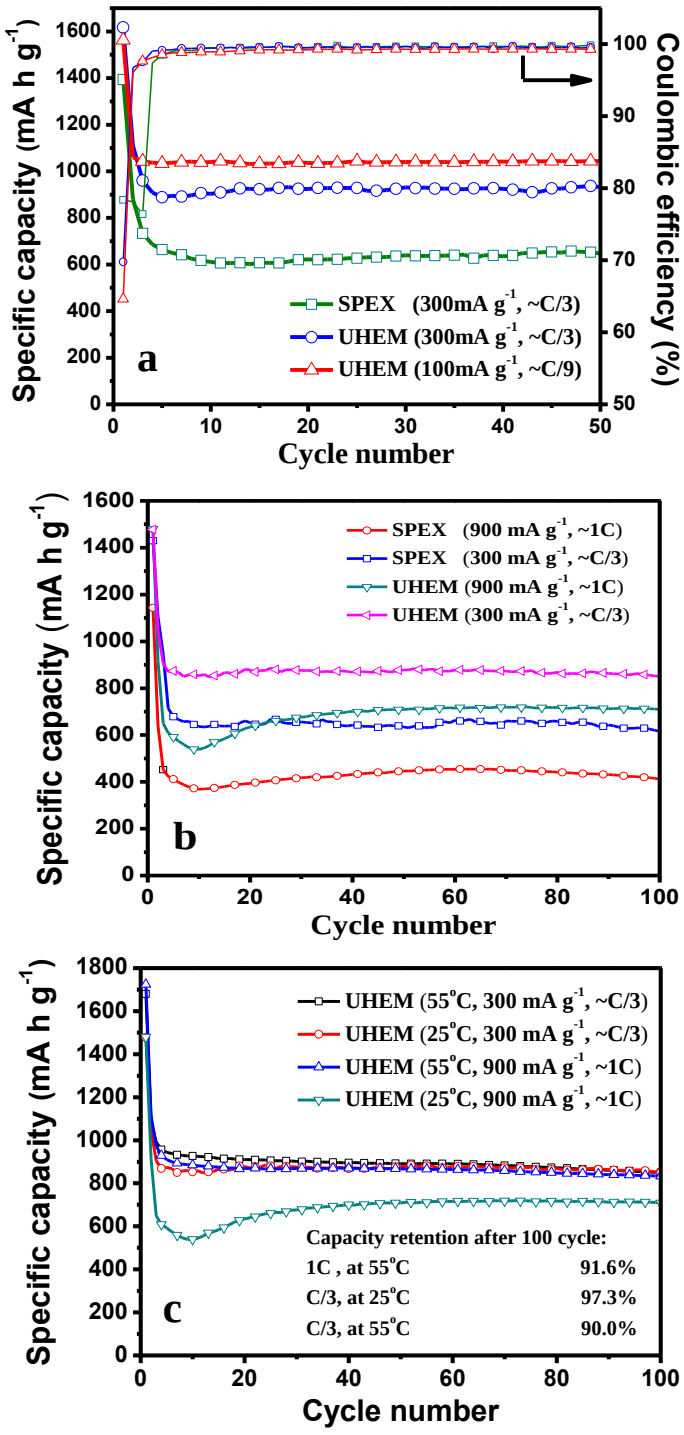

Fig. 5-7 Cycling performance of cells with (a) UHEM anode (current C/9 and C/3) and SPEX anode (current C/3), (b) UHEM anode (current C/3 and 1C) and SPEX anode (current C/3 and 1C), and (c) UHEM anode (current C/3 and 1C) at room temperature and 55°C

improves first cycle efficiency. To study the rate capability of the composite, the OAC anode fabricated by UHEM and SPEX methods was cycled at high current (900 mA/g, ~1C). As shown in Fig. 5-7b, the UHEM anode exhibits excellent rate capability: only 22% capacity loss and over 700 mAh/g specific capacity at current of 1C for 100 cycles. However, the capacity of the SPEX anode decreases from ~600 to ~400 mAh/g with 33% capacity loss at the high rate. For the first few cycles at high rate, the curves in Fig. 5-7b have a "concave" shape. We interpret this behavior as indicating that at the beginning, some particles are not involved with the lithiation reaction, especially the large particles present in the material even after ball milling. Lithium insertion pulverizes the large particles and forms a lithium-ion transport path. The capacity will discharge completely until all active materials contact and react with the electrolyte.

To study the thermal stability and high temperature performance of the UHEM OAC, we placed cells in an oven preset to 55 °C and operated at currents of 1C and C/3 for 100 cycles. Fig. 5-7c shows that, over the first 20 cycles, the specific capacity of the UHEM anode operated at C/3 and 55 °C was much higher compared with conditions of C/3 at 25 °C and 1C at 55 °C. The higher temperature could have speeded up the reaction kinetics, and the lower current could have provided more reaction time, which would promote a more thorough reaction and make the active material react more completely. Nevertheless, the accelerated reaction will inevitably lead to the rapid degradation of the composite material. As a result, after 100 cycles, the capacity retention was 97.3% for the anode cycled under conditions of 1C at 25 °C, but 91.6 and 90% for the anodes cycled under conditions of 1C at 55 °C and C/3 at 25 °C, respectively.

To increase the first cycle efficiency, SLMP was coated homogeneously on the OAC

electrode, and then coupled with Li metal. The Coulombic efficiency was 86% in the first cycle and increased to ~100% in the following cycles (Fig. 5-8a). To prove the applicability of the OAC anode material, we coupled it with the $Li_{1.2}Ni_{0.3}Mn_{0.6}O_{2.1}$ cathode developed by the Argonne National Laboratory. The cathode was composed of 84% active material, 8% conductive additive, and 8% binder solution. Fig. 5-8b shows the first cycle voltage profile of this full cell. The average voltage is around 3.5 V. The full cell achieves good cycle life without obvious degradation in 100 cycles at the C/9 rate, as shown in Fig. 5-8c.

Particle size is one of the key factors that contribute to the improvement of the specific capacity and the durability. However, it might not be the sole factor that resulted in such a large difference in the delivered capacity between UHEM OAC and SPEX OAC. Because our materials have amorphous or highly disordered phases, X-ray *PDF* analysis was employed to identify local structures that are correlated with specific electrochemical properties. Recently, *PDF* analysis has been successfully used to investigate short-range order in lithium-ion battery electrode materials.[35] The *PDF* technique considers total scattering (Bragg and diffuse scatterings) and converts it to real space by a Fourier transformation, while standard XRD patterns only contain information about the long-range average structure. The G(r) gives the probability of finding an atom at a given distance r from another atom and can be considered as a bond length distribution. Therefore, the *PDF* technique is a highly effective tool for characterizing those materials that do not possess the periodicity of a crystal structure. In this work, we performed a series of *PDF* experiments to study the local structure of OAC through observing and comparing the differences of milled samples.

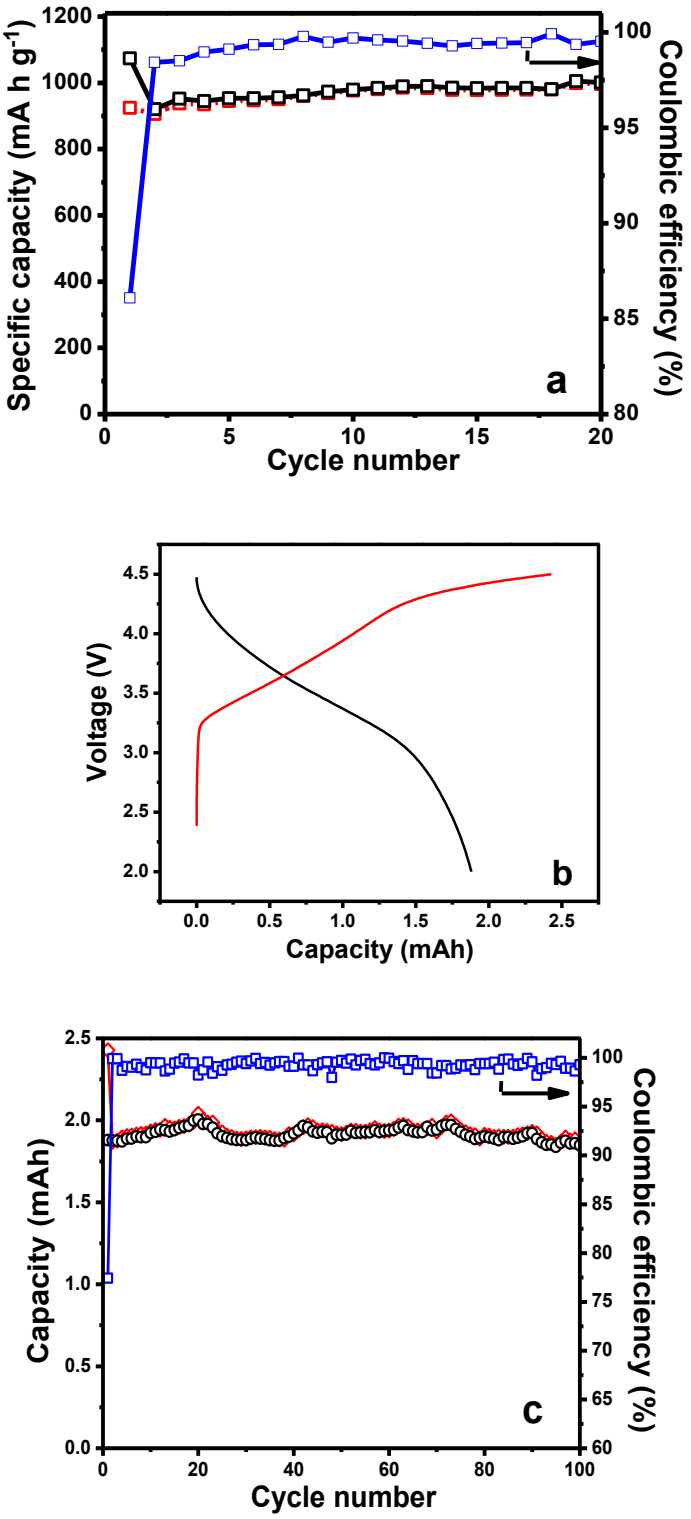

Fig. 5-8 Electrochemical performance of SLMP coated OAC electrodes: (a) UHEM OAC electrode vs. Li metal with SLMP coating, (b) the first cycle voltage profile of the $Li_{1.2}Ni_{0.3}Mn_{0.6}O_{2.1}$ vs. UHEM OAC with SLMP coating, (c) the cycle performance of $Li_{1.2}Ni_{0.3}Mn_{0.6}O_{2.1}$ vs. UHEM OAC with SLMP coating

Fig. 5-9a shows the *PDF* profiles for SiO, milled $Sn_{30}Co_{30}C_{40}$, SPEX OAC, and UHEM OAC. The interatomic distance peaks of SiO appear at 1.61, 2.35, and 3.05 Å, which correspond to the Si−O bonds of SiO_2 (alpha-quartz, *P3221*), the Si−Si bonds of Si ($Fd\bar{3}m$) nanoparticles, and the Si−Si bonds of SiO_2 (alpha-quartz, *P3221*), respectively. It was earlier reported that the structure of SiO consists of nanoparticles of Si dispersed in a matrix of amorphous SiO_2 (silicon dioxide), which was proven by *PDF* results.[36] The red line is the SPEX-milled $Sn_{30}Co_{30}C_{40}$ *PDF* curve. The peaks at 2.64, 3.73, and 4.65 Å are all attributed to the Co−Sn alloys. The blue line and olive line are the *PDF* curves of SPEX OAC and UHEM OAC, respectively. We compared the *PDF* results for SiO, milled $Sn_{30}Co_{30}C_{40}$, and milled OAC in order to determine whether some new phases were formed after ball milling. A new peak can be seen at the 3.42 Å interatomic distance (marked with red circle) in both the SPEX OAC and UHEM OAC *PDF* curves. This finding demonstrates that milled OAC is not only a physically simple mixture of SiO and $Sn_{30}Co_{30}C_{40}$, but some chemical reactions happened during the milling process between them. We also found that the 2.35 Å peak (marked with black circle) diminished almost completely for the UHEM OAC, indicating that most Si−Si bonds were destroyed by the impact among the stainless steel balls during the ball milling. Compared with SPEX milling, UHEM offers substantially higher attrition energy. Yet, clearly, the Si−Si bond remains, as seen by the 2.35 Å peak in the *PDF* curve for SPEX OAC, but the intensity has been significantly reduced. The intensity of the Si−Si peak at 2.35 Å decreases simultaneously with the emergence of the 3.42 Å peak. Therefore, the 3.42 Å peak is more likely associated with Si. In auxiliary experiments, Si/Sn (1:1 weight ratio) and SiO/Sn (1:1 weight ratio) materials were prepared by SPEX milling for 24 hours, which

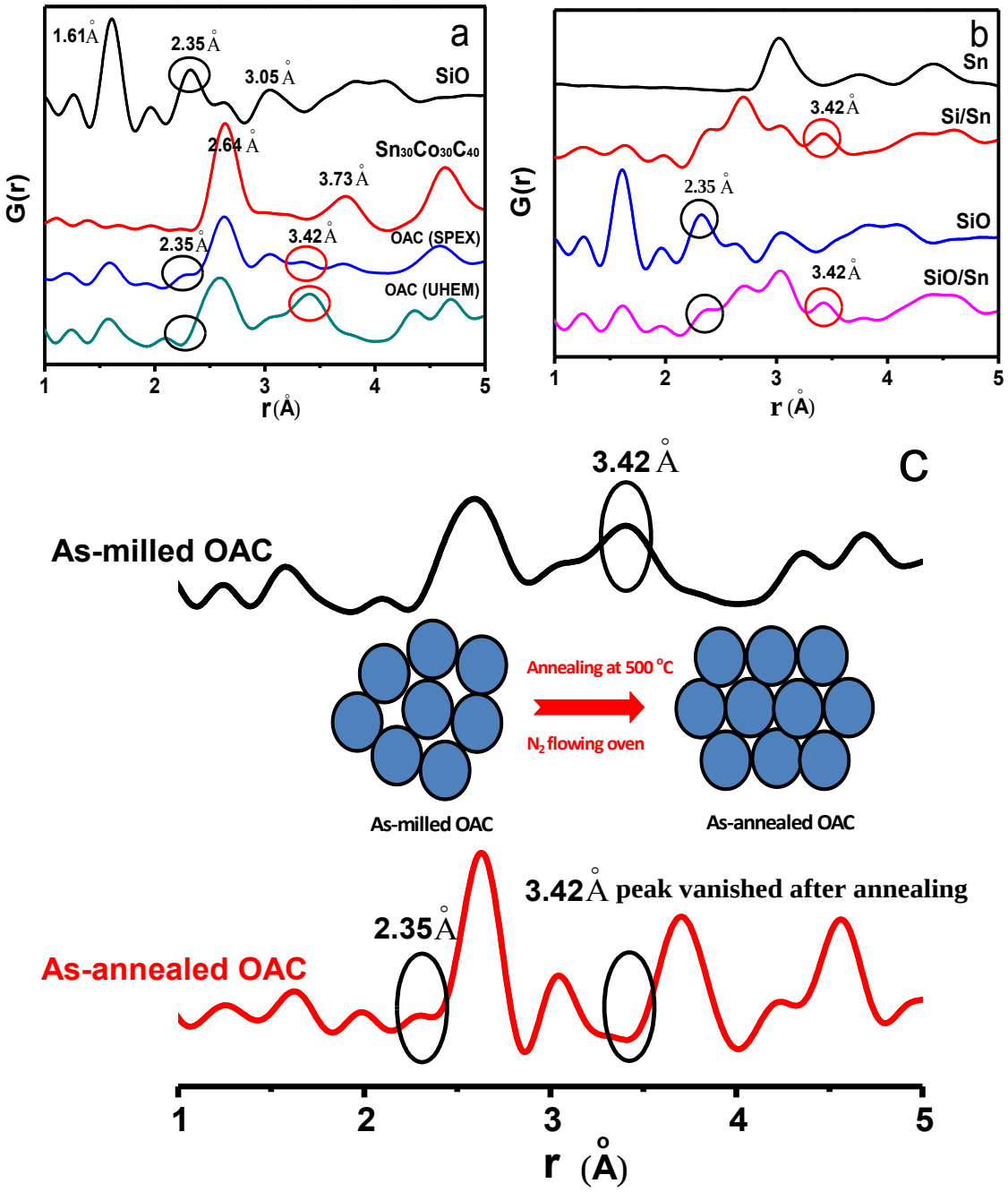

Fig. 5-9 Pair distribution function profile of (a) SiO, milled-$Sn_{30}Co_{30}C_{40}$, SPEX OAC, and UHEM OAC, (b) Sn, Si/Sn, SiO, and SiO/Sn, (c) annealed OAC

aimed at observing the 2.35 Å and 3.42 Å peaks and determining the difference. Fig. 5-9b shows *PDF* profiles of Sn, Si/Sn, SiO, and SiO/Sn. As was the case for OAC, the 3.42 Å peak is still present in milled Si/Sn and SiO/Sn. The auxiliary *PDF* experiments also indicated Si−Si bond breakage of the Si nanoparticles in SiO powder after ball milling with Sn powder. However, so far, it cannot be assured that the 3.42 Å peak can be attributed to an amorphous compound. Amorphous alloy is a kind of nonequilibrium metal, which tends to crystallize. The glass transition event is unique to amorphous alloys. Therefore, after annealing, we should observe the transition from the amorphous state to crystal structure. To test this conclusion, we annealed UHEM OAC powder in flowing N_2 at 500 °C for 3 hours, and then carried out *PDF* analysis. Fig. 5-9c shows that the 3.42 Å peak vanished after annealing, which means that the short-range order was lost. It further proves that the 3.42 Å peak belongs to amorphous alloy. Meanwhile, the peak at 2.35 Å, corresponding to the Si−Si bonds of Si ($Fd\bar{3}m$), emerged again. The second correlation of Si−Si is located at 3.84 Å, but unfortunately, it is overlapped by the peak (3.74 Å) of the Co−Sn correlation. The 3.42 Å peak is present in the *PDF* patterns for milled Si/Sn and SiO/Sn, which belong to neither the Si−Si correlation nor the Sn−Sn correlation. Furthermore, there is no intermetallic compound between Si and Sn. Hence, the 3.42 Å peak is speculated to be the Si−Sn correlation for Si−Sn amorphous alloy.

The *PDF* results were refined by *PDF*gui. The *PDF* curve for milled Si/Sn fitted to the data based on the tetragonal Sn, and the cubic Si did not show any peak at 3.42 Å. As-milled $Sn_{30}Co_{30}C_{40}$ experimental data were fitted using CoSn (space group P6/mmm and lattice parameters a = 5.278, c = 4.257), shown in Fig. 5-10a. The goodness-of-fit factor R_{wp} obtained is 31%. Obviously, the main phase of milled $Sn_{30}Co_{30}C_{40}$ is CoSn, which is

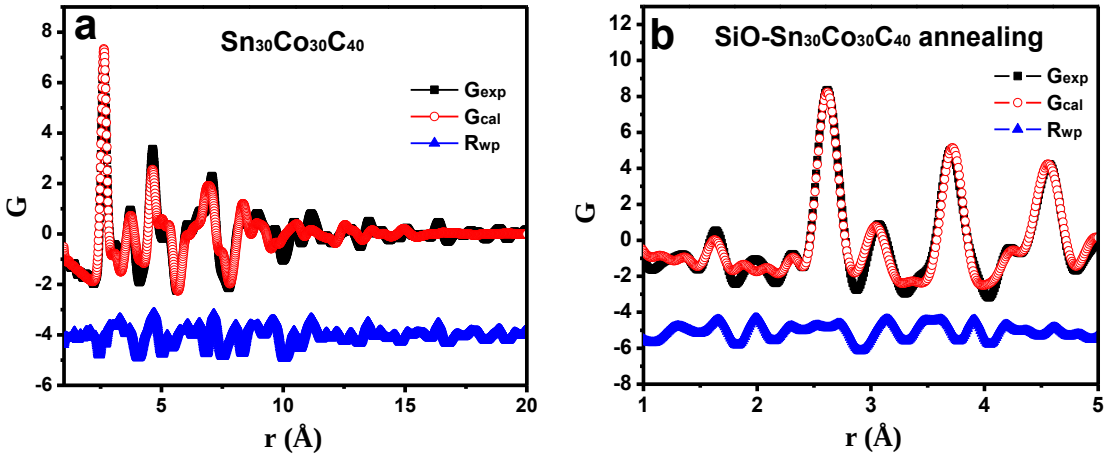

Fig. 5-10 *PDF* fitting data: (a) The *PDF*, G(r) of as-milled $Sn_{30}Co_{30}C_{40}$ and the calculated *PDF* plot and (b) The *PDF*, G(r) of annealed SiO-$Sn_{30}Co_{30}C_{40}$

consistent with the work of Fan *et al.*[33] The data demonstrate the formation of nano-hexagonal CoSn in a carbon matrix. As-milled SiO- $Sn_{30}Co_{30}C_{40}$ is difficult to fit to the data because we cannot find standard phases to match with the peak at 3.42 Å. For annealed SiO- $Sn_{30}Co_{30}C_{40}$, fitting of four phases (Si, Sn, CoSn, and SiO_2) was carried out. The fitting agreement factor R_{wp} is yielded to 17%, as shown in Fig. 10b. We believe that the great change of specific capacity between ultrahigh energy milling and conventional SPEX milling methods was most likely related to the difference in the material microstructure. The EXAFS results offer strong evidence that there is a large amount of Co metal unalloyed with Sn in the UHEM sample. Moreover, Sn and Co were added at a 1:1 molar ratio. Therefore, Sn should exist as a pristine state or alloy. Metallic Sn was not observed in the XRD and *PDF* patterns. After annealing at 500 °C, the Si−Si peak at 2.35 Å and the Sn−Sn peak at 3.04 Å appeared again.

Therefore, the formation of Si_xSn_{1-x} amorphous alloy is the most probable hypothesis. More detailed study will be done in future work. The macroscopic temperature of the milling vial is about 40−50 °C, which depends on milling time and sample media. The

instantaneous temperature inside can rise up to 300°C with the SPEX 8000 mixer/mill, and it can be even higher (>500 °C) with the planetary ball milling machine.[32] The high temperature may enhance the chemical reaction kinetics. Even though the silicon and tin are almost immiscible in the crystalline state, the Si−Sn amorphous alloy has been reported as a thin film in an ultra high-vacuum chamber by coevaporation.[31] The Si_xSn_{1-x} alloy could be amorphous in the concentration range $0 < x < 0.57$. Because of the small scattering vector, *RDF*(r) cannot be determined accurately by Fourier transformation. For high composition of tin ($0.57 < x$), the β−Sn structure was observed in the mixture.[37] More experiments and techniques will be employed to gain better understanding of the mechanism behind the electrochemical improvement of the UHEM OAC material.

5.4 Electrochemical Study and Structural Understanding of xSiO • (1-x) $Sn_{30}Co_{30}C_{40}$

Composite materials with the seven compositions shown in Table 5-2 were produced during the course of this work. The amount of SiO increases from sample #1 to #7. The structural properties of these compounds were investigated by high-energy XRD. The XRD patterns in Fig. 5-11 show that the peak intensities weaken with increasing amount of SiO, meaning that the crystallinity of the samples decreases and the milled samples become more amorphous. The XRD pattern of sample #7, pristine SiO, exhibits an extremely broad peak because the SiO consists of nanoparticles of metallic silicon distributed in a matrix of SiO_2.[10] Most Bragg peaks of the xSiO • (1-x)$Sn_{30}Co_{30}C_{40}$ samples (x=0, 0.1, 0.3, 0.5, 0.7, 0.9, and 1) are attributed to CoSn phase (hexagonal, *P6/mmm*). Obviously, CoSn phase is more prone to forming during milling. As the amount of SiO increased, the strongest peak (2 1 1) of crystal $CoSn_2$ (tetragonal, *I4/mcm*)

Table 5-2 Sample Information

Item number	Sample information
#1	$Sn_{30}Co_{30}C_{40}$
#2	10wt.%SiO-90wt.%$Sn_{30}Co_{30}C_{40}$
#3	30wt.%SiO-70wt.%$Sn_{30}Co_{30}C_{40}$
#4	50wt.%SiO-50wt.%$Sn_{30}Co_{30}C_{40}$
#5	70wt.%SiO-30wt.%$Sn_{30}Co_{30}C_{40}$
#6	90wt.%SiO-10wt.%$Sn_{30}Co_{30}C_{40}$
#7	SiO

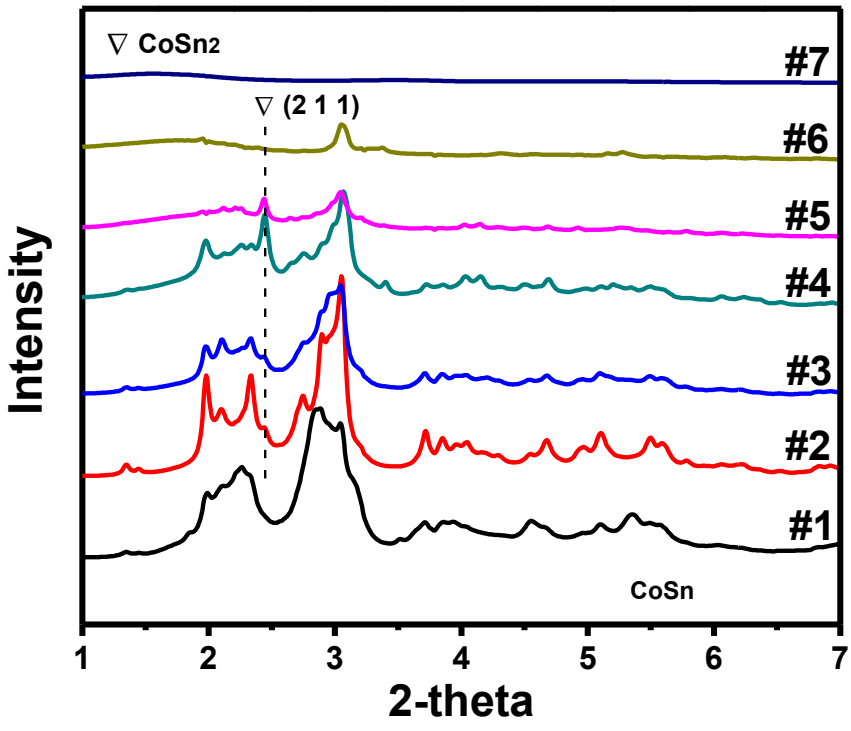

Fig. 5-11 X-ray diffraction patterns of the *x* SiO • (1-*x*) $Sn_{30}Co_{30}C_{40}$ series of samples

emerges gradually and becomes stronger (samples #3, #4 and #5). The XRD pattern for sample #5 shows only two peaks, which can be attributed to (2 1 1) $CoSn_2$ and (2 0 1) CoSn. The XRD pattern for sample #6 shows a $CoSn_2$ peak and a very broad peak at low 2θ, indicating a large amount of amorphous phase (SiO). Moreover, after milling, the samples trend to be highly disordered due to the collapse of the crystal structure. Samples thus undergo a transition from crystalline to amorphous phase during milling.

Conventional XRD is not suitable for identifying amorphous materials because of their broad scattering features. X-ray *PDF* is a powerful tool for probing the local structures that may associate with specific electrochemical properties. Fig. 5-12 shows the *PDF* patterns of the seven composite materials. The SiO content of the samples increases from the bottom of the graph to the top. The differences in the *PDF* patterns for samples #1, #2, and #3 are difficult to distinguish from each other. In the *PDF* patterns from sample #4 and beyond, the first correlation peak for the Si-O bonds of SiO_2 belonging to SiO emerges at 1.61 Å. This peak grows stronger from sample #4 to sample #6, corresponding to the increase of SiO content. The peak for sample #4 at 2.63 Å, which belongs to the first correlation of Co-Sn bonds of CoSn, becomes broader for samples #5 and #6 and decreases to 2.35 Å. The peak at 2.35 Å is the first correlation of Si-Si bonds of Si nanoparticles embedded in silica matrix. The pattern for sample #7 (pure SiO) has short-range order below 5 Å without periodic crystal structure in the long range. Due to the insensitivity of X-rays to light elements, graphite and carbide compounds were not clearly observed. Hence, the neutron *PDF* experiment was carried out on as-milled $Sn_{30}Co_{30}C_{40}$ and sample #4 (50 wt.% SiO-50 wt.% $Sn_{30}Co_{30}C_{40}$). Fig. 5-13 shows that the peaks of as-milled $Sn_{30}Co_{30}C_{40}$ are located at 1.4 Å and 2.47 Å, corresponding to the first

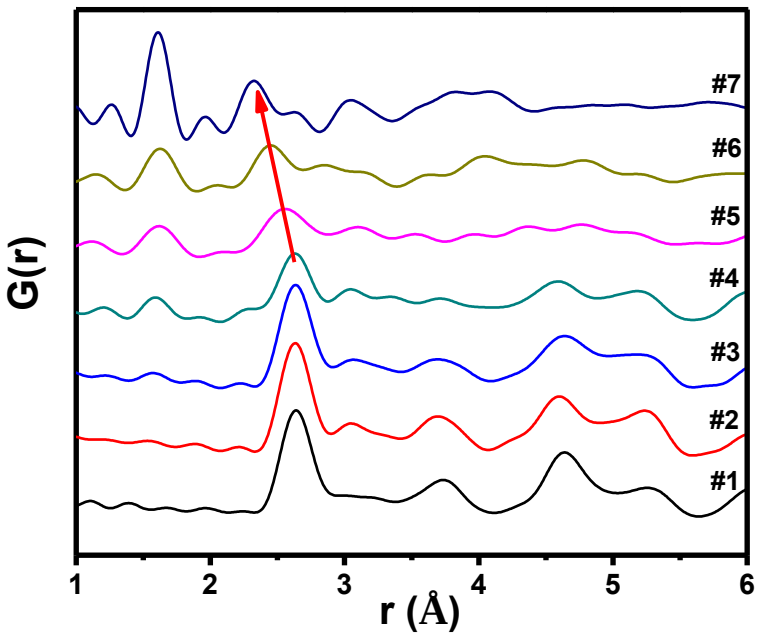

Fig. 5-12 Pair distribution function profiles of the xSiO • (1-x)$Sn_{30}Co_{30}C_{40}$ series of samples

and second C-C bond correlations of graphite (*P 63/m m c*), respectively. Also, a small peak arises at 1.94 Å, which matches the Co-C bond distance of Co_2C, and CoSn alloy is the dominant phase. The *PDF* pattern in Fig. 5-13 for sample #4 indicates Si-O bond correlation of SiO_2 at 1.61 Å. Also apparent is the C-C bond peak of graphite, which affects the shape of the Si-O peak. Both CoSn and $CoSn_2$ phases are found in the neutron *PDF* pattern, a finding that is consistent with the X-ray *PDF* result.

Fig. 5-14 shows the capacity vs. cycle number for half-cells with anodes made from the seven compositions in Table 5-2. These half-cells were cycled with a current density of 100 mA/g for the initial 2 cycles and 300 mA/g in the following cycles between 0.005 V and 1.5 V. It can be seen that sample #7 (SiO) yields the highest capacity, but it rapidly fades in 50 cycles. The reversible capacity decreases from 2450 to 400 mAh/g after 50 cycles. The declining curves for samples #5 to #7 indicate that active material is falling

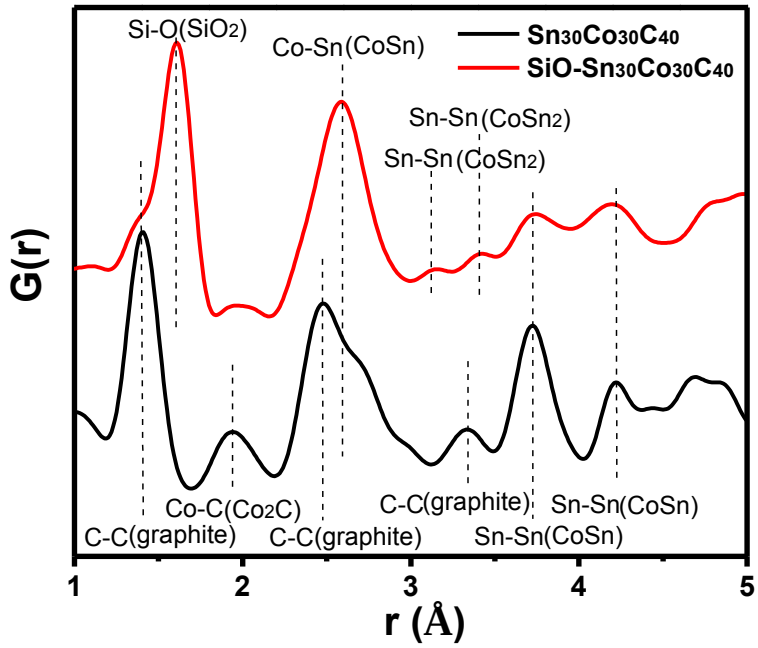

Fig. 5-13 The neutron PDF patterns of as-milled $Sn_{30}Co_{30}C_{40}$ and 50wt.%SiO-50wt.%$Sn_{30}Co_{30}C_{40}$ samples

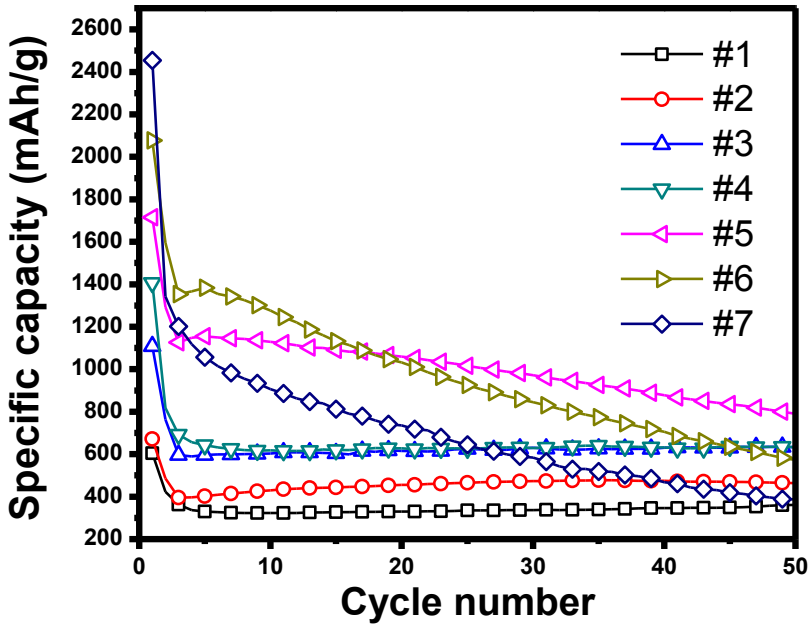

Fig. 5-14 Cycle performance of the *x*SiO • (1-*x*)$Sn_{30}Co_{30}C_{40}$ series of samples

away continuously from the current collector due to the large volume expansion during Li^+ uptake/release, and the amount of Sn-Co-C as buffer component is not sufficient to absorb the change of volume.

After an initial brief decline, the curves for samples #1 to #4 are flat, meaning no further degradation of capacity in 50 cycles. Obviously, Sn-Co-C plays an important role in restraining the volume change and maintaining the capacity. However, the capacity retention was gained at the expense of reversible capacity. Of the first four samples at the 50^{th} cycle, sample #1 delivers the lowest specific capacity, 361 mAh/g, while sample #4 gives the best, 633 mAh/g. As the SiO content increases, the reversible capacity consistently rises from sample #1 to #4. The carbon mainly acts as buffer and prevents Sn agglomeration. We concluded that the sample #4 composition represents the optimum tradeoff between the capacity and cycle life.

Fig. 5-15 shows potential vs. specific capacity plots for the seven compositions of xSiO • (1-x)$Sn_xCo_yC_z$ as anode material. The first discharge process occurs at approximately 0.4 V. The lithiation of pristine crystalline silicon is accompanied by a long flat (slightly decaying) voltage region at approximately 0.15 V, as observed for sample #7. For the other samples (no or a low amount of SiO), the shape of the voltage-capacity curves is associated with tin lithiation in various stages and an amorphous phase.[25] These samples (#1 and #2) were cycled at a high current rate of 100 mAh/g (~C/7 to C/8) and attained the first cycle capacity of 700 mAh/g, as compared with the SiO-rich samples (#3~#7) where the first cycle capacity is between 1300 and 2500 mAh/g, and the current rate is between ~C/13 and C/25.

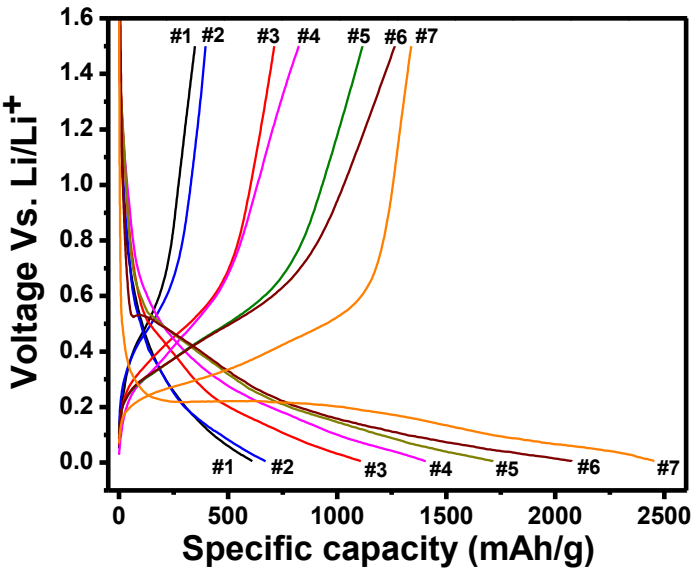

Fig. 5-15 The first cycle voltage profile of the SiO • (1-*x*)$Sn_{30}Co_{30}C_{40}$ series of samples

Based on an overall consideration of capacity and cycle life, the composite anode material yields the best electrical performance when *x* is equal to 0.5. In previous work, we used two milling methods to prepare this material.[19] Samples made by the planetary milling machine had higher capacity (~900 mAh/g) with long cycle life. So the x = 0.5 sample was selected for detailed studies. Fig. 5-16 shows the voltage profile of the Li/SiO-$Sn_{30}Co_{30}C_{40}$ cell (cycled at 50 mA/g). We chose 27 cut-off voltages during the charge-discharge process to simulate the in-situ study, in which the Cu current collector would have contaminated the XRD and *PDF* results. The XRD and *PDF* patterns collected from different charge and discharge voltages are presented in Fig. 5-16 (right). To better visualize the changes in patterns for different voltages, Fig. 5-17 and 5-18 show selected XRD and *PDF* scans taken from Fig. 5-16, respectively, where obvious changes are visible. From the discharge XRD pattern (Fig. 5-17a), it can be seen that the crystal phases of milled SiO-$Sn_{30}Co_{30}C_{40}$ contain Co and $CoSn_2$, which are consistent with EXANES results.[19]

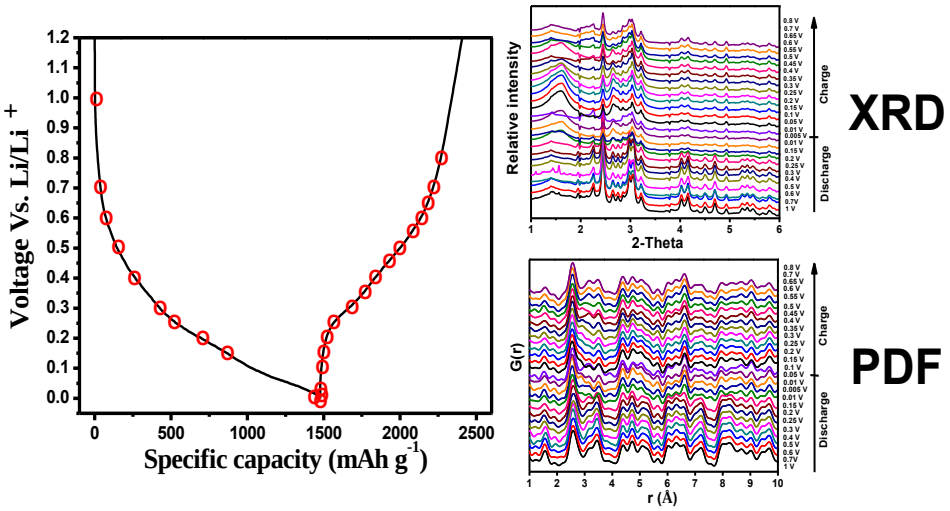

Fig. 5-16 Selected points on charge-discharge curve for X-ray diffraction and PDF investigation

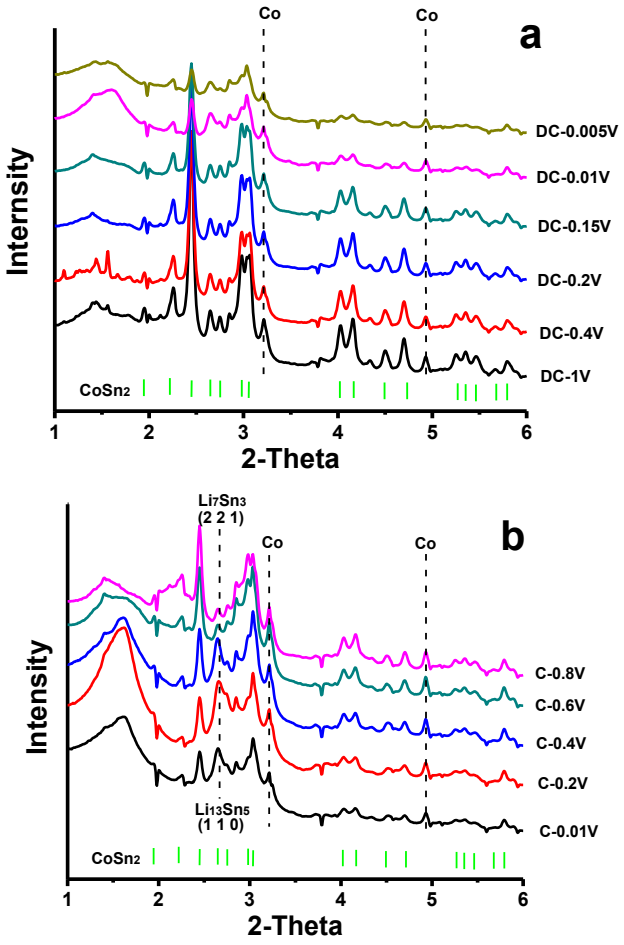

Fig. 5-17 Selected XRD patterns shown from Fig. 5-16, (a) discharge and (b) charge

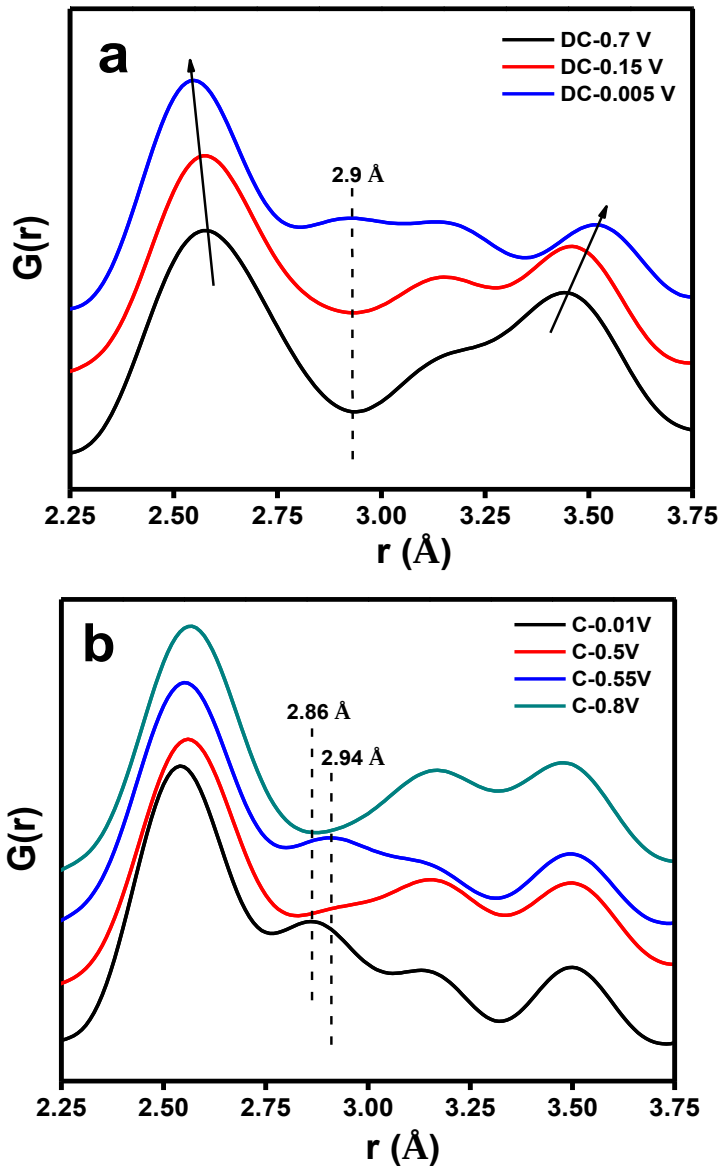

Fig. 5-18 Selected PDF patterns shown from Fig. 5-16, (a) discharge and (b) charge

Because Co is an inactive material, its peaks did not change during the discharge. Also, the $CoSn_2$ phase peaks showed no obvious change until the voltage decreased to 0.15 V. After that, the phase began to react with Li. The nonabsence of the $CoSn_2$ peaks suggests that a large amount $CoSn_2$ remained after the first discharge. In the meanwhile, a broad peak protruded at low 2θ, meaning that a large amount of amorphous phases had formed. The amorphous phase might be attributed to the formation of Li_xSi alloys after lithiation.

Crystalline silicon becomes amorphous during lithium insertion, according to previous studies.[26]

Fig. 5-17b shows no change of cobalt peaks in the charge, the same as was the case for discharge. The XRD pattern of the cell charged to 0.01 V shows a peak appearing at 2θ = 2.63, which is probably (1 1 0) $Li_{13}Sn_5$. This peak is the second strongest peak of $Li_{13}Sn_5$, where I(*f*) is equal to 62%. It is reasonable to speculate about the formation of $Li_{13}Sn_5$ alloy after lithiation. When the cell was charged to 0.2 V, the intensity of the peak (2θ = 2.63) became stronger, which might be due to the phase transition to Li_7Sn_3. The strongest peak (2 2 1) of Li_7Sn_3 (I(*f*) = 100%) appears at 2θ = 2.638, which overlaps with the peak of $Li_{13}Sn_5$. The peaks of $CoSn_2$ were reformed when the cell was charged to 0.8 V. Based on the stability of the $CoSn_2$ phase at this voltage during the discharge and the fact that the observed capacity is not due to the SiO component or SEI formation (225 mAh/g is obtained as discharge capacity in the third cycle at 0.3V), some lithium insertion in nanostructured $CoSn_2$ is believed to happen via the following intercalation/conversion reaction: $CoSn_2 + (x+xy)\ Li \leftrightarrow (1+y)\ Li_xSn + CoSn_{1-y}$.

We selected 3 voltages and 4 voltages from the discharge and charge curves in Fig. 5-16 (left), respectively, which revealed obvious changes in the ex-situ *PDF* patterns. These voltages are given in the *PDF* plot of Fig. 5-18. During discharge, a new peak, shown in Fig. 5-18a, protrudes around 2.9 Å, which most likely associated with Li-Sn alloys, such as $Li_{13}Sn_5$. The first Sn-Sn correlation of $Li_{13}Sn_5$ is located at 2.86 Å. Meanwhile, the 2.6 Å peak shifts to lower value (approximately 2.55 Å) and the 3.44 Å peak shifts to higher values (approximately 3.54 Å) with the Li^+ ion uptake. The former shift may be ascribed to the formation of more multiply bonded Sn-Sn linkages after Li^+ insertion, while the

latter shift can be ascribed to the second correlation of Co, which is probably due to the formation of Co. That can be represented by the following conversion reaction: $CoSn_2 + 2xLi \leftrightarrow 2Li_xSn + Co$. During charge (Fig. 5-18b), the bond correlations of $CoSn_2$ were still absent, which demonstrates a large amount of $CoSn_2$ remaining after the first cycle. The *PDF* pattern for the cut-off voltage of 0.01 V shows a peak at 2.86 Å, which fits the Sn-Sn bond distance of $Li_{13}Sn_5$ alloy. When cells were charged to 0.5 V, this peak disappeared gradually. Another peak at $2\theta = 2.94$ emerged, until cells were charged to 0.55 V. This behavior tallies closely with the Sn-Sn bond distance of Li_7Sn_3. The peaks of Li-Sn alloys were not observed until the cell was charged to 0.8 V. The *PDF* results reflect the phase transformation during the charge-discharge process, which is consistent with the XRD results. They suggest formation of Li-Sn alloys, such as $Li_{13}Sn_5$ and Li_7Sn_3, and intercalation/conversion reactions.

In order to demonstrate the feasibility for practical use, we prepared an anode of 50 wt.% SiO-50 wt.% $Sn_{30}Co_{30}C_{40}$ prepared by ultra high-energy milling.[12] Because of low first-cycle coulombic efficiency, we coated the material with solid lithium metallic powder (SLMP), developed by FMC Corporation. This coating can effectively compensate for irreversible capacity and increase the energy density. The amount of lithium powder for the coating was calculated according to the first-cycle capacity loss of the anode electrode. Then, SLMP was dispersed in solvent (p-xylene) and built up to homogeneous suspension, which was coated on the electrode surface. All the fabrication process was handled in an Argon-filled glove box. For the full-cell configuration test, we used Toda HE5050 ($Li_{1.2}Ni_{0.15}Co_{0.10}Mn_{0.55}O_2$) as the cathode, which is composed of 84% active material, 8% conductive additive, and 8% binder solution and has a loading mass

of 7.44 mg/cm^2 without Al foil. The voltage window was set up between 2.0 V and 4.5 V, and the current was 0.2 mA. The full cell achieved good cycle life in 200 cycles with 72% capacity retention and nearly 100% Coulombic efficiency, as shown in Fig. 5-19. The voltage profile also shows good voltage and capacity retention over 200 cycles.

5.5 Conclusion

In this work, we have developed and characterized a new composite anode material SiO/$Sn_{30}Co_{30}C_{40}$ for lithium batteries and investigated its electrochemical performance. We employed two different mechanical alloying machines, which show different milling effects on the aspects of particle size, phases, and performance of cells. A remarkable improvement of specific capacity was obtained through UHEM. In half-cell tests for over

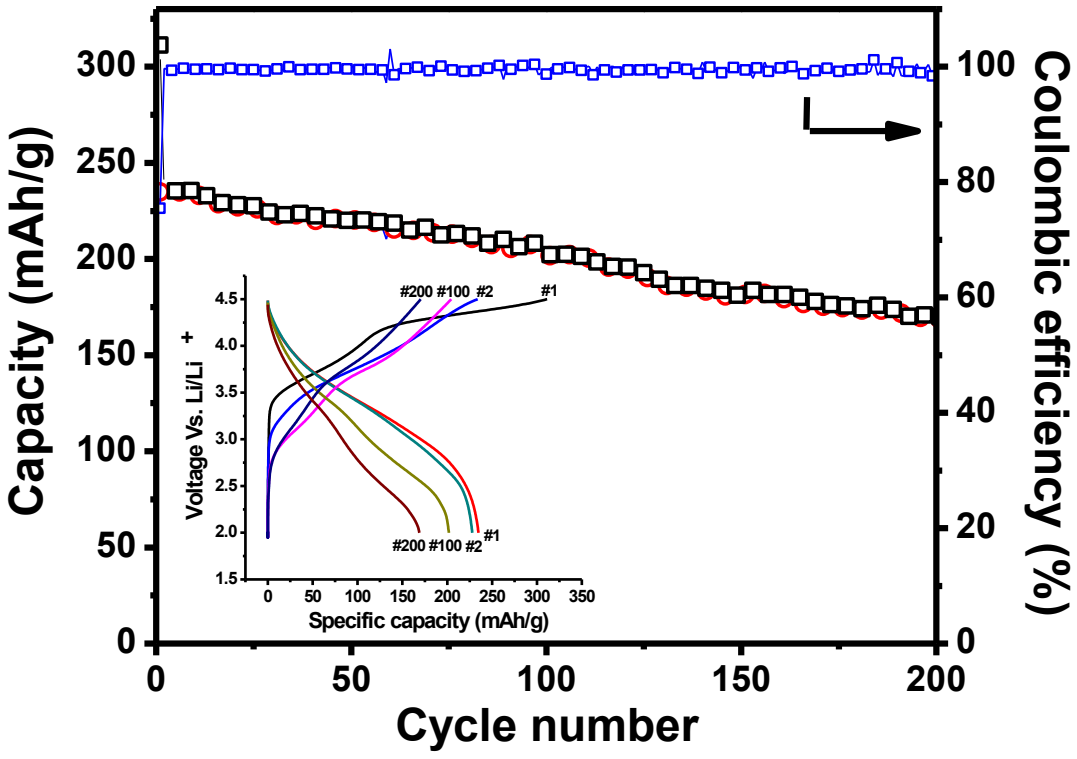

Fig. 5-19 Cycle performance of the full cell based on $Li_{1.2}Ni_{0.15}Co_{0.10}Mn_{0.55}O_2$ vs. 50wt.%SiO-50wt.%$Sn_{30}Co_{30}C_{40}$ with SLMP coating

100 cycles, the UHEM SiO/$Sn_{30}Co_{30}C_{40}$ composite electrode operated at capacity levels as high as 700 mAh/g at a current of 1C and 900 mAh/g at a current of C/3 and room temperature, with very stable capacity at high temperature. The stable lithium metallic powder technique improves the Coulombic efficiency to 86% for the half-cell. Furthermore, the feasibility of operating a full cell (OAC anode coupled with $Li_{1.2}Ni_{0.3}Mn_{0.6}O_{2.1}$ cathode) has been demonstrated. Then, we prepared a series composite anode material of xSiO • (1-x)$Sn_xCo_yC_z$ by SPEX ball milling and studied by electrochemical method. The composition of 50 wt.% SiO-50 wt.% $Sn_{30}Co_{30}C_{40}$ shows the best electrochemical performance of 633 mAh/g after 50 cycles. So this combination was selected for detailed studies. X-ray and neutron PDF techniques exhibits different information about as-milled 50wt.% SiO-50wt.%$Sn_{30}Co_{30}C_{40}$. From neutron PDF patterns, C-C bond peaks of graphite were easily observed. Ex-situ X-ray diffraction and PDF study of different cut-off voltages reveals the phase transformation during interclation/convertion reaction, $CoSn_2 + (x+xy)Li \leftrightarrow (1+y)Li_xSn + CoSn_{1-y}$. The stable lithium metallic powder technique was used to improve the first cycle Coulombic efficiency. Full-cell configuration ($Li_{1.2}Ni_{0.15}Co_{0.10}Mn_{0.55}O_2$ vs. 50 wt.% SiO-50 wt.%S $n_{30}Co_{30}C_{40}$) has been cycled over 200 cycles.

5.6 Reference

[1] Y. Idota, T. Kubota, A. Matsufuji, Y. Maekawa and T. Miyasaka, *Science*, 1997, **276**, 1395.

[2] U. Kasavajjula, C. Wang and A. John Appleby, *J. Power Sources*, 2007, **163**, 1003.

[3] S. H. Lee, Y. H. Kim, R. Deshpande, P.A. Parilla, E. Whitney, D.T. Gillaspie, K.M. Jones, A.H. Mahan, S. Zhang and A.C. Dillon, *Adv. Mater.*, 2008, **20**, 3627.

[4] P. Poizot, S. Laruelle, S. Grugeon, L. Dupont and J. M. Tarascon, *Nature*, 2000, **407**, 496.

[5] M. S. Park, G. X. Wang, Y. M. Kang, D. Wexler, S. X. Dou and H.-K. Liu, *Angew. Chem. Int. Ed*., 2007, **46**, 750-753.

[6] Y. Nagao, H. Sakaguchi, H. Honda, T. Fukunaga and T. Esaka, *J. Electrochem. Soc*., 2004, **151**(10), A1572-A1575.

[7] M.N.Obrovac and L. Christensen, *Solid-State Lett*., 2004, **7**(5) A93-A96.

[8] T. Takamura, S. Ohara, M. Uehara, J. Suzuki and K. Sekine, *J. Power Sources*, 2004, **129**, 96.

[9] C. K. Chan, H. Peng, G. Liu, K. Mcilwrath, X. Zhang, R. A. Huggins and Y. Cui, *Nature Nanotech*. 2008, **3**, 31-35.

[10] A. Timmons, A. D. W. Todd, S. D. Mead, Graham H. Carey, R. J. Sanderson, R. E. Mar and J. R. Dahn, *J. Electrochem. Soc*., 2007, **154**(9), A865-A874.

[11] T. D. Hatchard and J. R. Dahn, *J. Electrochem. Soc*., 2005, **152**, A1445.

[12] T. D. Hatchard, M. N. Obrovac and J. R. Dahn, *J. Electrochem. Soc*., 2005, **152**, A2335.

[13] S. J. Lee, H. K. Baik and S. M. Lee, Electrochem. Commun., 2003, **5**, 32.

[14] M. D. Fleischauer, J. M. Topple and J. R. Dahn, *Solid-State Lett*., 2005, **8**, A137.

[15] C. H. Doh, C. W. Park, H. M. Shin, D. H. Kim, Y. D. Chung, S. I. Moon, B. S. Jin, H. S. Kim and A. Veluchamy, *J. Power Sources*, 2008, **179**, 367–370.

[16] I.-S. Kim, G. E. Blomgren and P. N. Kumta, *J. Power Sources*, 2004, **130**, 275–280.

[17]

Sony News Release, accessed at http://www.sony.net/SonyInfo/News/Press/200502/05-006E/.

[18] A. D. W. Todd, R. E. Mar and J. R. Dahn, *J. Electrochem. Soc*., 2006, **153**(10), A1998-A2005.

[19] A. D. W. Todd, R. E. Mar and J. R. Dahn, *J. Elecrochem. Soc*., 2007, **154**(6), A596-A604.

[20] P. P. Ferguson, A. D. W. Todd and J. R. Dahn, *Electrochem. Commun*., 2008, **10**, 25–31.

[21] P. P. Ferguson, R. A. Dunlap and J. R. Dahn, *J. Electrochem. Soc*., 2010, **157**(3), A325-A332.

[22] A. D. W. Todd, R. A. Dunlap and J. R. Dahn, *J. Alloys and Compounds*, 2007, **443**,

114–120.

[23] P. P. Ferguson, M. L. Martine, R. A. Dunlap and J. R. Dahn, *Electrochem. Acta*, 2009, **54**, 4534–4539.

[24] P. P. Ferguson, Peng Liao, R. A. Dunlap and J. R. Dahn, *J. Electrochem. Soc*., 2009, **156**(1), A13-A17.

[25] R. B. Lewis, A. Timmons, R. E. Mar and J. R. Dahn, *J. Electrochem. Soc*., 2007, **154**(3), A213-A216.

[26] J. Yang, M. Winter and J. O. Besenhard, *Solid State Ionics*, 1996, **90**, 281-287.

[27] C. Syryanarayana, *Prog. Mater. Sci*. 2001, **46**, 1-184.

[28] Ludovic Milin and Raj K. Rajamani, *Mater. Manufact. Proc*. 1997, **12**(2), 241-260.

[29] J. Lu, Y. J. Choi, Z. Z. Fang, H. Y. Sohn and E. Rönnebro, *J. Am. Chem. Soc*.. 2009, **131**(43), 15843-15852.

[30] B. G. Butler, J. Lu, Z. Z. Fang and R. K. Rajamani, *International Journal of Powder Metallurgy* 2007, **43**(1), 35-43.

[31] M. Vergnat, G. Marchal, M. Piecuch and M. Gerl, *Solid State Communications*, 1984, **50**(3), 236-242.

[32] C. Suryanarayana, *Progress in Materials Science*, 2001, **46**, 1-184.

[33] Q. Fan, P. J. Chupas, and M. S. Whittingham, *Electrochem. Solid-State Lett*., 2007, **10**, A274-A278.

[34] J.J. Zhang and Y.Y. Xia, *J. Electrochem. Soc*., 2006, **153**(8), A1465-A1471.

[35] B. Key, M. Morcrette, J. M. Tarascon and C. P. Grey, *J. Am. Chem. Soc*., 2011, **133**(3), 503–512.

[36] Y. Nagao, H. Sakaguchi, H. Honda, T. Fukunaga and T. Esaka, *J. Electrochem. Soc*., 2004, **151**(10), A1572-A1575.

[37] M. Vergna and M. Gerl, *J. Mater. Sci. Technol*. 1993, **9**, 79-88.

CHAPTER 6

SILICON MONOXIDE/TIN-IRON-CARBON COMPOSITE

6.1 Introduction

In 1991, Sony released the world's first commercial lithium-ion rechargeable battery. Since then, lithium-ion batteries (LIBs) have been commercially used in portable devices such as cell phones and laptop computers over the past 20 years. Furthermore, LIBs are considered as the most promising power source for hybrid electric vehicles (HEVs) and plug-in HEVs. The most challenging goal for that application is to develop high-power density electrode materials. The conventional anode material, graphite, has a gravimetric and volumetric capacity of 372 mAh/g and 818 Ah/L, respectively, corresponding to the intercalation of one Li per six C. Due to the limited theoretical capacity, graphite is not a suitable material for the next-generation LIB anode. Metal alloys anode materials involving as Si, Sn, Ge, Mo, Al, etc. have shown high capacity, acceptable rate ability, and better safety. Unfortunately, the major weakness is huge volume change during the Li^+ insertion and removal, which results in cycle life that is too low for practical use. Owing to the demands for alternative anodes with both higher volumetric and gravimetric capacities than carbon, Sn and Si oxides appear as the best candidates. Compared with pure metals, oxides exhibit better cycle life. For example, amorphous tin oxide follows a two-step process during charge and discharge.[1,2] First, the SnO_2 reacts with Li to form amorphous Li_2O and metallic Sn. Second, Sn is alloyed with Li^+ and forms a series of

compounds: $Li_{22}Sn_5$, Li_7Sn_2, Li_3Sn, Li_5Sn, LiSn, and Li_2Sn_5. In this process, Li_2O acts as a buffer material to restrain volume change. Nevertheless, the cycle life of oxides is still far from practical LIB use.

An intermetallic compound, such as Sn-M-(C), can also be employed to overcome volume expansion, where Sn acts as an active phase, and "M" is a transition metal that does not react with lithium. SONY developed a lithium-ion battery called NEXELION, using an amorphous ternary Sn-Co-C composite as the anode.[3] Tin, cobalt, and carbon were mixed into the composite on a nanometer level for improving energy density and cycling performance. Dahn's group developed an extensive infrastructure for studies of nanostructured Sn-Co-C alloys.[4-11] Unfortunately, this material is not the optimal candidate for electric vehicles and large-scale use due to its high cost and the toxicity of cobalt. Therefore, the Sn-Fe-(C) system was investigated in the hope of obtaining a superior anode material.[12-16] A series of Sn-Fe-(C) alloys was prepared by mechanical alloying and direct melting of elements.[13-15] Iron was chosen because it does not alloy with Li and should form an inactive matrix for the tin atoms. Various alloys were prepared according to the Gibb's composition triangle.[13] The binary Sn-Fe system contains several intermetallic phases of SnFe, Sn_2Fe, Sn_2Fe_3, and Sn_3Fe_5. Specific capacities of 804 mAh/g, 676 mAh/g, 582 mAh/g, and 557 mAh/g are expected for Sn_2Fe, SnFe, Sn_2Fe_3, and Sn_3Fe_5 if all compounds react fully with Li to form $Li_{4.4}Sn$ and Fe. Dahn's group synthesized a series of Sn-Fe alloys by mechanical alloying.[14] Materials processed by mechanical alloying have much larger capacity than those made only by high-temperature annealing, presumably because of their smaller particle and grain size. As the Fe content in the Sn-Fe intermetallic compound increases, the cycle life of the

materials improved. Dahn et al. explained that the formed Fe and residual starting material act as a "matrix" to hold the Sn and Li-Sn alloys together during cycling. Therefore, they used Sn_2Fe as an active phase (that is, it reacts completely to form $Li_{4.4}Sn$ and Fe) and $SnFe_3C$ as an inactive phase (that is, it reacts with very little Li). Cell tests had shown that the $SnFe_3C$ anode attained 100 mAh/g reversible capacity with good cycle performance.[14] By increasing the amount of Sn_2Fe, cells exhibited higher capacity but capacity retention is poor. The best cycling performance was observed for anode material with about 24% active phase (Sn_2Fe), 72% inactive phase ($SnFe_3C$), and 4% C, where 200 mAh/g discharge capacity was sustained for more than 80 cycles.[15]

We previously developed a novel composite anode material SiO-$Sn_{30}Co_{30}C_{40}$ that was formed by mechanical alloying.[17] Mechanical alloying is an effective and low-cost way to synthesize nano and amorphous materials. Whittingham and co-workers have studied crystalline and amorphous Sn-Co alloy and characterized that using pair distribution function method.[18,19] They concluded that nanosized amorphous tin–cobalt materials showed enhanced cycling behavior over the crystalline SnCo analog and over crystalline tin. Silicon monoxide was chosen to be the milling component because it can produce high capacity (>1400 mAh/g). A 50 wt.% SiO-50 wt.% $Sn_{30}Co_{30}C_{40}$ composite electrode delivered 700 mAh/g and 900 mAh/g reversible capacity at rates of 900 mA/g and 300 mA/g, respectively, over 100 cycles. It also showed very stable capacity at high temperature (50ºC). The feasibility of the full-cell configuration of this anode coupled with a $Li_{1.2}Ni_{0.3}Mn_{0.6}O_{2.1}$ cathode was demonstrated.

In this work, we eliminated the expensive and toxic cobalt from the anode material and replaced it with cheap and environmentally benign iron, resulting in a SiO-$Sn_xFe_yC_z$

composite. The Sn-Fe-C alloy has been used as a buffer material to extend the cycle life of cells. Therefore, the aim of our work is to find the optimal capacity and cycle life by tuning the composition of Sn-Fe-C. We fixed the amount of SiO as 50 wt.% and Sn-Fe-C as 50 wt.%, then tuned the Sn-Fe-C composition. The Gibbs composition triangle in Fig. 6-1 indicates the various alloys we have investigated, which are marked by red points. The as-milled samples can be divided into two groups: (I) carbon rich and (II) iron rich. Group I contains sample #1, #2, and #3. In this group, the amount of carbon increases with item number. Group II includes sample #4, #5, and #6, in which the amount of iron increases with item number. We investigated the effect of carbon and iron in the composite material on the electrochemical performance. Then, we studied the anode composition of 50 wt.% SiO-50 wt.% $Sn_{30}Fe_{30}C_{40}$ in detail. The above composite materials were characterized by X-ray diffraction (XRD), pair distribution function (*PDF*) measurements, and electrochemical testing.

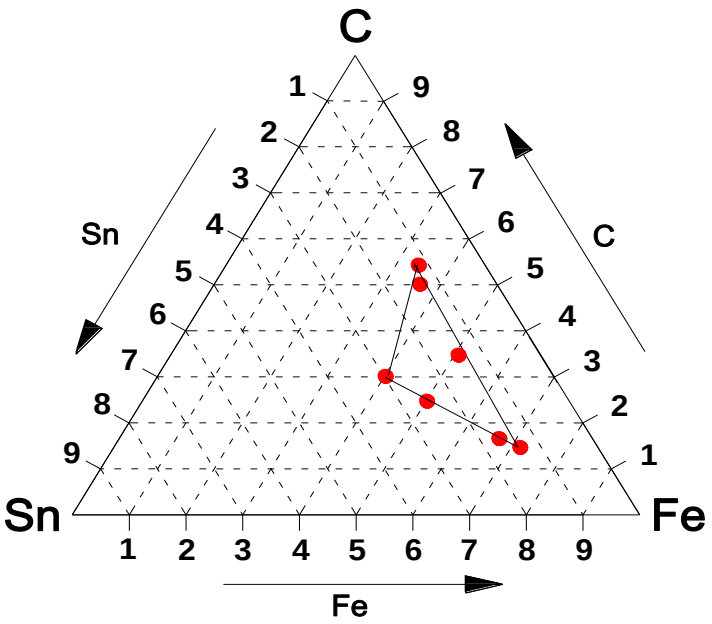

Fig. 6-1 Gibbs composition triangle for Sn-Fe-C (The marked compositions indicate those that have been investigated in this series of studies.)

6.2 Experimental Procedure

6.2.1 Preparation of SiO-$Sn_xFe_yC_z$ Composites

The raw materials for this work, Silicon monoxide (99.99%, -325 mesh, Sigma-Aldrich), Tin (99%, powder, Sigma-Aldrich), Iron (99%, fine powder, Sigma-Aldrich), and Graphite (Hitachi), were purchased commercially. Mechanical alloying has proven to be an efficient processing technique to prepare powders with small grains. The raw materials were mixed homogeneously in select proportions. Then, the mixture was milled mechanically with a SPEX 8000 mixer/mill machine for 48 hours. Five grams of mixed powder was milled in a round-ended hardened steel grinding vial (35 mL) containing two 1/2-in. (12.7 mm) and four 1/4-in. (6.35 mm) steel balls. All the material handling was carried out in a glove box filled with purified Argon and controlled H_2O concentration. See Table 6-1 for sample compositions.

Table 6-1 Compositions and properties of the composite alloy samples

Sample #	50 wt.% SiO-50 wt.% $Sn_xFe_yC_z$				Particle size (μm)	Reversible capacity (mAh/g, 3rd cycle)	Reversible capacity (mAh/g, 100th cycle)
	SiO (wt.%)	Sn	Fe (at.%)	C			
1	50	16.7	50	33.3	9.08	695	397
2	50	12.5	37.5	50	8.62	644	472
3	50	11.1	33.3	55.6	9.20	620	538
4	50	25	50	25	7.79	706	333
5	50	16.7	66.6	16.7	8.99	646	511
6	50	14.3	71.4	14.3	10.27	578	440

6.2.2 Electrochemical and Physical Characterization

The electrochemical performance was determined in tests with CR 2032-type coin cells at room temperature. The electrode laminate was prepared as a thin film by doctor-blade deposition (150 μm) on a copper substrate of a slurry composed of 80 wt.% active material, 10 wt.% acetylene black as the conductive agent, and 10 wt.% U-Varnish polyimide binder. Lithium foil served as the counter electrode, and the electrolyte consisted of a 3:7 weight ratio of ethylene carbonate and ethyl methyl carbonate, with 1.2 M LiPF6. The cells were assembled in an Argon-filled glove box and tested to cut-off potentials of 0.005 V-1.5 V (vs. Li/Li^+). The cells were tested with constant charge and discharge currents (100 mA/g at the first two cycles and 300 mA/g at subsequent cycles). The cells were tested on a Maccor cycler.

Room-temperature Mössbauer measurements were made in transmission geometry using 20 mCi Co-57m in a Rh matrix. The 14.4 keV nuclear resonance X-rays were measured with a Canberra GL0515R/S germanium detector. The spectra were calibrated with a 5-micron α-Fe foil.

Ex-situ powder XRD data were collected from the 11-ID-C beam line at the Advanced Photon Source (APS) of the Argonne National Laboratory. Scattering patterns were acquired with two-dimensional (2D) detectors. 2D images were converted into 1D Q-space versus intensity plots by using the FIT2D with a CeO_2 calibration standard. The X-ray wavelength was preset to 0.10798 Å (fixed wavelength for this beam line). Use of a high-energy X-ray beam is important for obtaining the necessary penetration to detect structural changes and for collecting diffraction data at high wave vectors. The high flux of the X-ray beam at APS is able to carry out fast experiments at one spectrum per

minute. The samples were loaded in a cylindrical geometry polyimide capillary (d = 0.5 mm). The detector was set up at a distance of around 1800 mm to the samples for diffraction. For the ex-situ *PDF* (Pair distribution function) test, 30 spectra were collected to reduce the error at high angle. The final *PDF* value is the average of 30 spectra. The detector was moved to about 300mm distance away from samples.

6.3 Material Characterization and Electrochemical Properties of 50 wt.%SiO-50 wt.% $Sn_xFe_yC_z$

The structural characteristics of the compound of the 50 wt.% SiO-50 wt.% $Sn_xFe_yC_z$ (x=1, $2\leq y\leq 5$, $2\leq z\leq 5$) were investigated by high-energy XRD. Fig. 6-2 shows the XRD patterns, and Table 6-1 lists the phases that were detected. The value of x is fixed to 1 because a large portion of Sn leads to rapid capacity degradation. Group I (samples #1, #2, and #3 with increasing carbon) shows very similar XRD patterns. A very broad peak can be observed at low 2θ, indicating a large amount of amorphous phase, which might be amorphous SiO_2 embedded in SiO or some new phases formed after ball milling. The dominant phases are Fe_3Sn, $FeSn_2$, Sn, and α-Fe. According to many studies, carbon mainly plays the role of buffer material, but does not involve new phase formation during mechanical alloying.[7] The Raman scattering pattern of milled SiO-$Sn_{30}Co_{30}C_{40}$ in our previous paper showed peaks at 1578 and 1340 cm^{-1}, which were assigned to the G and D bands of graphite.[17] It can be seen that the XRD patterns for Group I scarcely changed with the amount of carbon increased from 33.3 at.% to 55.6 at.%. In Group II (sample #4, #5 and #6), the amount of iron increased from 50 at.% to 71.4 at.%. In the XRD pattern of sample #4, $FeSn_2$ peaks protrude from the background, compared with the samples of Group I, indicating a large amount of $FeSn_2$ in the mixture. The $FeSn_2$ phase is prone to be formed at a similar atomic ratio of Fe and Sn during milling. As mentioned above,

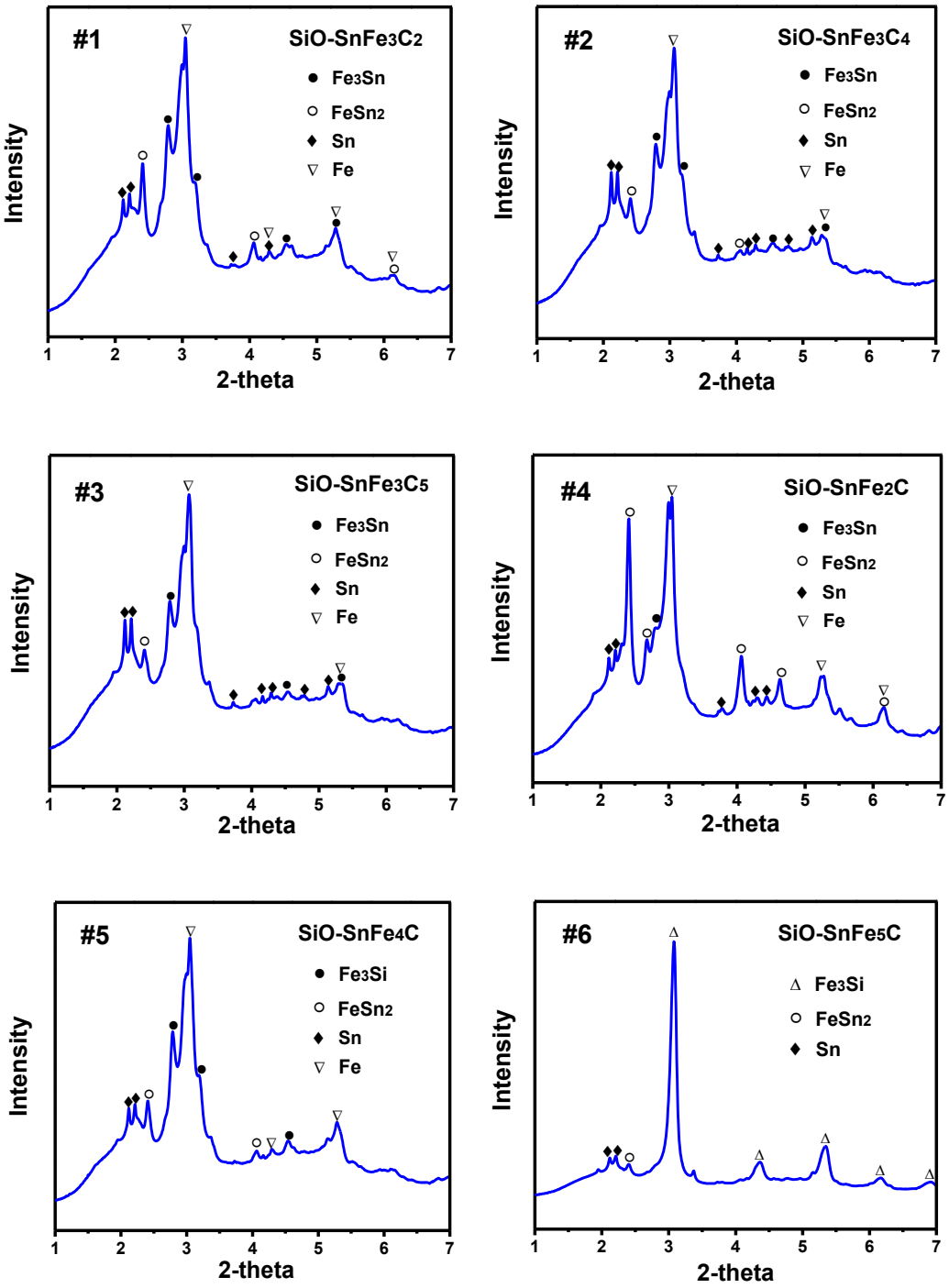

Fig. 6-2 XRD patterns of as-milled samples from Group I (#1, #2, #3) and Group II (#4, #5, #6)

although $FeSn_2$ intermetallic compound delivers an extremely high specific capacity of 804 mAh/g, it should be avoided due to its fast degradation upon cycling. The XRD pattern of sample #5 is very similar to that of the Group I samples. Thus, no significant difference was observed in the XRD patterns of samples #1 to #5. The increase in the amount of iron in Group II leads to the formation of Fe_3Si in sample #6. The presence of Fe_3Si in samples #1 to #5 cannot be excluded because of the large amount of amorphous phase. Furthermore, α-Fe and Fe_3Si have the same space group (*Im-3m*). Compared with the five other samples, sample #6 is more crystalline and contains the Fe_3Si phase as a result of the large amount of Fe added. In this sample, Fe_3Si with cubic structure is the dominant phase; Sn and $FeSn_2$ are minor phases. Commercial SiO is known to be an amorphous phase. The structure of SiO consists of nanoparticles of Si distributed in a matrix of amorphous SiO_2. Nagao and co-workers found that amorphous SiO is composed of silica-like glass and metallic silicon cluster based on a comparison between the radial distribution functions [*RDF*(r)] of SiO and SiO_2.[20] During the milling process, nanosize Si particles embedded in SiO_2 react with Fe to form crystal Fe_3Si.

Compared with carbon, iron is highly associated with the phase change of the composite anode materials during mechanical alloying. The *PDF* technique was used to probe the local structure. This technique is a highly effective tool for characterizing materials that do not possess the periodicity of a crystal structure, such as amorphous SiO. Fig. 6-3 shows the *PDF* patterns with the correlations to 15 Å. Line 1 located at 1.61 Å was observed in all samples, corresponding to Si-O bonds of SiO_2. Obviously, SiO_2 embedded in SiO is very stable during ball milling process. It can be seen that there is a very broad, non-Gaussian shaped peak at line 3 found in the *PDF* patterns of samples #1

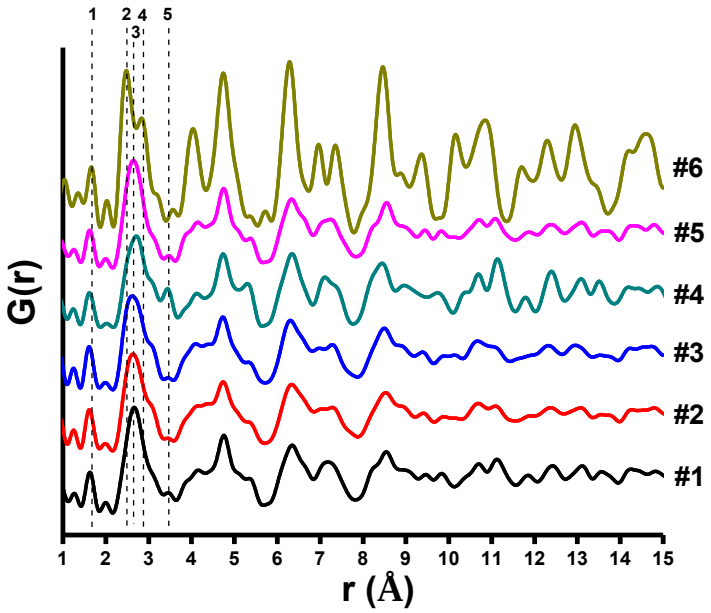

Fig. 6-3 *PDF* patterns of as-milled samples from Group I (#1, #2, #3) and Group II (#4, #5, #6)

to #5, which is made up of Fe-Fe bonds (2.539 Å and 2.932 Å) in α-Fe, Fe-Sn bonds (2.789 Å) in $FeSn_2$, and Fe-Fe bonds (2.60 Å) in Fe_3Sn. Due to the many phases and the overlap of peaks, no detailed analysis of the data is included here. The stronger intensity of line 5 at 3.46 Å in the sample #4 corresponds to Sn-Sn bonds ($FeSn_2$), which means that the material contains more $FeSn_2$ than others samples as revealed by XRD results. The sample #6 does not follow the same trend with other samples. The peak at line 3 splits into two peaks corresponding to line 2 and line 4, which are attributed to the first correlation and the second correlation of Fe_3Si. Line 2 and line 4 are contributed from the bonds of Fe-Fe (2.453 Å and 2.833 Å) and Fe-Si (2.453 Å and 2.833 Å) belonging to crystal Fe_3Si. Because sample #6 is highly crystalline, we performed *PDF* fitting using *PDF*gui software. A good fit (R_w=25.63%) is obtained of the *PDF* pattern by only using Fe_3Si phase, as is shown in Fig. 6-4.

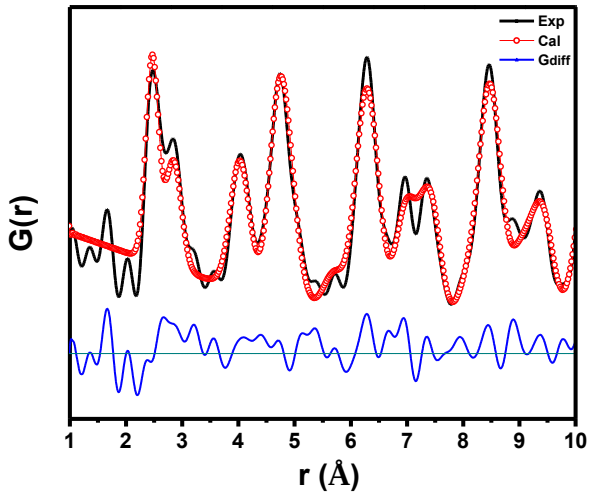

Fig. 6-4 *PDF* fitting result of sample #6 using Fe_3Si phase

Fig. 6-5 shows potential vs. specific capacity plots for the six compositions of SiO-$Sn_xFe_yC_z$ as anode material. The half-cells were operated with a current density of 100 mA/g at the first cycle and 300 mA/g at the 50^{th} and 100^{th} cycles. The cut-off voltage was set between 0.005 V and 1.5 V. As shown in Fig. 6-5, the cells with the different anode compositions have very similar charge/discharge voltage profiles. The average voltage is around 0.2~0.25 V. In the first cycle, these materials deliver very close charge capacity of ~1200 mAh/g and Coulombic efficiency of 50~60%. The irreversible capacity at the first discharge is mainly due to both the formation of an SEI film and Li_2O (oxygen from SiO_2).

Fig. 6-6 compares the cycle-life test results for the Li/SiO-$Sn_xFe_yC_z$ composite half-cells containing the six samples mentioned above. As shown in Fig. 6-6a for Group I, the capacity of the initial cycles decreased with lesser amount of tin, and the anodes having higher carbon content resulted in better capacity retention in subsequent cycles. Obviously, carbon plays a significant role as a buffer matrix in restraining the volume expansion. The anode with sample #3 contains the most carbon and exhibits the best

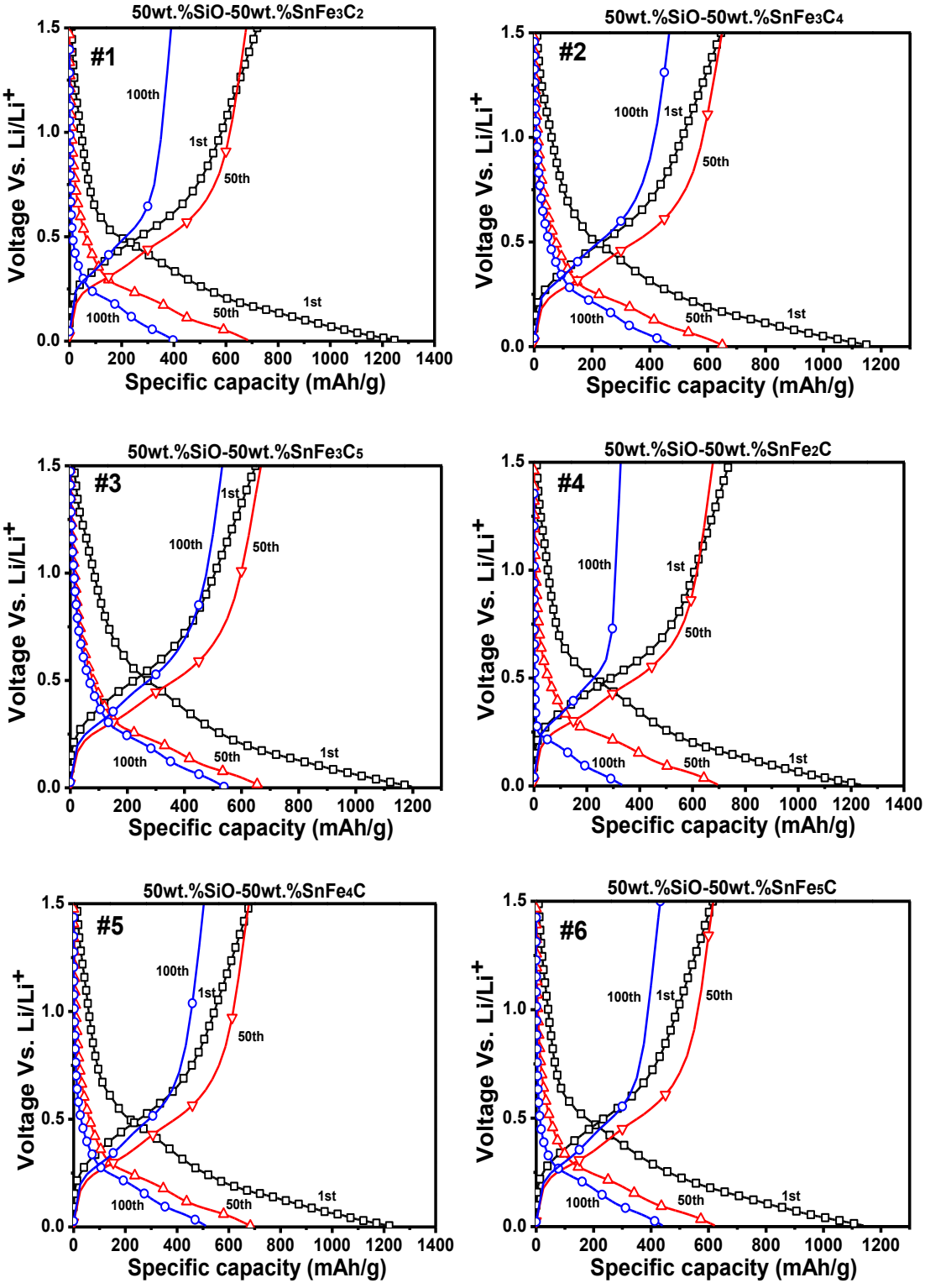

Fig. 6-5 Voltage profile of cells with anodes from Group I (#1, #2, #3) and Group II (#4, #5, #6)

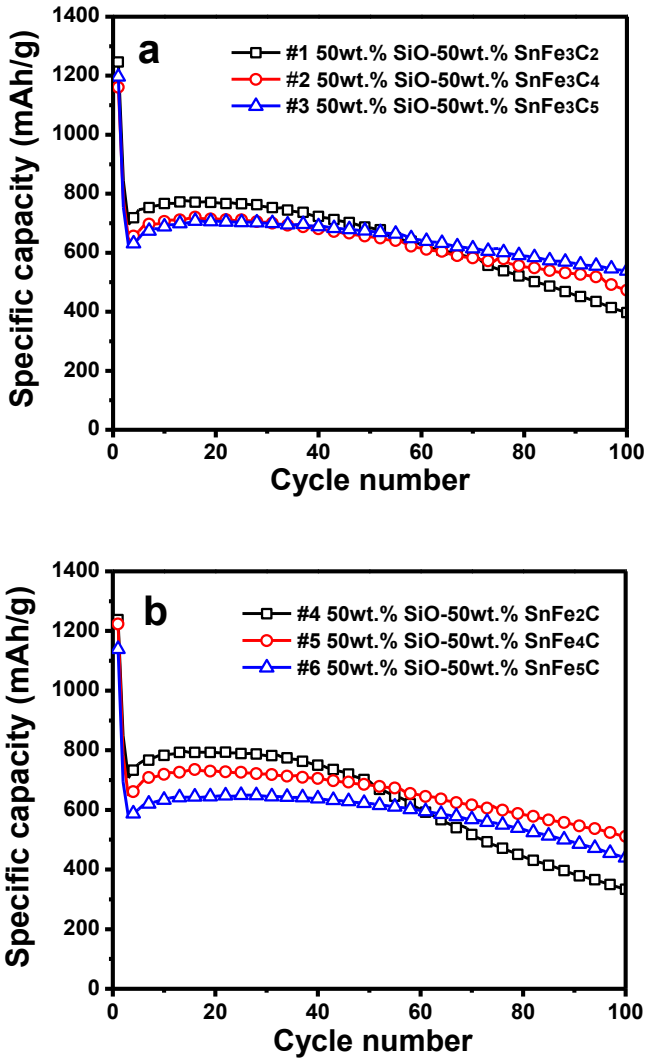

Fig. 6-6 Cycle performance of anodes from as-milled samples in Group I (#1, #2, #3) and Group II (#4, #5, #6)

electrochemical performance with respect to capacity and cycle life. It delivers 620 mAh/g and 538 mAh/g reversible capacities at the 3rd cycle and the 100th cycle, respectively. The capacity retention is 86.8%.

Half-cells with samples from Group II were similarly tested (Fig. 6-6b). Iron is an inactive material for lithiation reaction. Hence, iron could be alloyed with another metal or act as a buffer. The sample #4 anode suffers from rapid capacity degradation because it contains much $FeSn_2$, as indicated by XRD. The best electrochemical performance is

exhibited by the sample #5 anode. The sample #5 and #6 anodes show a similar capacity retention rate (79% and 76%, respectively). Because of the greater amount of tin in the sample #5 compared with sample #6 anode, it delivers more reversible capacity, 511 mAh/g, after 100 cycles. Obviously, iron is not acting as a buffer material as carbon does. On the contrary, excess iron would reduce the capacity. In sum, the sample #3 anode exhibits the best electrochemical performance among Groups I and II.

In order to obtain better electrochemical performance, we adjusted the combination of Sn, Fe, and C. The content of Sn was increased for improving the reversible capacity, while the amount of Fe was limited because of its Li^+ inactive property and poor buffer effect. But it may sacrifice cycle life due to the easy formation of $FeSn_2$ with the close ratio of Sn and Fe. In the meantime, a little bit more graphite was added in for improving cycle performance. According to some literature about the Sn-Co-C system, the composition near $Sn_{30}Co_{30}C_{40}$ was considered to provide the best electrochemical performance in terms of capacity and cycle life.[7,10,21] We also found that this composition exhibited very good cycle life and high capacity in our previous work on SiO-$Sn_{30}Co_{30}C_{40}$.[17] Therefore, a detailed investigation of 50 wt.% SiO-50 wt.% $Sn_{30}Fe_{30}C_{40}$ composite is made in the following study.

The XRD pattern of ball-milled SiO-$Sn_{30}Fe_{30}C_{40}$ is given in Fig. 6-7 and indicates three phases: $FeSn_2$, Fe_3Sn, and Fe. Crystal alloys tend to be highly distorted after mechanical alloying. Bragg peaks protrude on a broad peak at low angle. Graphite peaks are not observed. Also, oxides peaks are not detectable, which implies that milling occurred without significant oxidation or the associated phases might exist in an amorphous state. The lithium intercalation process for Fe-Sn alloys ($FeSn_2$, FeSn, and

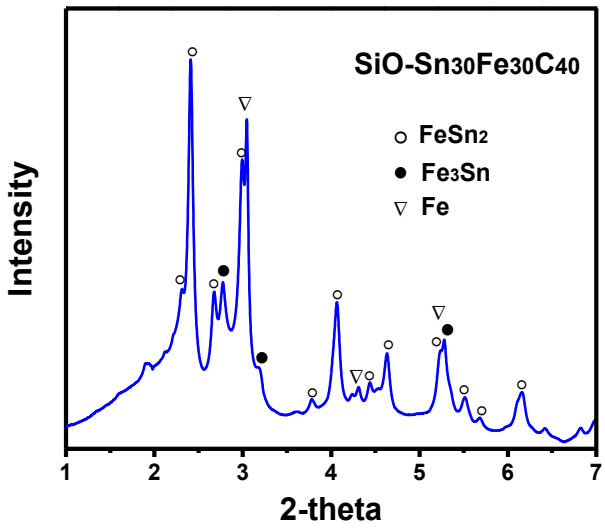

Fig. 6-7 XRD pattern of as-milled 50 wt.% SiO-50 wt.% $Sn_{30}Fe_{30}C_{40}$ composite

Fe_3Sn_2) was reported earlier.[13-15] Both $FeSn_2$ and $CoSn_2$ have the same structure (tetragonal), which belongs to space group I4/mcm with Sn atoms occupying 8h sites and Fe/Co atoms in 4a sites. In the *PDF* fitting for this sample using the three phases of $FeSn_2$, FeSn, and Fe_3Sn_2, the R_w is low at 22.9% (see Fig. 6-8). The main error is due to the Si-O atomic distance (1.61 Å) of SiO_2 embedded in SiO.

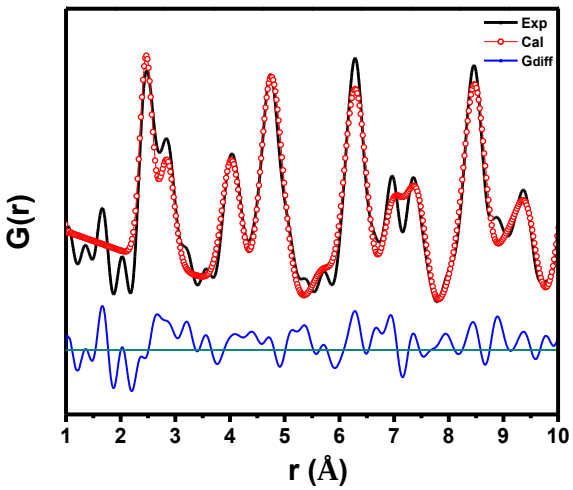

Fig. 6-8 *PDF* pattern and fitting profile of as-milled 50 wt.% SiO-50 wt.% $Sn_{30}Fe_{30}C_{40}$ composite

Mössbauer spectroscopy was performed on the ball-milled SiO-$Sn_{30}Fe_{30}C_{40}$ sample (see Fig. 6-9). Care was taken to focus on the low velocity portion of the spectrum to magnify small features caused by $FeSn_2$ and Fe_3Sn. Instead of conducting Mössbauer spectroscopy from -8 to +8 mm/sec, we cut the range in half, -4 to +4 mm/sec, and thus the outer lines (green peaks 1 and 4) of the magnetic iron metal spectrum are not shown in Fig. 6-9 (which lie at roughly ± 5.3 mm/sec). We fitted the data to Lorentzian functions (constrained to the usual 3:2:1 amplitude ratio for the magnetic spectrum) using a least-square fitting routine and determined the hyperfine parameter values: the isomer shift (measured relative to an α-Fe foil), δ; the magnetic hyperfine field, H_{eff}; and the quadrupole splitting, ε. The spectrum unambiguously shows three iron components: (i) magnetic Fe metal [H_{eff} = 32.7(1) T, δ = 0.04(2) mm/sec, ε = 0.07(5) mm/sec], (ii) nonmagnetic single-line $FeSn_2$ [δ = 0.42(1) mm/sec, ε = 0.004(20) mm/sec], and (iii) nonmagnetic quadrupole split Fe_3Sn [δ = 0.27(1) mm/sec, ε = 0.90(2) mm/sec]. These results are in good agreement with the XRD measurements shown in Fig. 6-5. From analyzing the relative areas under the fits for each component, we found that the SiO-$Sn_{30}Fe_{30}C_{40}$ sample is roughly 57% $FeSn_2$, 32% Fe metal, and 11% Fe_3Sn. One interesting property seen in the Mössbauer spectrum is that $FeSn_2$, which is antiferromagnetic at room temperature (the Neel temperature lies between 378 K to 393 K), appears as a single line in Fig. 6-9 (that is, it appears to be nonmagnetic).[16] This superparamagnetic effect of $FeSn_2$ is most likely caused by the ball milling creating nanosized particles of $FeSn_2$ (on the order of 20 nm or less). The other interesting effect is the existence of Fe_3Sn. Generally, this compound is formed at high temperatures (by a diffusion synthesis technique) and decomposes quickly upon cooling to room temperature.[16] However, the

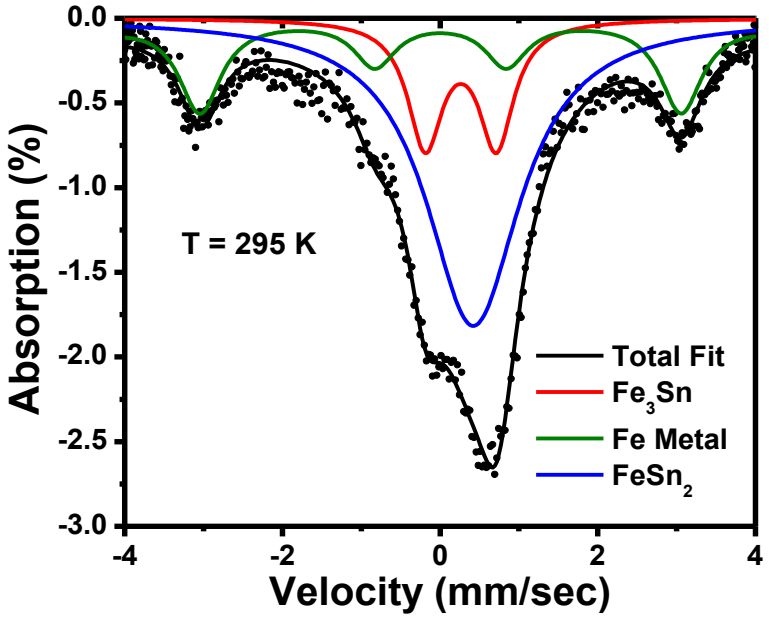

Fig. 6-9 Mössbauer spectrum of as-milled 50 wt.% SiO-50 wt.% $Sn_{30}Fe_{30}C_{40}$ showing that it is composed of magnetic Fe metal, superparamagnetic $FeSn_2$, and paramagnetic Fe_3Sn at room temperature

thermodynamics of ball milling appears to lead to a stable phase of Fe_3Sn, allowing a unique room-temperature Mössbauer measurement of Fe_3Sn.

Fig. 6-10a presents discharge-charge voltage profiles for the 1st, 2nd, and 50th cycles of the composite anode material. In the first cycle, the electrodes exhibit discharge and charge capacities of 1427 mAh/g and 961 mAh/g, respectively. All the discharge capacity is delivered below 0.4 V. The Coulombic efficiency is 67% in the first cycle, higher than those of the sample #1 to #6 anodes. After the initial cycles, the coulombic efficiency rapidly increases to near 100% and remains stable throughout the 50 cycles (Fig. 6-10c). No voltage plateau is observed in the discharge/charge process. The amorphous phase of SiO and the smaller grain size may be the contributing factors to the sloping voltage curves. The voltage curves keep the same shapes at the 50th cycle, indicating good Li insertion/extraction reversibility. The plot of differential capacity with cell potential for

the composite anode is shown in Fig. 6-10b. For the first discharge, SEI formation occurs from 0.3 V to 0.6 V. Two peaks are observed at 0.3 V and 0.48 V in Fig. 6-10b for the charge process and are attributed to the phase transitions between amorphous LixSi phases.[22,23] Fig. 6-10c shows the discharge/charge specific capacity versus cycle number for the composite electrode, along with its Coulombic efficiency. This anode delivers a specific capacity of 900 mAh/g and 700 mAh/g at rates of 300 mA/g and 800 mA/g, respectively. The specific capacities at various current densities with the composite electrode are shown in Fig. 6-10d. The composite electrode maintains 600 mAh/g at high

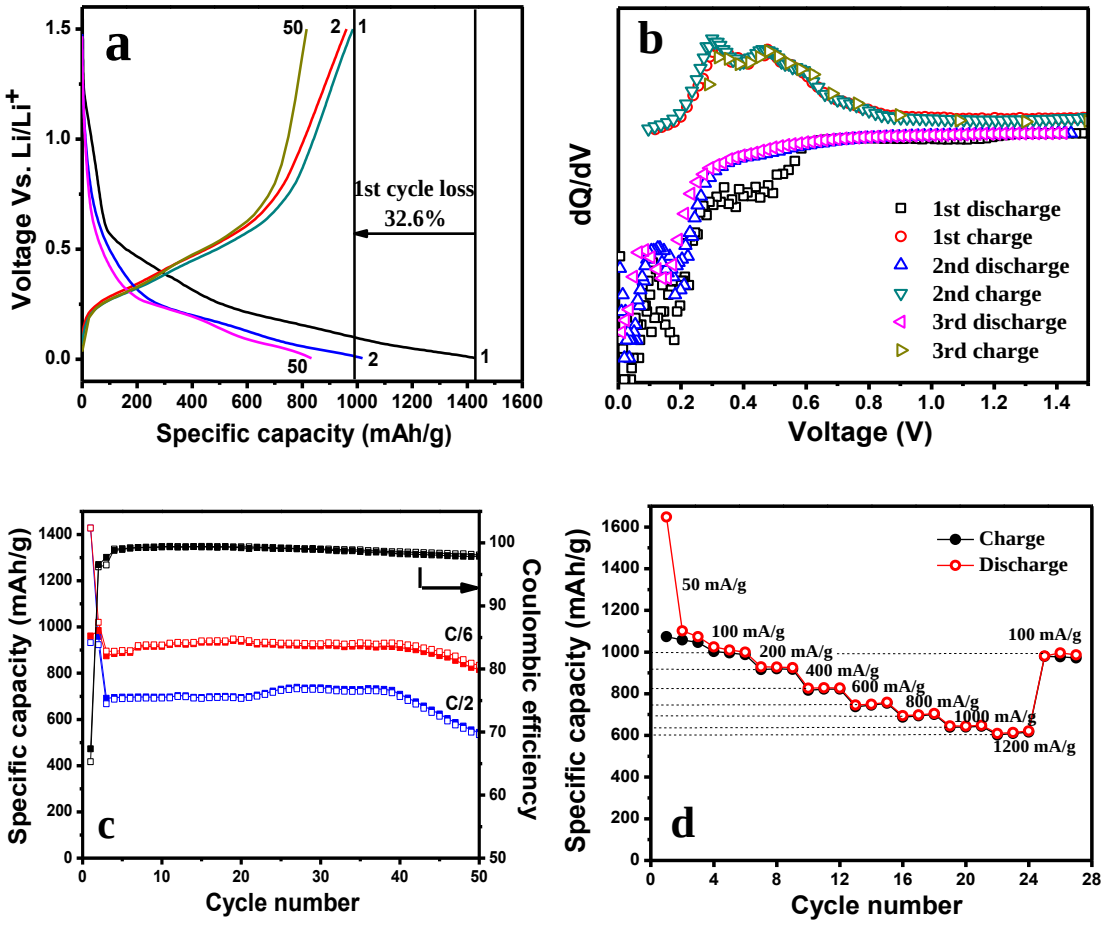

Fig. 6-10 Electrochemical properties of as-milled 50 wt.% SiO-50 wt.% $Sn_{30}Fe_{30}C_{40}$ composite: (a) voltage profile, (b) differential capacity, (c) cycle performance, and (d) rate capability

current density (1200 mA/g) and exhibits excellent recoverable performance after switching back to a low current density (100 mA/g). SiO-$Sn_{30}Fe_{30}C_{40}$ delivers a high capacity of ~900 mAh/g sustainable for 50 cycles. Unfortunately, this composition shows some capacity fading due to the presence of a high amount of $FeSn_2$. The sample #3 (50 wt% SiO–50 wt% $SnFe_3C_5$) provides medium capacity of about 600 mAh/g sustainable for about 100 cycles without capacity loss. The good cycleability of sample #3 is due to the presence of less $FeSn_2$ as revealed by XRD (Fig. 6-2). It is known that $FeSn_2$ has the same crystal structure and atom sites occupied as $CoSn_2$. Mao and Dahn explained that these compounds have tunnels among Sn atoms for Li penetration.[14] However, neither Fe_3Sn nor other Fe-Sn intermetallic compounds have such lithium-penetrating tunnels. Lithium-ion intercalation is more difficult in these compounds because Fe acts like a "skin" to block the further lithiation reaction. As a consequence, $FeSn_2$ delivers higher capacity, although its cycle life suffers from degradation due to large volume expansion. Compared with $FeSn_2$, $CoSn_2$ has much better cycle performance. The reason is still unclear. Therefore, this phase should be avoided during milling.

6.4 Conclusion

In summary, we prepared the composite anode materials of SiO-$Sn_xFe_yC_z$ by the mechanical alloying method. Metallic iron was chosen to take the place of cobalt in a previous promising composite, which immensely cuts the cost and acts more environmentally friendly. The electrochemical performance (capacity and life) of the composite anode can be optimizing by tuning the composition of silicon monoxide and tin/iron/carbon. The 50 wt.% SiO-50 wt.% $SnFe_3C_5$ composite electrode delivered the best electrochemical performance in terms of cycle life and capacity. Also studied was

the 50 wt.% SiO-50 wt.% $Sn_{30}Fe_{30}C_{40}$ composite electrode, which attained capacity levels as high as 700 mAh/g at a current of C/2 and 900 mAh/g at a current of C/6 for 40 cycles and exhibited good rate capability.

6.5 Reference

[1] I. A. Courtney and J. R. Dahn, *J. Electrochem. Soc*., 1997, **144**, 2045.

[2] I. A. Courtney and J. R. Dahn, *J. Electrochem. Soc*., 1997, **144**, 2943.

[3]

Sony News Release, accessed at http://www.sony.net/SonyInfo/News/Press/200502/05-006E/.

[4] A. D. W. Todd, R. E. Mar and J. R. Dahn, *J. Electrochem. Soc*., 2006, **153**(10), A1998-A2005.

[5] A. D. W. Todd, R. E. Mar and J. R. Dahn, *J. Electrochem. Soc*., 2007, **154**(6), A596-A604.

[6] P. P. Ferguson, A. D. W. Todd and J. R. Dahn, *Electrochem. Commun*., 2008, **10**, 25–31.

[7] P. P. Ferguson, R. A. Dunlap and J. R. Dahn, *J. Electrochem. Soc*., 2010, **157**(3), A325-A332.

[8] A. D. W. Todd, R. A. Dunlap and J. R. Dahn, *J. Alloys and Compounds*, 2007, **443**, 114–120.

[9] P. P. Ferguson, M. L. Martine, R. A. Dunlap and J. R. Dahn, *Electrochim. Acta*., 2009, **54**, 4534–4539.

[10] P. P. Ferguson, P. Liao, R. A. Dunlap and J. R. Dahn, *J. Electrochem. Soc.*, 2009, **156**(1), A13-A17.

[11] R. B. Lewis, A.Timmons, R. E. Mar and J. R. Dahn, *J. Electrochem. Soc*., 2007, **154**(3), A213-A216.

[12] R. A. Dunlap, O. Mao and J. R. Dahn, *Physical Review B*, 1999, **59**, 1-7.

[13] O. Mao, R. A. Dunlap and J. R. Dahn, *J. Electrochem. Soc*., 1999, **146**, A405-A413.

[14] O. Mao and J. R. Dahn, *J. Electrochem. Soc*., 1999, **146,** A414-A422.

[15] O. Mao and J. R. Dahn, *J. Electrochem. Soc*., 1999, **146**, A423-A427.

[16] O. Mao, R. A. Dunlap, I.A. Courtney and J. R. Dahn, *J. Electrochem. Soc*., 1998, **145**, 4195-4203.

[17] B. Liu, , A. Abouimrane, Y. Ren, M. Balasubramanian, D-P.Wang, Z. Z. Fang and K. Amine, *Chem. Mater*., 2012, **24**(24), 4653.

[18] R. Zhang and M. S. Whittingham, *Electrochem. Solid-State Lett*., 2010, **13**(12), A184-A187.

[19] Q. Fan, P. J. Chupas and M. Stanley Whittingham, *Electrochem. Solid-State Lett*., 2007, **10**(12), A274-A278.

[20] Y. Nagao, H. Sakaguchi, H. Honda, T. Fukunaga and T. Esaka, *J. Electrochem. Soc*., 2004, **151**(10), A1572-A1575.

[21] A. D. W. Todd, P. P.Ferguson, M. D. Fleischauer and J. R. Dahn, *Int. J. Energy Res.*, 2010, **34**, 535–555.

[22] H. Kim and J. Cho, *Nano Lett*., 2008, **8**(11), 3688-3691.

[23] J. Li and J. R. Dahn, *J. Electrochem. Soc*., 2007, **154**, A156.

CHAPTER 7

SUMMARY AND FUTURE WORKS

7.1 Summary of results

The thesis has described a high-capacity, inexpensive, long cycle life and environmentally friendly anode for lithium-ion batteries prepared by mechanical alloying. With those goals in mind, a novel oxide alloy composite material MO-$Sn_xCo_yC_z$ (MO=GeO_2, SnO_2, SiO and SiO_2) has been proposed and investigated. The electrochemical behavior and lithiation mechanism of the composite electrodes were studied. A systematic study has been performed on the screening, particle size, surface area, crystal/amorphous structures, electrochemical properties, and structural changes during lithiation/delithiation through many techniques like PSA, BET, XRD, PDF, EXAFS, and Mössbauer spectroscopy. The main findings are summarized as follows:

1. The screening process was carried out on different combinations of various oxides, such as SnO_2, SiO_2, GeO_2, and SiO, and tin-cobalt-carbon by electrochemistry test. GeO_2 and SiO are the most promising candidates for the components of the composite materials.
2. The GeO_2 composite anode shows a reversible capacity over 800 mAh/g with good capacity retention. Furthermore, the first cycle Coulombic efficiency has been improved up to 80%, which is much higher than that (34.6%) of pure GeO_2. The feature is closely associated with the reversible lithiation-delithiation reaction of

metal oxide. The Co_3Ge_2 might act as the catalytic role in the reaction.

3. SiO-$Sn_{30}Co_{30}C_{40}$ composite anode material shows superior electrochemical properties, compared with other composite material, in terms of cost, capacity, pack density, and lifespan. A series of composite anode materials of xSiO • (1-x)$Sn_xCo_yC_z$ were studied by electrochemical method. The composition of 50 wt.% SiO-50 wt.% $Sn_{30}Co_{30}C_{40}$ shows the best electrochemical performance. Ex-situ X-ray diffraction and *PDF* study of different cut-off voltages reveals the phase transformation during intercalation/convertion reaction, $CoSn_2 + (x+xy)Li \leftrightarrow (1+y)Li_xSn + CoSn_{1-y}$.
4. Two mechanical alloy methods, commercial SPEX milling and custom-made planetary milling, were used to synthesize 50 wt.% SiO-50 wt.% $Sn_{30}Co_{30}C_{40}$ composite anode material. A remarkable improvement of specific capacity could be obtained through planetary milling, which provides high centrifugal force to confine particles between milling balls and promotes the milling effect in terms of particles size, morphology, and alloying degree. In half-cell tests, the planetary-milled SiO/$Sn_{30}Co_{30}C_{40}$ composite electrode exhibits 700 mAh/g and 900 mAh/g at 300 mA/g and 900 mA/g, respectively. The half-cells work stably at high temperature. The stable lithium metallic powder technique improves the Coulombic efficiency to 86% for half-cell. The full-cell configuration ($Li_{1.2}Ni_{0.15}Co_{0.10}Mn_{0.55}O_2$ vs. 50 wt.% SiO-50 wt.%$Sn_{30}Co_{30}C_{40}$) has been cycled over 200 cycles.
5. We eliminated the expensive and toxic cobalt from the anode material and replaced it with cheap and environmentally benign iron, resulting in a SiO-$Sn_xFe_yC_z$ composite. The electrochemical performance (capacity and life) of the composite anode can be optimized by tuning the composition of silicon monoxide and tin/iron/carbon. The 50

wt.% SiO–50 wt.% $Sn_{30}Fe_{30}C_{40}$ composite electrode attained capacity levels as high as 700 mAh/g at a current of C/2 and 900 mAh/g at a current of C/6 for 40 cycles and exhibited good rate capability. The 50 wt%SiO-50 wt%$SnFe_3C_5$ composite electrode delivered the best electrochemical performance in terms of cycle life and capacity.

The density and cost of various oxides (pristine state) and the electrochemical properties of the oxide composite anode materials investigated in this thesis have been summarized in Tables 7-1 and 7-2. Based on an overall consideration of various factors, SiO composite anode material prepared by ultra high-energy milling can provide the best electrochemical performance in terms of capacity and cycle life, and also have acceptable tap density and cost.

7.2 Suggestion for Future Works

Further studies on these topics could be carried out mainly in the following five fields:

1. Although mechanical alloying is a low-cost and easily commercialized method to synthesize the composite anode materials, the inherent drawbacks of MA are unavoidable. Samples easily get into the contamination from the surface of the

Table 7-1 Density and cost of various oxides (pristine state)

Oxide	Tap density (g/cc)	True density (g/cc)	Cost
SnO_2	3.02	7.13	Low
SiO_2	1.43	3.58	Low
GeO_2	2.62	5.06	High
SiO	1.89	3.78	Low

Table 7-2 Electrochemical properties of the composite anode materials

Electrochemical properties / Anode materials	Voltage vs. Li^+/Li	The first cycle efficiency	Specific capacity mAh/g (100th)	Rate capability
SnO_2-$Sn_{30}Co_{30}C_{40}$	0.7 V	65%	387	Poor
SiO_2-$Sn_{30}Co_{30}C_{40}$	0.5 V	63%	432	Excellent
GeO_2-$Sn_{30}Co_{30}C_{40}$	0.4 V	80%	780	Good
SiO-$Sn_{30}Co_{30}C_{40}$ (SPEX)	0.2 V	73%	616	Poor
SiO-$Sn_{30}Co_{30}C_{40}$ (UHEM)	0.2 V	65%	850	Good
SiO-$SnFe_3C_5$	0.2 V	54%	538	-
SiO-$Sn_{30}Fe_{30}C_{40}$	0.2 V	67%	927 (40th)	Excellent

grinding medium and the inner walls of the container. The phases and particle size cannot be controlled exactly during milling, which is significant for the electrode fabrication and performance of batteries. Future work should focus on the improvement of the particle morphology using other chemical/physical synthesis methods.

2. The anomalous capacity of milled SiO_2 composite was found, but the mechanism of the reaction is not clear. Recently, some literature reported that SiO_2 can be milled into nano Si with oxygen loss. But the reliability has been verified and acknowledged universally. We need to design new experiments to demonstrate the accuracy of the above conclusion.

3. GeO_2 was found to be reversible during lithiation/delithiation. Some researchers explained that decreasing particle size led to enhanced electrochemical activity towards the reversible reactions of metal oxides and transition metal worked as the catalyzer to trigger this reversible reaction. But the mechanism still needs to be further studied.
4. Within the SiO-SnCoC anode, the primary work has been focused on to produce materials that are amorphous and have smaller grain size by different milling methods, which leads to better electrochemical performance. Low first cycle efficiency has limited its application on the commercial batteries. New techniques should be figured out to improve the first cycle efficiency.
5. In Chapter 7, we used cheap and environmentally benign iron instead of the expensive and toxic cobalt, resulting in a SiO-$Sn_xFe_yC_z$ composite. Although it exhibits acceptable electrochemical performance, it is still far from commercial use. We need to continue the search for new candidate elements to improve capacity and cycle life.

APPENDIX A

PUBLICATION LIST

1. Bo Liu, Ali Abouimrane, Yang Ren, Mahalingam Balasubramanian, Dapeng Wang, Zhigang Z. Fang, Khalil Amine, "*New anode material based on SiO-$Sn_{30}Co_{30}C_{40}$ for lithium batteries*", *Chem. Mater.*, 2012, **24** (24), pp 4653–4661
2. Bo Liu, Ali Abouimrane, Dennis Brown, Xiaofeng Zhang, Yang Ren, Zhigang Z. Fang, Khalil Amine, "*Mechanically alloyed composite anode materials based on SiO-$Sn_xFe_yC_z$ for Li-ion batteries*", *J. Mater. Chem. A*, 2013, **1**, 4375-4382
3. Bo Liu, Ali Abouimrane, Yang Ren, Jörg Neuefeind, Zhigang Z. Fang, Khalil Amine, "*Electrochemical study and material characterization of xSiO • $ySn_{30}Co_{30}C_{40}$ composite anode material for Lithium ion batteries*", *J. Electrochem. Soc.*, 2013, **160** (6), A882-A887
4. Bo Liu, Ali Abouimrane, Yang Ren, Mahalingam Balasubramanian, Zhigang Z. Fang, Khalil Amine, "*An electrochemical investigation of GeO_2 composite as a negative electrode in Li-ion batteries*" Manuscript in preparation